Signature, Supervisor

TECHNISCHE UNIVERSITÄT WIEN
Vienna University of Technology

Monte-Carlo simulation of a new ultra-fast gamma detector design in Geant4

performed at the Institute for Atomic and Subatomic Phyics
at the Vienna University of Technology

under supervision of
Univ.Prof. civ.ing. tekn.lic. tekn.dr. Lembit Sihver
Univ.Ass. Dipl.-Ing. Dr.techn. Albert Hirtl
Assistant Prof. Dennis R. Schaart, PhD
Dipl.-Ing. Dr.techn. Stefan E.K. Brunner

by

Florian Dachs, Matr.-Nr. 1026828, 066 461

Gersthoferstraße 148/1/5, 1180 Währing, Vienna, Austria

Thursday 1st December, 2016

Signature, Student

Contents

1 Introduction

In recent years, solid state silicon photo multipliers (SiPM) have emerged as an alternative to conventional photo multiplier tubes (PMT) as a robust, compact and easy-to-handle alternative [1, 2]. Development of these detectors has started in the 1990s and has since then steadily progressed. While analogue SiPMs are still the state of the art and superior in terms of dark count rate and particle detection efficiency, a digital SiPM - or dSiPM - has the advantage of producing purely digital data. Such a device was developed by Philips [3] and is a promising candidate for applications in various fields of scientific study (i.e. Positron Lifetime Annihilation Spectroscpy - PALS) and medical imaging such as PET (Positron Emission Tomography) or combined imaging methods such as TOF-PET (Time of Flight PET) and PET-MRT (PET combined with Magnetic Resonance Tomography).

As part of the PALADIN project [4] which aims to develop a gamma photon detector with 100 ps FWHM time resolution, 1 mm FWHM spatial resolution, 10 % FWHM energy resolution and a detection efficiency of about 90 % [5, 6, 7], this work aims to provide an accurate simulation of the proposed detector system and to enable a first analysis of its properties.

The new design features a central cube shaped scintillation crystal with its sides in direct optical contact to up to 6 dSiPMs developed by Philips. The goal is to improve on current designs in terms of spatial and temporal resolution, energy resolution and photon detection efficiency. To this end, a GEANT4 (GEometry ANd Tracking) application was developed in this work to simulate the new detector system and produce output of resulting scintillation photon emissions from 511keV annihilation photons interacting with a monolithic LYSO:Ce:Ca (Lutetium Yttrium Oxy-Orthosilicate, co-doped with Cerium and Calcium) scintillation crystal.

The goal of this simulation is to determine whether or not the new detector system can be expected to improve on already existing designs where only one or two DPCs were used for readout. These older designs showed, i.e., varying performance for spatial reconstruction along different directions which was inherent in their asymmetric design. Possible improvements in performance for the 6-sided readout will be studied by first discussing the plausibility of the data and then analysing a few first results such as the probabilities of various processes, the distribution of detection times for photons, the number of Cherenkov photons produced per event, and the performance of a spatial reconstruction algorithm. The data analysis is performed with a self developed ROOT [8] script.

2 Technical Background

To begin with, a technical background on the main components of the simulated detector as well as the simulation tools will be given. The behaviour of the detector components will not yet be implemented in the simulation in detail (e.g. cross talk, dead time, etc.) but large scale effects such as saturation effects for dSiPMs must be understood and discussed if they are to be implemented properly. A quick introduction to GEANT4 and a short overview of ROOT will be given in the last two sections.

2.1 Single Photon Avalanche Diode - SPAD

The single photon avalanche diode (SPAD) is a silicon based solid state photon multiplier which relies on charge avalanches for signal amplification (see Figure 1) [9]. It is the smallest and most basic element of any (d)SiPM and the first element of its photon detection process.

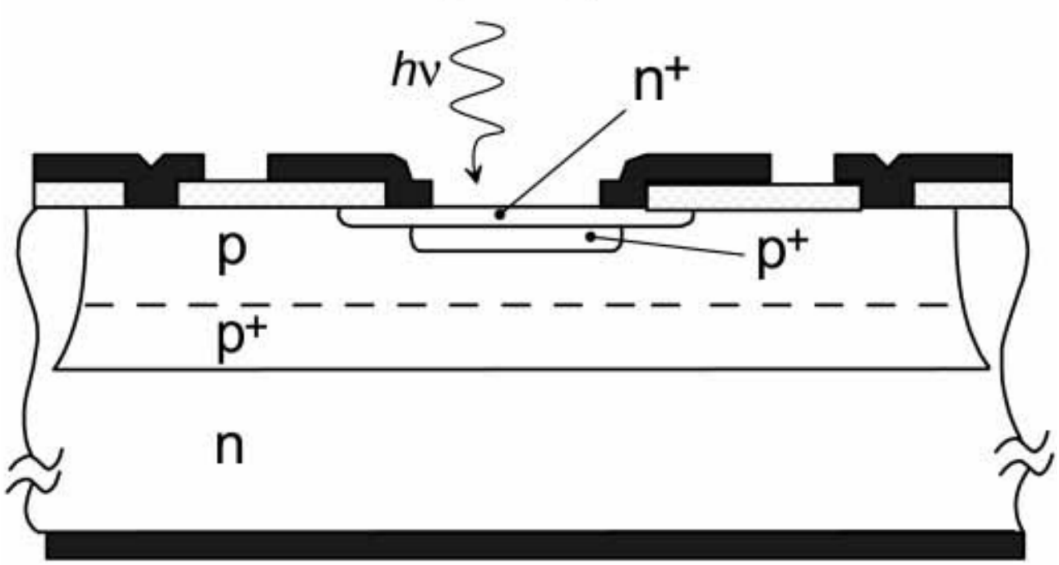

Figure 1: Cross section of a typcal SPAD [9]. Any particle impinging on the SPAD which produces charge carriers in the depletion zone can trigger an avalanche. If the applied bias and thus the electric field is high enough electrons are accelerated fast enough to create new electron-hole pairs which eventually creates a charge avalanche. The avalanche current is self-sustaining until the bias voltage is lowered to below V_{bd} (= quenching). When the avalanche has been quenched, the bias voltage is returned to $V_a > V_{bd}$ and the SPAD is in a ready state again.

During operation SPADs are reversely biased at the avalanche voltage $V_a > V_{bd}$ above the breakdown voltage so that electrons from electron-hole pairs produced in the depletion zone are accelerated enough by the electric field of the bias to create more electron-hole pairs and trigger an avalanche.
Naturally, a SPAD in its ready state (i.e. fully developed depletion region and bias at V_a) is extremely sensitive to any disturbance because a single charge carrier in the depletion zone, i.e. avalanche zone, will trigger an avalanche. This gives the SPAD its name and enables the measurement of single photons.

The SPAD goes through a number of steps if a particle is detected (see Figure 2):

- wait for avalanche trigger with bias voltage above the breakdown voltage
- build up avalanche and generate signal
- quench the avalanche by reducing bias below breakdown voltage
- increase bias voltage to initial value above breakdown voltage
- repeat

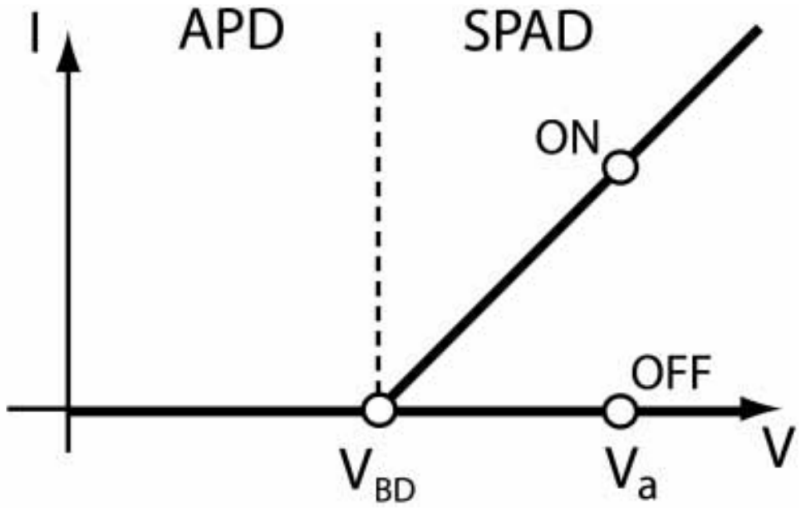

Figure 2: An operating diagram of a passively quenched SPAD [9]. First the bias is ramped to V_a and the SPAD is ready to trigger an avalanche ("OFF" mark). When a trigger occurs, the SPAD switches to the "ON" state, the avalanche is built up and the current increases. When a quenching resistor is connected in series to the SPAD, the avalanche is passively quenched by reducing the voltage (increasing current, constant resistor) below the breakdown voltage inhibiting the avalanche.

A SPAD cannot be triggered several times between recharges and thus the maximum measurable count rate depends on how fast an avalanche can be detected, quenched and the voltage be ramped up again.
Since SPADs are inherently sensitive to any disturbance in their avalanche region—most falsely triggered avalanches result from thermally generated charge carriers—the dark count rate of SPADs strongly depends on their temperature. Furthermore, impurities in the material can either act as traps for charge carriers, releasing them at a later time and possibly triggering a secondary avalanche after recharge (i.e. after-pulses), or create intermediary energy states in the band gap which lowers the SPADs avalanche trigger threshold and gradually decreases the bias V_a where the SPAD can operate stably.

2.2 Silicon Photomultipliers

Silicon photo-multipliers (SiPM) are silicon based solid state devices comprising of a large number of SPADs. They were invented in the 1990s [1] and have since then seen a lot of development [2] up to the current development of fully digital SiPMs [3]. Compared to conventional photomultiplier tubes, SiPMs provide a compact and robust device with high gain, detection efficiency, good timing capabilities and single photon counting capability showing at the same time no susceptibility to magnetic fields. Operating voltages are comparatively low at 100 V or less. This allows for safer handling compared to PMTs which require operating voltages in the kV range. Consequently, the power consumption of SiPMs is also much lower. Furthermore, SiPMs have a low nuclear counter effect (charged particles impinging on the device seldom trigger it) and can withstand accidental illumination.

Nevertheless, some shortcomings have to be acknowledged as well. To start with, the recovery time of individual SPADs much depends on their size (i.e. capacitance) and can reach hundreds of microseconds which limits the maximum count rate of the device. Although, with active quenching circuits, count rates of more than 1MHz are possible. Also, the dark count rate shows a strong temperature dependency and decreases by a factor of 2 for every decrease in temperature by 8 °C. Similarly, depending on the quenching resistors used, the recovery time of the SPADs may depend on temperature as well. This is an issue especially for SiPMs with a large number of small SPADs (as they are used, for example, in PET applications) because the amount of electronics increases with the number of SPADs and so does heat generation. Additionally, SiPMs which feature a large amount of small SPADs only reach low geometric factors (i.e. the ratio of active detector area over total detector area) because some space is needed between cells to accommodate the electronics and reduce optical cross talk, a phenomenon where SPADs trigger neighbours by emitting secondary photons which may be produced when an avalanche is triggered or by diffusion of charge carriers into the avalanche region of a neighbouring SPAD.

Despite the drawbacks SiPMs pose a good alternative to PMTs. In the case of combined medical imaging methods such as PET-MRT, they are the only viable candidate. Also, one has to acknowledge that PMT development has been ongoing for roughly 70 years by now and has arguably reached its limits, whereas SiPMs are still in a rather early stage of development and further increases in performance are to be expected.

DPC Tile	
Nb of Dies	16 (4×4)
Outer Dimensions [mm]	32.6×32.6
Glassplate and Glue thickness (front side) [μm]	$100 + 75$
Fill Factor [%]	≈ 73
DPC Die	
Max. Event Rate	122 kCPS
Dimensions [mm]	7.886×7.159
Number of Pixels	4 (2×2)
Actice Pixel Area [mm]	3.8016×3.2
Cells per Pixel	3200
Cell (SPAD) Size [μm]	59.4×64

Table 1: Characteristics of DPC dies and tiles.

2.3 The Digital Photon Counter developed by Philips

The digital photon counter (DPC) developed by Philips is one of the first fully digital SiPMs. This means that instead of an analogue output signal, the DPC directly provides digital photon counts and time stamps. A DPC die has several nested substructures: It contains 2×2 pixels, pixels contain 2×2 sub-pixels and sub-pixels contain 32×25 SPADs (as shown in Figure 3) which results in 12800 SPADs per die. Time stamps are generated at die level, photon counts at pixel level.

A DPC tile, as simulated in the GEANT4 application of this work, features a total of 16 DPC dies (4×4 configuration, see Figure 4). Thus a DPC tile can produce 16 time stamps and 16×4 photon counts independently. The dimensions and some technical specifications can be found in Table 1, schematics of a DPC tile can be found in section 4.2.

The basic operating scheme of a DPC can be seen in Figure 5. As long as the DPC is in ready mode, SPADs are triggered by true events as well as noise and dark counts. As soon as the trigger threshold is met, the validation phase begins.

During the validation phase, the detector waits for a configurable amount of time to accumulate a set number of hits and if this validation threshold is met, the DPC starts its integration phase and counts the number of triggered SPADs. The time stamps correspond to the first photon measured at a die when the initial trigger threshold is met and kept if the event is validated.

It is important to note, that reaching the trigger threshold is more or less just a matter of time since dark counts cannot be eliminated completely. However, it is possible to record a dark count map by addressing each SPAD individually and recording its dark count rate. SPADs with high dark count rates can then be deactivated. By deactivating, e.g., 10% of cells with the highest dark count rates, the overall dark count rate can be decreased by 80% [10].

The validation phase is important to distinguish true events from false ones because in order to pass the validation threshold, a given number of SPADs must be triggered within a given time window.

As already mentioned, each SPAD can only be triggered once between recharge cycles, and thus the maximum measurable photon count rate is determined by the number of SPADs in a die and its recharge rate. The

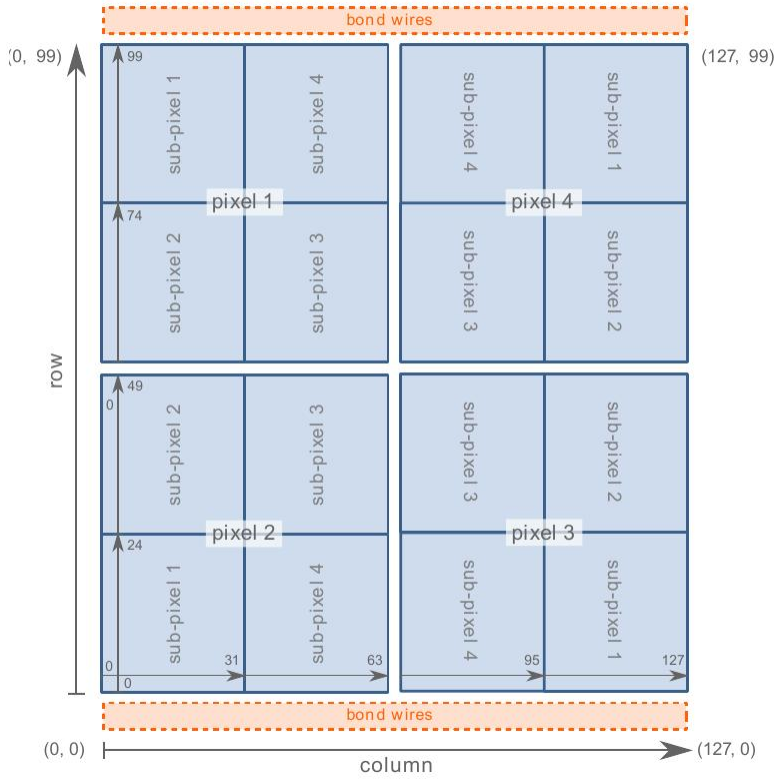

Figure 3: Pixel and sub-pixel structure of a DPC die [10].

detector reaches saturation for very high photon counts as the chance of SPADs being hit multiple times between recharge cycles increases. As a result the accuracy of the measured photon count decreases. This saturation effect [11] can be described by

$$N_{\text{detected}} = N_{\text{cells}} \left(1 - e^{-\frac{N_{\text{photons}}}{N_{\text{cells}}}}\right) \tag{1}$$

where N_{detected} is the number of detected photons (i.e. the number of triggered SPADs), N_{cells} the number of available SPADs and N_{photons} the number of photons which actually reached the detector.

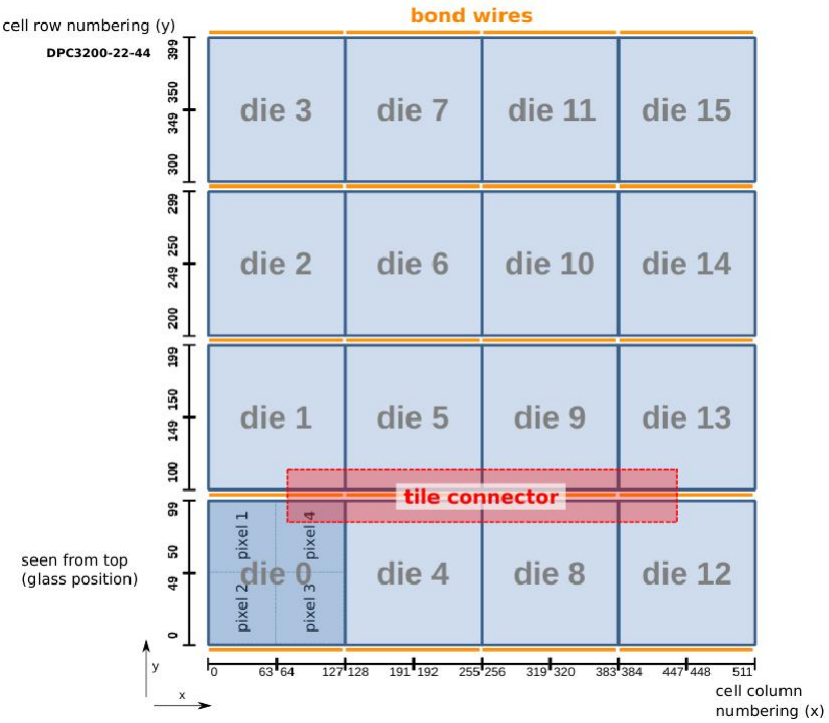

Figure 4: Die structure of a DPC tile [10].

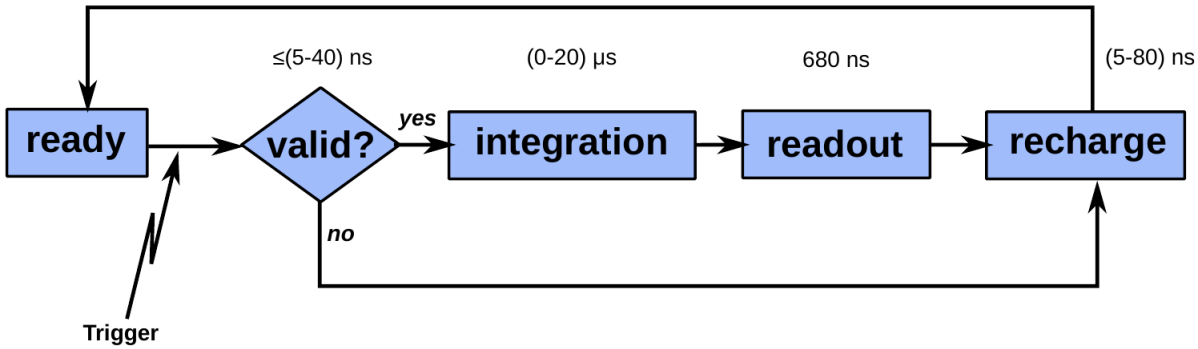

Figure 5: Operating procedure of a DPC die [10]. When a trigger occurs (i.e. enough SPADs have been triggered to exceed the trigger threshold), the die enters a validation phase. During this phase, a set number of photons must be detected within a given time window. If this validation threshold is met during that time interval, an integration and readout phase follows. After that the die is recharged and the cycle starts again. Otherwise, if the event is invalidated, the die is recharged right away.

2.4 A New Detector Design for Ultra Fast Gamma Detection

The detector design studied in this work features a central cube-shaped monolithic scintillation crystal and up to 6 DPC tiles, each one optically coupled to one of the crystals sides. Any scintillation event inside the cube can thus be recorded from all 6 sides.
Previously tested designs included a monolithic scintillator as well, but only with either 1 DPC tile attached to its backside or 2 DPC tiles attached to the front- and backside, with respect to incoming photon beams. Sides of the scintillation crystal not covered by a DPC were covered with a reflective layer to keep scintillation photons inside. This resulted in a large amount of photons being reflected at least once before they were detected by a DPC. The reconstruction of the point of interaction (POI) of a photon was done via look-up-tables. To this end, look-up tables where gathered by scanning fan-beams over the whole scintillator and measuring the photon- and time-distributions [12]. In real acquisition, photon count densities of unknown events were then compared to densities of pre-recorded events and the points corresponding to the k most similar densities were used to calculate a POI of the unknown event. This approach is called the k-nearest-neighbour method [13].
A symmetrical readout from all sides is expected to provide several advantages:

- The symmetric readout geometry provides isotropic spatial resolution.
- Less influence of reflected photons is expected which will improve, for example, center-of-gravity algorithms (COG) which rely on the geometrical information contained in photon count densities.
- Analytic reconstruction with better performance will speed up k-NN algorithms by providing an a-priori estimate of the POI and reducing the search space for k-NN.
- Timing resolution is expected to improve due to the larger number of recorded time stamps and will likely perform more stably.
- The 6-sided readout configuration has very high redundancy and can thus be expected to be more robust against missing dies (e.g. due to dead time).

The software to develop a simulation of this detector system was chosen to be GEANT4 due to its good software support, detailed documentation, access to source codes and highly flexible physics models.

2.5 GEANT4 - A Particle Transport Code

GEANT4 [14, 15] is an open source toolkit to simulate the passage of particles through matter. It was developed by a worldwide collaboration of scientists and covers a wide range of hadronic, electromagnetic and optical processes over an energy range from a few 100 eV to up to several TeV including a wide range of long-lived particles, elements and materials.
GEANT4 is written in C++ and features a highly modular structure for applications in general, but also for the physics processes and models implemented in these applications by exploiting the object oriented nature of its programming language.
Consequently, various particle sources, geometries and other modules of an application can be easily exchanged or altered without too much effect on other sections of the code. Likewise, various models describing the same physical process can be just as easily exchanged and their results compared.
Understanding the concepts of classes, objects, inheritance and overloading in C++ is vital to developing an application in GEANT4. The toolkit dictates the basic structure of any application by providing a plethora of default classes from which concrete user classes inherit their basic functionality. Often, a concrete user class is even required to contain a specific method or methods in order for it to work.
For example, every concrete detector construction user class must inherit from the G4VUserDetectorConstruction class provided by GEANT4 and must contain a method "Construct()" or otherwise the application will not work. The actual geometry of a specific application is implemented in the "Construct()" method.
This means that developing a new application is, to a large extent, about overloading existing default classes, adding new methods and "filling in" the body of mandatory methods specific to an application.
The full range of features offered by GEANT4 is beyond the scope of this work and consequently this thesis will only elaborate on the most important features and will do so only to an extent necessary to understanding the functioning of the application discussed in this work.

2.5.1 Procedural Structure

The following paragraphs will roughly elaborate the concept of runs, events, tracks and steps in GEANT4. These basic elements of the procedural structure are especially important because they govern the persistence of most objects created during a simulation and consequently determine, when and where data can be acquired from the simulation. In a more abstract way, the procedural structure often also affects how data can be acquired. For example, when the energy loss during a step is of interest, it is important to know when steps are being processed and how their persistence is limited.

The Run

A run is the largest unit of simulation of an application. During a run, the configuration of an application should be fixed. This means, that modules like the applications geometry or its physics list should not be changed. Runs are managed by the G4RunManager class which also handles all user initializations (such as the construction of the geometry, particles and physics processes). The G4RunManager class is a singleton (which means that during the execution of the application, only one instance of it may be created) and contains various methods to, e.g., initialize the application (before this point, changes to geometry, physics or other modules are still possible) and to start or kill a run. During a run, a number of events may take place.

The Event

An event is the basic unit of simulation during a run. When a new event starts, its primary tracks are generated and pushed into the events stack. Then, the stack is being processed one track at a time. Any secondary tracks (i.e., secondary particles) which are created along the way are put on the stack as well. As soon as all tracks are processed and the stack is empty, the event ends. Events are managed by the G4EventManager class which contains several methods partitioning an event into several stages (i.e. "BeginOfEvent", "EndOfEvent", etc.). Events do not persist beyond the scope of the run during which they were created.

The Track

Tracks can be understood as "snapshots" of particles which contain information about its current state (such as position or energy). Each individual particle of a simulation has its own, unique track with a unique track ID. The information contained in a track object is updated by steps and previous states of a track are not stored by the simulation by default. Since track IDs are unique, they allow tracking a particle along its way through the world of the simulation and record, for example, how often it has been reflected or undergone some other physical interaction. The class G4Track serves as an interface to access information currently held by a track object. The current state of a track is determined by the flag "TrackStatus" for which the most important values are

- fStopAndKill (i.e. the particle track has ended (i.e. by absorption, fission or leaving the world volume of the simulation) and
- fAlive.

Tracks do not persist beyond the event in which they were created.

The Step

Steps are among the smallest units of simulation. Tracks, i.e. individual particles, move through the world in a series of steps. The steps of any track are limited by all the processes attached to the corresponding particle and also by geometrical boundaries. For example, there are several processes for possible interactions of photons in matter. When the next step of a photon is calculated, GEANT4 uses Monte Carlo methods to determine which one of all the available processes yields the smallest step length and limits the step accordingly. After the step, the state of the photon (i.e., its track) is updated (i.e., interactions take place) and then the next step follows.
Apart from physical processes, steps are also limited by geometrical boundaries. If a track would cross the interface between two volumes during a step, the step instead ends prematurely at the boundary and the next step continues from there.
Each step is defined geometrically by a pre-step point and a post-step point which can be accessed via methods of the corresponding track object. It is also possible to acquire the process which limited the current step, the deposited energy, step length and other properties.

Data held by a step object is accessed via the G4Step class. Steps do not persist beyond the invocation of the next step. This means that GEANT4 does not store any data about previous steps of a track and consequently, the current state of a track is always just a "snapshot" of the corresponding particle.

As an example, a single run may contain a set number of events, where every event consists of a primary particle impinging on the detector. During every event, the primary particle track will undergo a number of interactions (i.e., steps) and, for example, produce secondary tracks which will in turn interact with the geometry. When, during an event, every step of every track has been calculated, the event ends and all the tracks and particles generated during the event are destroyed with it. Then, the next event starts until, finally, the last event is finished and the run ends as well.

2.5.2 Mandatory User Classes

Although the modular structure of GEANT4 puts only very few limits on how one might develop a new application, there are a few mandatory classes which must be implemented for the simulation to work at all. These mandatory user classes comprise the detector construction, primary particle generation and the physics list.

Detector Construction

In the detector construction module the geometry of an application is defined. This is usually done by placing various volumes into the 3D "world" of an application and filling them with their corresponding materials. Materials and their properties are also created in this module. Furthermore, volumes which are required to record data are declared "sensitive detectors" (see section 2.5.3).

Primary Generator

The primary generator module produces the primary particles which impinge on the detector system and is usually invoked at the beginning of a new event. Usually this means creating some sort of particle beam by defining the position of a vertex from which a given number of a given particle are emitted with a given energy and momentum. More complex primary generators include, for example, radioactive sources placed in the geometry.

Physics List

The physics list contains all the models necessary to simulate any physical processes of interest taking place during a simulation. In this module, the particles necessary for an application are "built" and the appropriate processes attached to them. These processes are also created here. The physics list, too, has a very modular structure and various models for the same physical process can be easily interchanged. Yet, this modular approach also has a drawback in that, by default, GEANT4 does not implement any physics at all. If a process or particle is not explicitly created in the physics list, it will not show up during a simulation. For this reason, GEANT4 provides preconfigured physics builders which are optimized for various general fields of physics (i.e. such as high energy phsics, neutron physics, electromagnetic physics, etc.) which can then be adapted by the user to precisely meet his or her requirements.

For example, when all mandatory user classes are implemented, the application can finally be compiled into a working simulation. Yet, the simulation will simply run, but not record any data or produce any output. To achieve that, further modules must be implemented which will be discussed in the following section.

2.5.3 Data Acquisition

Since GEANT4 does not record data by default, it is the user's job to implement the functionality necessary to acquire data from a simulation. Data is usually stored in "hit objects". These objects hold the data collected by a sensitive detector and must be implemented by the user.

Hit Objects

Hit objects are single units of data produced during a simulation. Whenever a SD is hit, i.e. a track completes a step within a volume belonging to the SD, and the hit is acknowledged, a hit object is created from the corresponding hit class and filled with the data. Hits are then stored in a hits collection which allows access to all the hits processed by an SD during an event.

Sensitive Detector

Sensitive detectors (SD) function as the main means of data acquisition in GEANT4. Any volume of the applications geometry can be declared a SD and for every different one of them, a corresponding SD class must be implemented.
Every SD class must inherit from the G4VSensitiveDetector class provided by GEANT4 and must contain a method "ProcessHits()". The explicit implementation of this method determines, which hits of an SD will produce data (i.e. one might define criteria which must be met before a hit is acknowledged), what kind of data (i.e. position, energy, momentum, etc.) and how that data is processed. If a hit produces data, the SD will create a new hit object which will be "filled" with the data and stored in the corresponding hits collection which is simply an array of hit objects produced by a specific SD. Hits can then be accessed at a later stage via their hits collection. Consequently, one must also implement a corresponding hit class for every SD which can provide hit objects suitable to hold the data produced by the SD.
SDs are declared in the detector construction module along with the materials and geometry of an application. They are declared via "logical volumes" which can be understood as the blueprint for any number of copies of a "physical volume" placed in the applications world. For example, all sub-pixels are copies sharing the same logical volume as their blueprint. By declaring this logical volume as a SD, all physical placements of sub-pixels become SDs as well. Thus, the declaration of an SD must not be purely geometrical and tied to a specific volume placed in the world but instead may comprise of any number of disjoint volumes which share the same logical volume.

For example, a water volume might be declared as a sensitive detector which will process any interactions of photons inside it, if the photon deposits energy (this is usually accomplished by simple if-statements in the ProcessHits() method). The SD might then acquire the position and time of the interaction and calculate its distance to each of the volume's surfaces. Then, the data is put into a hit object created from the corresponding hit class. The hit object is added to the corresponding hit collection and can be accessed later at the end of the event, when output is produced.

2.5.4 User Actions

The final goal in any GEANT4 application is usually to produce output. A good time to produce output is for example at the end of an event when the calculations of tracks and steps are finished and all the hits produced are stored in their hits collections. Also, data can be acquired at the end of the run if data was acquired across several events. For this purpose, there are various user action classes provided by GEANT4. The most relevant ones for this work are the run action, the event action and the stepping action classes which feature methods invoked at the beginning and end of runs, events or after steps, respectively.

Run Action

Run actions are invoked at the beginning and the end of a run. Yet, the run action also features a "GenerateRun()" method, which allows the user to initialize a custom run with, for example, custom energy cuts, physics models or an alternate geometry. As mentioned before, as soon as a run has started, the geometry or physics of any simulation should not be changed.

Event Action

As the name suggests, this user action class is invoked at the beginning and the end of an event. Consequently, producing output for every event is best done using this class and its methods "BeginOfEvent()" and "EndOfEvent()".

Stacking Action

The stacking action gives control over the order in which particle tracks are processed. By default, all primary and secondary tracks created during an event are placed on the urgent-stack. As a result, if an interaction of, for example, a primary particle produces secondary particles, i.e. tracks, these are put on top of the urgent-stack and—since the stack is processed from the top down—have to be processed before the primary track that produced them can be continued. If, for example, the primary tracks of an event need to be processed before any secondary tracks, the stacking action can be used to place secondary tracks on the waiting-stack which will not be processed before the urgent-stack is empty.

Stepping Action

As the name suggests the stepping action is invoked for every step of a track which is a great many times during a simulation. It is thus very important to keep its code simple and fast and do more complex calculations elsewhere. Possible applications are to manually invoke sensitive detectors or produce step-by-step output. It is also possible to filter for events where the primary particle undergoes a certain interaction and discard all others thus saving computational effort.

Output can be produced in various formats, GEANT4 directly supports ROOT, CSV and XML formats. Producing ASCII output can be done by opening a file and writing to it using standard C++ libraries and methods.

For example, one might set up a tree of folders to hold various parts of the output during the "BeginOfRun()" method of the run action, then fill those folders with event-specific data during the "BeginOfEvent()" and "EndOfEvent()" methods of the event action and finally output some statistical data about all the events during the "EndOfRun()" method.

2.6 ROOT - A Data Analysis Tool

ROOT [8] is a data analysis software specifically developed to handle large data files and works very well in combination with GEANT4. Its modular structure resembles that of GEANT4 albeit this is simply a feature of the programming language (C++) and not further enforced by mandatory modules or default classes to inherit from.
The structure of ROOT files is based on plant anatomy and thus data is structured in Trees, Branches and Leafs. Any ROOT file may contain a number of Trees which correspond to separate sets of data. Each Tree in return may contain any number of Branches which correspond to individual columns of data compared to a simple TXT file.
Usually ROOT is used via its command line based interface but scripts can be written as well by including the corresponding libraries in a C++ program. For this work, a C++ script implementing ROOT libraries was developed to process the data produced by the simulation. This way, fast data acquisition from the simulation can be achieved while at the same time, laborious computations can be done on specific sets of data with the analysis script.

3 Mathematical and Physical Background

The following chapter will introduce the mathematical and physical methods and models most relevant to this work. The Monte Carlo method is used extensively in GEANT4 to compute total cross sections and final states, the center of gravity (COG) and the peak value (a figure of merit chosen for data analysis) are both used in the analytic reconstruction algorithm shown in this thesis. The physical models implemented by GEANT4 will be discussed with a focus on the photoelectric effect, Compton scattering, scintillation, the Cherenkov effect and optical photons (a "second kind of light" implemented by GEANT4 to simulate optical properties of visible light).

3.1 The Monte Carlo Method

The Monte Carlo method is a numerical technique relying on random number generation to calculate probabilities and corresponding quantities [16]. It is often used to solve high dimensional optimization problems, calculate multidimensional integrals or to sample random numbers that follow a certain probability density function (PDF).
In the case of GEANT4, the Monte Carlo method is used, for example, to determine the next point of interaction of a particle based on its mean free path or the final state of an interaction by sampling random values which follow the corresponding PDF.
The basis for any MC calculation is the generation of a sequence of uniformly distributed random numbers $\vec{r}$ which follow ($\sim$) a uniform distribution N_0 over $[0, 1)$

$$\vec{r} = \{r_0, r_1, r_2, ...\}; \quad r_i \sim N_0 \tag{2}$$

which are then used to generate a new sequence of random numbers $\vec{x}$ which follow the PDF of interest $f(x)$

$$\vec{x} = \{x_0, x_1, x_2, ...\}; \quad x_i \sim f(x). \tag{3}$$

GEANT4 provides several algorithms to generate uniform random numbers. In this work the "RanecuEngine" generator was used.
The straight forward method to do this is called the transformation method which aims to find a function $x(r)$ which directly yields the desired sequence when evaluated on elements of $\vec{r}$. To find $x(r)$ one can request that

$$F(x(r)) = \int_{-\infty}^{x(r)} f(x')dx' = G(r) = \int_{-\infty}^{r} N_0(r')dr' = r \tag{4}$$

and thus

$$x(r) = F^{-1}(r) \tag{5}$$

where F(x(r)) is the cumulative distribution function (CDF), $f(x)$ the probabilitiy density function (PDF) of interest and $G(r)$ the CDF of N_0. For the PDF $f(x)$ several requirements must be met:

$$
\begin{aligned}
f(x) &\geq 0 \quad \forall\, x \in [-\infty, \infty] \\
\int_{-\infty}^{\infty} f(x)\, dx &= 1
\end{aligned}
$$

It should be noted here, that while in general x may range from $-\infty$ to ∞, $f(x)$ may only have non-zero values over an interval $[a, b]$ which effectively reduces integrals over $[-\infty, \infty]$ to integrals over $[a, b]$. This is the case, i.e., for Equation (4) where the lower limit of the integral of $N_0(r')$ is $-\infty$ despite the fact that N_0 only has non-zero values over $[0, 1)$.

The process of the transformation method is visually described in Figure 6.

Finding F^{-1} and solving for $x(r)$ is often very difficult or may not even be possible. Thus, alternatively, there is another, albeit less efficient, method to produce random numbers with the desired distribution which is called the rejection method.

If the PDF $f(x)$ of a distribution is too complex to find an analytic solution with the transformation method, one option is to instead use a rejection-function

$$
M\, g(x) \geq f(x), \quad \forall \quad x \in [a, b] \tag{6}
$$

where $[a, b]$ is the interval within which random variables need to be produced, $g(x)$ is a function which is easily sampled and M is a constant for which Equation (6) is fulfilled.

In order to compute samples of the desired PDF one must acquire a sample $r \sim N_0[0, 1)$ and a sample $x \sim g[a, b)$, then if

$$
r\, g(x) \leq f(x) \tag{7}
$$

x is accepted as $\sim f(x)$, otherwise another tuple of $\{x, r\}$ must be produced and tried. This process is visualized in Figure 7.

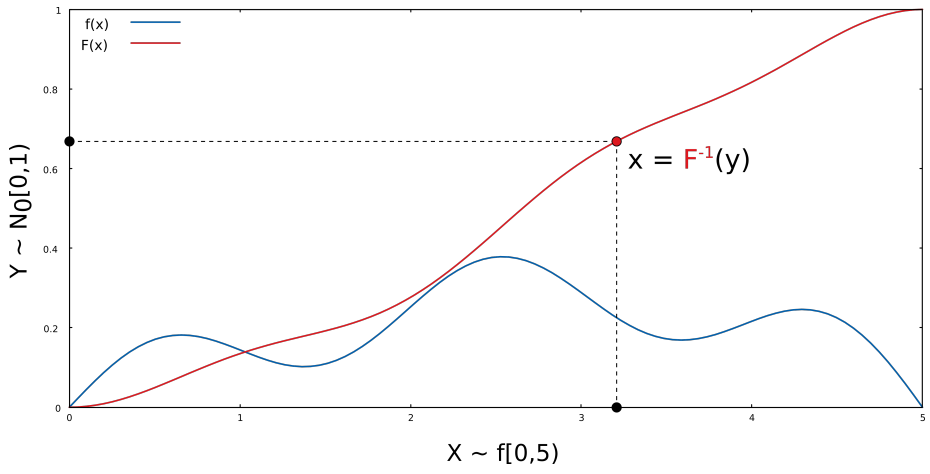

Figure 6: Sampling from a custom PDF f(x) on the interval $[0, 5)$. *First, find* $F(x)$ *and acquire its inverse. Then sample values* $x_i \sim f[0, 5)$ *by computing* $F^{-1}(r)$ *with* $r \sim N_0[0, 1)$.

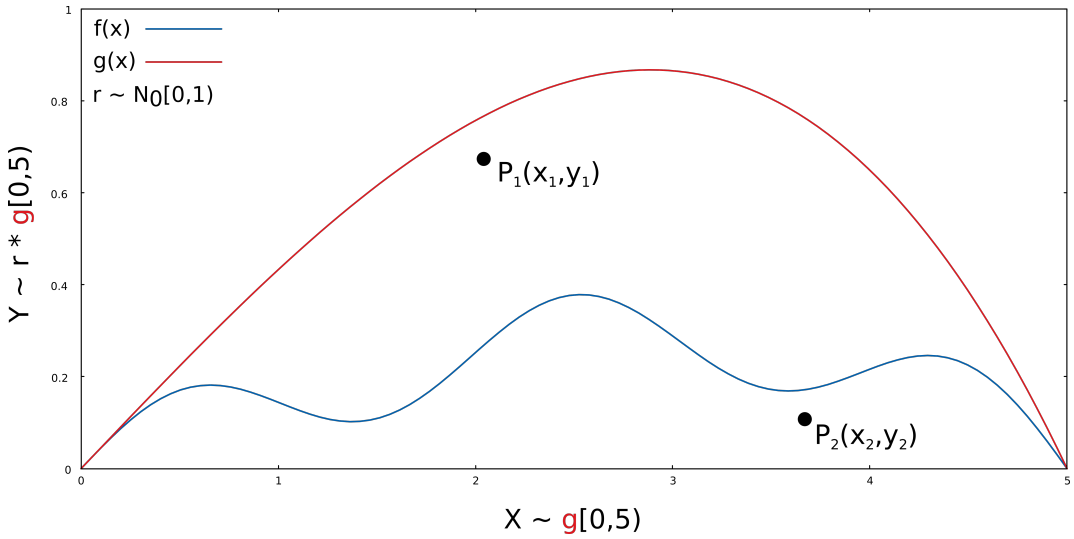

Figure 7: Sampling from a complex custom PDF f(x). First, produce samples $r \sim N_0[0,1)$ and $x \sim g[0,5)$. Then check, if the point $P(x, y = rx)$ is below the graph for $f(x)$. If no (see $P(x_1, y_1)$) sample a new set of x and r, if yes (see $P(x_2, y_2)$) x is accepted as $x \sim f(x)$.

The efficiency of the rejection method depends on how close $g(x)$ is to $f(x)$ because then Equation (7) is more easily fulfilled. This implies finding the smallest value for M for which Equation (6) is still true. Consequently, one also has to compromise between efficiency and complexity when choosing $g(x)$.
GEANT4 uses MC methods based on the rejection method to sample compound PDFs which comprise of a number of PDFs which describe, for example, several processes attached to a particle. With these samples the final states of an interaction can be determined [17]. Suppose the composition PDF of a final state is given by

$$f(x) = \sum_{i=0}^{n} N_i \, f_i(x) \, g_i(x) \qquad N_i > 0, \quad 0 < g_i(x) < 1, \tag{8}$$

where $f_i(x)$ are various normalized density functions describing the mean free path of a particle for various processes on the interested interval $[a, b]$ and $g_i(x)$ are the corresponding rejection functions.
Then $f(x)$ is sampled by

1. selecting an integer $i \in [0, n]$ with probability proportional to N_i,
2. producing a sample x_0 following the PDF $f_i(x)$,
3. calculating $g_i(x_0)$ and accepting x_0 with probability $g_i(x_0)$ and
4. returning to step 1 if x_0 is rejected. Otherwise, use x_0.

The mean value of tries for this method to yield an accepted value is

$$\bar{N} = \sum_{i=0}^{n} N_i. \tag{9}$$

3.2 Center of Gravity

The data produced by DPC tiles includes an 8×8 array of photon counts which correspond to the 8×8 pixels of the DPC. These arrays allow for the reconstruction of the point of interaction (POI) of the corresponding scintillation event.

Each bin of the photon count array corresponds to a pixel and thus a position on the DPC tile. Under the assumption that pixels with higher photon counts are closer to the POI one can calculate the center of gravity $COG(p, \vec{w}, \vec{x})$ in one dimension as

$$COG(p, \vec{w}, \vec{x}) = \frac{\sum_{i=0}^{N} w_i^p \, x_i}{\sum_{i=0}^{N} w_i^p}, \tag{10}$$

where $\vec{w}$ and $\vec{x}$ are vectors containing weighting factors and corresponding coordinates, respectively. N is the dimension of $\vec{w}$ and $\vec{x}$ and p is an arbitrary power ≥ 1. When reconstructing the two coordinates in the DPC's plane, the weighting factors correspond to the photon counts $n_i \in \mathbb{N}$ of each pixel. When reconstructing the normal distance between the DPC and the scintillation event (depth of interaction - DOI) the weights correspond to the peak value $P \in \mathbb{R}$ which is derived from the photon count array and will be introduced in the next section.

Usually, the center of gravity is calculated with linear weights ($p = 1$) but higher powers are hypothetically viable. For example, for $p > 1$ the influence of bins with small values will diminish while bins with high values will dominate.

3.3 The Peak Value - A Figure of Merit for Spatial Reconstruction

Although pixel photon counts provide good weighting factors for the reconstruction of the POI coordinates in the plane of a DPC tile, a new weighting factor is necessary to reconstruct the normal distance between scintillation event and DPC, i.e. the depth of interaction (DOI).

It can be assumed, that the DOI influences the height of pixel photon counts as well as their distribution across the DPC tile and hence the value

$$P(p) = \sum_{i=0}^{N} n_i^p, \quad n_i \in \mathbb{N} \tag{11}$$

where n_i is the photon count of the i-th bin, has been devised in this work to be applied as a figure of merit for how *peaked* a count distribution is. This choice can be justified by the following proof:

In the context of bins containing photon counts, we can give the following domains for photon counts n, n_i, n_j, differences in photon counts k and powers p:

$$n, n_i, n_j \in \mathbb{N} \tag{12}$$

$$k \in \mathbb{N}_0, \, k < n, n_i \tag{13}$$

$$p \in \mathbb{R}, \, p > 1. \tag{14}$$

$$\tag{15}$$

Suppose a total photon count

$$C_{\text{tot}} = \sum_{i=1}^{N} n_i \tag{16}$$

is arbitrarily distributed across all pixels of a DPC tile. Then this photon count distribution will yield a certain peak value P_0. Now, if any photon count $n_j = n_i - k$, $i \neq j$ of the j-th bin is decreased by 1 and the photon count n_i of the i-th bin is increased by 1, the total photon count C_{tot} is preserved, but the peak value will change by $(n_i \to n)$

$$\Delta P(n,k,p) = (n+1)^p + (n-k-1)^p - n^p - (n-k)^p. \tag{17}$$

which can be rewritten as

$$\begin{aligned} \Delta P(n,k,p) &= [(n+1)^p - n^p] - [(n-k)^p - (n-k-1)^p] & (18)\\ &= f(n+1,p) - f(n-k,p) & (19) \end{aligned}$$

with

$$f(n,p) = n^p - (n-1)^p. \tag{20}$$

For the derivative $f'(n,p)$ the following statement holds true:

$$\begin{aligned} f'(n,p) &= p(n^{p-1} - (n-1)^{p-1}) & (21)\\ f'(n,p) &> 0, \quad \forall \quad n \in \mathbb{N},\, p \in \mathbb{R}^+,\, p > 1. & (22) \end{aligned}$$

Thus $f(n)$ is strictly monotonously growing because power functions such as n^p are strictly monotonously growing for the given domains and Equation (18) must evaluate to ≥ 0 because $(n+1) > (n-k)$ $\square$.
Accordingly, $P(p)$ will grow whenever photon counts are "moved" from lower to higher bins ($k \geq 1$) or from one to another, equally high, bin ($k = 0$) and thus $P(p)$ will be larger when photon counts are distributed among fewer bins, i.e. when photon count arrays are peaked.
The maximum value for $P(p)$ is

$$P_{\max}(p) = {C_{\text{tot}}}^p \tag{23}$$

where all photons are detected in a single pixel, i.e. bin, and the minimum value is

$$P_{\min}(p) = \sum_{i=1}^{C_{\text{tot}} \bmod N} \left(\left\lfloor \frac{C_{\text{tot}}}{N} \right\rfloor + 1 \right)^p + \sum_{i=(C_{\text{tot}} \bmod N)+1}^{N} \left(\left\lfloor \frac{C_{\text{tot}}}{N} \right\rfloor \right)^p \tag{24}$$

where all photons are distributed as equally as possible over all bins. This has to be done in two steps if the total photon count is to be preserved because the integer division C_{tot}/N generally has a remainder $(C_{\text{tot}} \bmod N) > 0$. This remainder is distributed over the first $(C_{\text{tot}} \bmod N)$ bins in the first sum of Equation (24) by adding 1 to each element. After that, the remaining bins are summed normally in the second sum.

With $P_{\max}$ and $P_{\min}$ a relative peak value $P_{\text{rel}} \in \mathbb{R}$ can be defined as

$$P_{\text{rel}}(p) = \frac{P(p) - P_{\min}(p)}{P_{\max}(p) - P_{\min}(p)} \tag{25}$$

whose possible values are $P_{\text{rel}}(p) \in [0, 1]$.
With the relative peak value P_{rel}, the *peakedness* of different DPC tiles with different total photon counts can be compared. P and P_{rel} will be used as weighting factors for position reconstruction via COG.

3.4 Photons in Matter

The interaction of photons in matter is mainly governed by three different physical processes: the photoelectric effect, Compton scattering (including Rayleigh Scattering) and pair production [18]. The dominant process is determined by the photon energy and the atomic number Z of the target atoms. Generally, the photoelectric effect dominates for low energies and high Z, the Compton effect for a wide energy range and low Z and pair production for high energy and high Z. Pair production will not be discussed in this section because it is not relevant to this work where only 511keV photons are considered.

The energy dependent cross sections for coherent and incoherent scattering (Rayleigh scattering and Compton scattering, respectively), photoelectric absorption and pair production in LYSO:Ce:Ca are shown in Figure 8.

This section will take a look at the methods of the Livermore [19], Penelope [20] and LowEP [21] physics models implemented in GEANT4 in an effort to better understand the data generated by the application developed in this work. It will only provide a rough overview on how GEANT4 samples mean free paths and computes final states as these methods are often very complex. A reference to the corresponding section in the Physics Reference Manual [17]—the main source of information on the mathematical and physical methods used by GEANT4—will be given whenever a detailed description would become too lengthy.

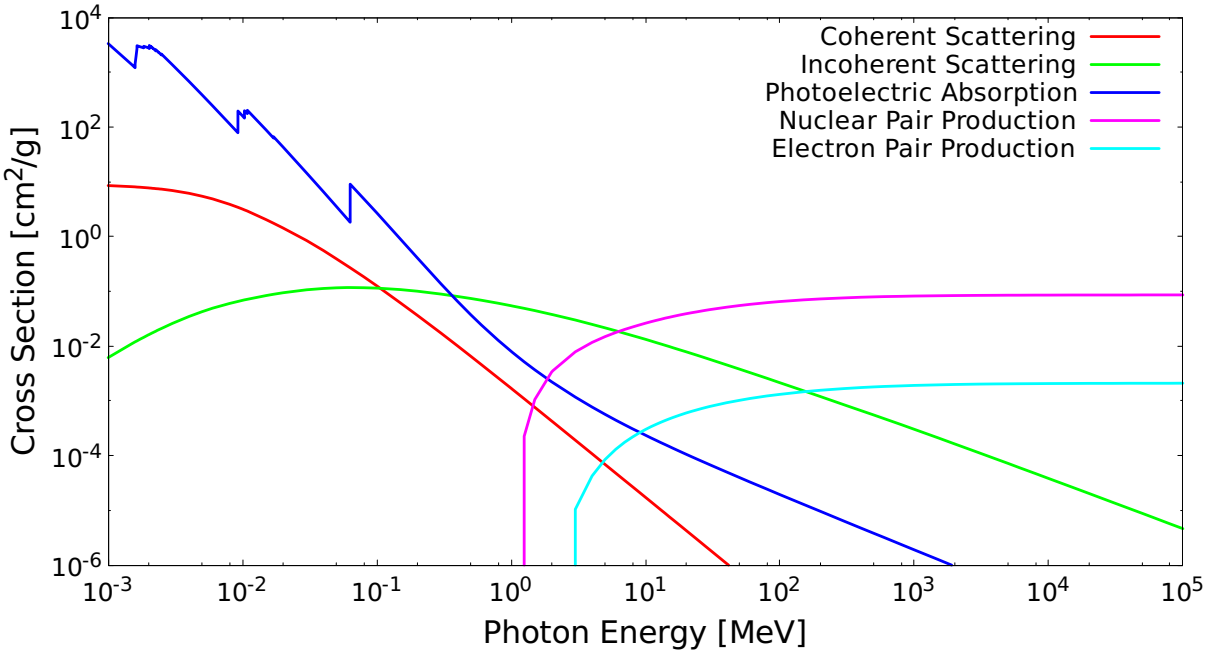

Figure 8: Various cross sections for photon interactions in matter depending on energy. This plot was done for LYSO:Ce:Ca with components as listed in the appendix in Table 14. The data was acquired from XCOM [22] and plotted with gnuplot [23].

3.4.1 Livermore Physics

The Livermore physics model [19] was developed to implement electromagnetic physics processes for very low energies and uses data from a set of publicly distributed evaluated data sets for the determination of cross sections and final states. The current implementation is valid down to 100 eV and up to 100 GeV. Elements with an atomic number between 1 and 99 are included.

Total Cross sections

Total cross sections for Compton scattering and electron interactions are obtained via interpolation with

$$\log(\sigma[E]) = \frac{\log(\sigma_1)\ \log(E_2/E) + \log(\sigma_2)\ \log(E/E_1)}{\log(E_2/E_1)} \tag{26}$$

where E is the energy for which a total cross section must be found, E_1 and E_2 are the energies of the closest lower and higher data points and σ_1 and σ_2 are the corresponding total cross sections, respectively.

Photoelectric Effect

The total cross sections for the photoelectric effect are tabulated for energies up to 600 keV. For higher energies, they are parametrized by

$$\sigma(E) = \sum_{i=1}^{5} \frac{a_i}{E^i} \tag{27}$$

where a_i are parameters and E is the photon energy. This parametrization reaches an accuracy of better than 1 %.
The final state is sampled by calculating the energy of the electron via the well known equation

$$E_{e^-} = h\,\nu - E_{\text{binding}} \tag{28}$$

where h is the Planck constant, ν the photon frequency and E_{binding} the binding energy of the atomic electron. The angular distribution of the emitted photo-electron is sampled from the Sauter-Gavrila angular distribution. A detailed documentation of this rather complex distribution and the corresponding sampling method can be found in the PRM in section 9.8.3.

Compton Scattering

The angular and energy distribution of the final state for Compton scattering is sampled from

$$P(\epsilon, x) = \Phi(\epsilon) \times SF(x) \tag{29}$$

where $\Phi(\epsilon)$ is the Klein-Nishina formula and $SF(x)$ the scattering function [24]

$$\begin{aligned}
\Phi(\epsilon) &\cong \left[\frac{1}{\epsilon} + \epsilon\right] \left[1 - \frac{\epsilon}{1+\epsilon^2}\,\sin^2(\theta)\right] && (30)\\
\epsilon &= \frac{E_f}{E_i} \\
SF(x) &= \sum_j A_j \left(1 - \frac{1}{[1 + B_j\, x]^N}\right) && (31)\\
x &= E_i^2\,(1 - \cos(\theta)) && (32)\\
\sum_j A_j &= Z.
\end{aligned}$$

Z is the atomic number, θ is the scattering angle of the photon and ϵ the ratio between the final and initial energy of the photon. Sub-shells of the atom are enumerated by j and A_j, B_j and N are parameters to fit tabulated data sets for the scattering function. A polar plot of the angular distribution produced by the Klein-Nishina formula for various energies can be seen in Figure 9.
The determination of the final state is very complex and is described in section 5.3.2 in the PRM. However, ϵ is sampled from probability distributions based on the first factor in Equation (30) and then, since E_i is known, E_f is known as well and θ can be determined via the Compton formula

$$E_f = E_i\,\frac{m_e\,c^2}{m_e\,c^2 + E_i\,(1 - cos\,\theta)} \tag{33}$$

where m_e is the rest mass of the electron and c the speed of light. Then x and consequently $SF(x)$ can be determined. The azimuthal angle for both, photon and electron, are sampled isotropically over $[0, 2\pi)$.
It should be noted here, that Compton scattering may not only occur for free electrons, but also for atomic electrons, if the energy of the gamma is sufficiently larger than the binding energy of the electron. This is usually the case for photon interactions in solids and necessitates the implementation of the scattering function $SF(x)$ which is responsible for such effects as Doppler Broadening of the final energies of the photon caused by the initial momentum of the electron and very important for low energies. The scattering function also suppresses complete forward scattering because $x = 0$ for $\theta = 0$ and consequently $SF(x = 0) = 0$.

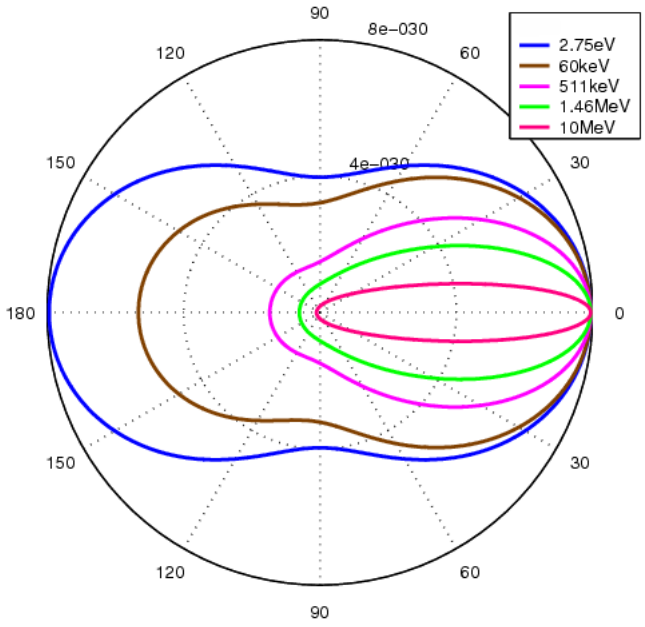

Figure 9: Polar plot of the angular scattering distribution of the Klein-Nishina formula for various energies. The probability for forward scattering increases with energy [25].

Rayleigh Scattering

The coherent scattering angle θ of the photon is sampled from

$$\begin{aligned}
\Phi(E,\theta) &= R(\theta) \times FF^2(x) && (34)\\
R(\theta) &= \sin(\theta)(1+\cos^2(\theta)) && (35)\\
FF^2(x) &= \sum_j \frac{A_j}{[1+B_j\,x]^N} && (36)\\
x &= E_i^2(1+\cos(\theta)) && (37)\\
\sum_j A_j &= Z^2
\end{aligned}$$

where Z is the atomic number, $R(\theta)$ the Rayleigh formula and $FF^2(x)$ the square of Hubbel's form factor [24]. Again, A_j, B_j and N are parameters to fit tabulated values for $FF^2(x)$.
The sampling procedure starts by selecting an atom randomly according to its corresponding cross section and then sampling $\cos(\theta)$ from $\Phi(E,\theta)$. The azimuthal angle is sampled uniformly over $[0, 2\pi)$.

3.4.2 Penelope Physics

The Penelope physics model [20] was developed specifically for Monte Carlo simulations and low energy electromagnetic processes. Hence this model is valid for energies down to a few hundred eV and up to $\approx 1\,\mathrm{GeV}$.
Contrary to the empiric approach of the Livermore model, Penelope mostly utilizes analytical parametrization to determine total cross sections and final states.

Photoelectric Effect

The total cross section for the photoelectric effect is acquired in the same way as described in section 3.4.1.
The electron's energy is calculated with Equation (28). The final state is determined by sampling from the Sauter distribution (see PRM section 10.1.5.).

Compton Scattering

The total cross section for Compton scattering utilizes the usual Klein-Nishina formula for initial photon energies $E_i > 5\,\mathrm{MeV}$. For lower energies, a more accurate parametrization which includes atomic binding effects and Doppler Broadening is used

$$\sigma(E_i) = 2\pi \int_{-1}^{1} \frac{r_e^2}{2} \frac{E_C^2}{E_i^2} \left(\frac{E_C}{E_i} + \frac{E_i}{E_C} - \sin^2(\theta) \right) \left(\sum_{\text{shells,i}} f_i \, \Theta(E_i - U_i) \, n_i(p_z^{\max}) \right) d(\cos(\theta)) \tag{38}$$

where r_e is the classical electron radius, m_e the electron rest mass, θ the scattering angle of the photon, E_C the Compton energy (see Equation (33), $E_f \to E_C$), f_i the number of electrons in the i-th atomic shell, U_i the ionization energy for the i-th shell, Θ the Heaviside step function and $p_z^{\max}$ the highest possible value of the initial momentum of the atomic electron p_z projected in the direction of the scattering angle.
The function n_i is given by

$$\begin{aligned} n_i(p_z) &= \int_{-\infty}^{p_z} J_i(p_z') dp_z' && (39) \\ J_i(p_z) &= \int\int \rho(\vec{p}) \, dp_x \, dp_y && (40) \\ J_{i0} &= J_i(p_z = 0) \end{aligned}$$

where $J_i(p_z)$ is the Compton profile of the i-th atomic shell and J_{i0} is the Compton profile of that shell with $p_z = 0$. Values for J_{i0} are tabulated. Further details on Equation (38) and on how the energy of the final state is sampled can be found in the PRM in section 10.1.2.
The azimuthal angle ϕ of the gamma is sampled uniformly over $[0, 2\pi)$. The electron is emitted with energy

$$E_e = E_i - E_f - U_i \tag{41}$$

and its azimuthal angle is $\phi_e = \phi + \pi$. The polar scattering angle of the electron θ_e is given by

$$\cos(\theta_e) = \frac{E_i - E_f\, cos(\theta)}{\sqrt{E_i^2 + E_f^2 - 2\, E_i\, E_f\, \cos(\theta)}}. \tag{42}$$

Rayleigh Scattering

The total cross section for Rayleigh scattering is calculated by

$$\sigma(E) = \pi\, r_e^2 \int_{-1}^{1} \frac{1 + \cos^2(\theta)}{2}\, FF^2(x, Z)\, d\cos(\theta) \tag{43}$$

where $FF(x, Z)$ is the atomic form factor and x an expression for the momentum transfer (see Equations (37) and (36)).
The final state is then determined by sampling $\cos(\theta)$ from

$$P(\cos(\theta)) = \frac{1 + \cos^2(\theta)}{2}\, FF^2(x, Z) \tag{44}$$

and the azimuthal angle is sampled uniformly over $[0, 2\,\pi)$.

3.4.3 LowEP Physics

The LowEP [21] model (actually "Monash University low energy photon processes", see PRM section 11) was developed as an alternative to Livermore and Penelope models for Compton scattering.
While Livermore and Penelope project the pre-collision momentum of the target electron into the plane of the photon path and are thus forced to eject the Compton electron also in this plane, the LowEP model implements a two-body fully relativistic three-dimensional scattering model to describe Compton scattering. The total cross section is acquired the same was as in section 3.4.1. The sampling of the final state is again very complex and can be studied in the PRM in section 11.1.2.

3.4.4 Interactions of Optical Photons

In GEANT4 there are two different implementations of light, "gammas" and "optical photons". Optical photons are produced when a charged particle traverses a dielectric material with a speed $v \geq c/n$ or deposits energy in a scintillating material. Optical Photons are used for light with wavelengths much larger than the typical atomic spacing, i.e., $\lambda \geq 100\,\mathrm{nm}$ and energies $E \leq 100\,\mathrm{eV}$.
Optical photons undergo three main interactions:

- Elastic scattering (Rayleigh scattering)
- Absorption
- Boundary interactions (reflection or refraction)

Rayleigh Scattering

Rayleigh scattering is mostly negligible for optical photons because the cross sections for average wavelengths are very small. It is only significant for applications where large-volume Cherenkov radiators or water Cherenkov detectors are simulated. Consequently, Rayleigh scattering of optical photons is neglected in this work.

Absorption

Absorption is important because it defines the the energy range where radiators are transparent and competes with photo-ionization. Consequently, absorption must be implemented properly when tracking optical photons.

Boundary Interactions

In the case of boundary interactions, three different cases must be defined.

- dielectric $\rightarrow$ dielectric: The photon can be reflected or refracted, including total internal reflection if applicable.
- dielectric $\rightarrow$ metal: The photon is either absorbed or reflected by the metal but will never enter the material. Absorption and reflection depend on the material properties defined by the user. In the case of absorption, a detection efficiency can be defined so that SDs made of metal can still detect optical photons.
- dielectric $\rightarrow$ black material: any material for which no optical properties are defined (e.g. a refractive index) is considered a black material by GEANT4 and will absorb any optical photons impinging on it, i.e. its track will be killed immediately.

Since Rayleigh scattering is mostly negligible and absorption is defined by the material properties entered into the simulation, only the behaviour of optical photons at surface borders remains to be discussed.
The behaviour of optical photons at surface borders involves three quantities:

- Kinematics: angle of refraction or reflection

- Dynamics: amplitude of refracted or reflected photon
- Quantum Mechanics: probability of refraction (Transmittivity T) and reflection (Reflectivity R)

Generally, GEANT4 treats optical photons as plain waves

$$\vec{E} = \vec{E}_0 e^{i\vec{k}\vec{r}-\omega t} \tag{45}$$

$$\vec{B} = \sqrt{\mu\epsilon}\frac{\vec{k}\times\vec{E}}{k} \tag{46}$$

where $\vec{E}_0$ is the amplitude vector, $k = \frac{\omega}{c}\sqrt{\mu\epsilon}$ the wave number, ω the photon frequency and $n = \sqrt{\mu\epsilon}$ is the refractive index. $\vec{E}$ and $\vec{B}$ are the electric and magnetic field components. Since the incoming ($\vec{k}$), refracted ($\vec{k'}$) and reflected ($\vec{k''}$) wave must have the same phase at the interface, the well known Fresnel law can be deduced which handles the kinematics of a surface boundary action

$$(\vec{k}\,\vec{r})_{\text{surf}} = (\vec{k'}\,\vec{r})_{\text{surf}} = (\vec{k''}\,\vec{r})_{\text{surf}} \tag{47}$$

$$k\,\sin(i) = k'\,\sin(r) = k''\,\sin(r') \tag{48}$$

with i, r, r' being the angles of incidence, refraction and reflection, respectively. This yields

$$\frac{\sin(i)}{\sin(r)} = \sqrt{\frac{\mu'\,\epsilon'}{\mu\,\epsilon}} = \frac{n'}{n}. \tag{49}$$

The dynamics can be calculated using Maxwell's equations and the continuity of the normal components of the $\vec{D}$ and $\vec{B}$ field and the tangential components of the $\vec{E}$ and $\vec{H}$ field.
For plain waves with a polarization perpendicular to the plane defined by the photon path and the normal vector of the boundary the following relations hold:

$$\frac{\vec{E}_0'}{\vec{E}_0} = \frac{2n\,\cos(i)}{n\,\cos(i) + n'\,\cos(r)} \tag{50}$$

$$\frac{\vec{E}_0''}{\vec{E}_0} = \frac{n\,\cos(i) - n'\,\cos(r)}{n\,\cos(i) + n'\,\cos(r)} \tag{51}$$

where $\frac{\mu}{\mu'} \approx 1$ was assumed which is legitimate for visible light.
For a polarization parallel to the plane of the photon path and the normal vector of the surface the relations are

$$\frac{\vec{E}_0}{\vec{E}_0} = \frac{2n\,\cos(i)}{n'\,\cos(i) + n\,\cos(r)} \tag{52}$$

$$\frac{\vec{E}_0''}{\vec{E}_0} = \frac{n'\,\cos(i) - n\,\cos(r)}{n\,\cos(i) + n'\,\cos(r)}. \tag{53}$$

For the quantum mechanical aspect, a reflectivity and transmittivity have to be calculated. This can be done using the conservation of the energy flux at the border surface. The energy current is given by

$$\vec{S} = \frac{c}{8\pi}\sqrt{\mu\,\epsilon}\,\vec{E}\times\vec{H} = \frac{c}{8\pi}\sqrt{\frac{\epsilon}{\mu}}\,\vec{E}_0^2\,\hat{k} \tag{54}$$

and the following relations must hold due to conservation of energy:

$$\begin{aligned}
\vec{S}\,\vec{u} &= \vec{S}'\,\vec{u} - \vec{S}''\,\vec{u} && (55)\\
S\,\cos(i) &= S'\,\cos(r) + S''\,\cos(i) && (56)\\
\frac{1}{\mu}\,n\,\vec{E}_0^2\,\cos(i) &= \frac{1}{\mu'}\,n'\,\vec{E}_0'^2\,\cos(r) + \frac{1}{\mu}\,n\,\vec{E}_0''^2\,\cos(i). && (57)
\end{aligned}$$

where $\vec{u}$ is the normal vector of a unit area on the interface and, if $\frac{\mu}{\mu'} \approx 1$ is assumed, T and R can be calculated as

$$T = \left(\frac{E_0'}{E_0}\right)^2\,\frac{n'\,\cos(r)}{n\,\cos(i)} \tag{58}$$

$$R = 1 - T \tag{59}$$

where T is the transmittivity and R the reflectivity.

3.5 Scintillation

Scintillation is one of the oldest and most useful methods to detect ionizing radiation. A great variety of radiations can be measured by scintillation but there are several properties which determine the optimal scintillator for specific tasks:

- kinetic energy from impinging projectiles must be converted into detectable light with the highest possible efficiency
- energy conversion into light should be as linear as possible
- the medium must be transparent to its own scintillation light
- the decay time for scintillation should be as short as possible
- the medium needs good optical qualities and must be manufacturable in practical quantities
- the refraction index should be close to glass (= 1.5) for optimal optical coupling to photon detectors (which usually have a glass or glass-like surface)

No material will fulfil all these criteria but, depending on the experiment, an optimal medium can be found. Generally, inorganic scintillators provide better light yields and linearity but lack fast response times (barring some exceptions). Organic scintillators have good response times but have inferior detection efficiency for 511 keV gammas.
The scintillation mechanism in inorganic scintillators is determined by the energy states of the crystal lattice. In a pure crystal, the band gap between valence and conduction band provides a poor mechanism to produce scintillation photons because the energy is usually high and produces photons with too much energy. Also, photons emitted by such de-excitations have exactly enough energy to excite electrons again which leads to self-absorption. Consequently, impurities are introduced into the crystal which create intermediary energy states in the band gap, called activators, which allow for electrons which were lifted from the valence to the conduction band to de-excite back into the valence band in several steps. The light produced from these steps is less energetic an more suitable for detection. These de-excitation sites are called luminescence or recombination centres [26].
When a charged particle passes through the scintillator, it will create a number of electron-hole-pairs by elevating electrons from the valence into the conduction band. Holes will drift to activator sites and ionize them because their ionization energies are lower than normal lattice sites. Electrons which encounter an ionized activator will recombine with it and create a neutral configuration in an excited state. This state will, if the transition is allowed, de-excite quickly into its ground state while emitting a photon of the corresponding wavelength.
If the transition is not allowed, the state is metastable and requires additional energy to reach a higher state from which de-excitation is possible. A possible source of additional energy is thermal energy which will result in a slow component of the light yield which is called phosphorescence. This effect is also responsible for the "afterglow" of scintillators and worsens timing capabilities. Another process competing with scintillation, called quenching, describes electrons being captured in activator sites which enables de-excitation without radiation.

The scintillator relevant to this work is cerium and calcium co-doped lutetium-yttrium oxyorthosilicate (LYSO:Ce:Ca), a high density inorganic material with a glass-like appearance. LYSO:Ce:Ca is part of the rare earth oxyorthosilicates among inorganic scintillators.

3.6 Cherenkov Effect

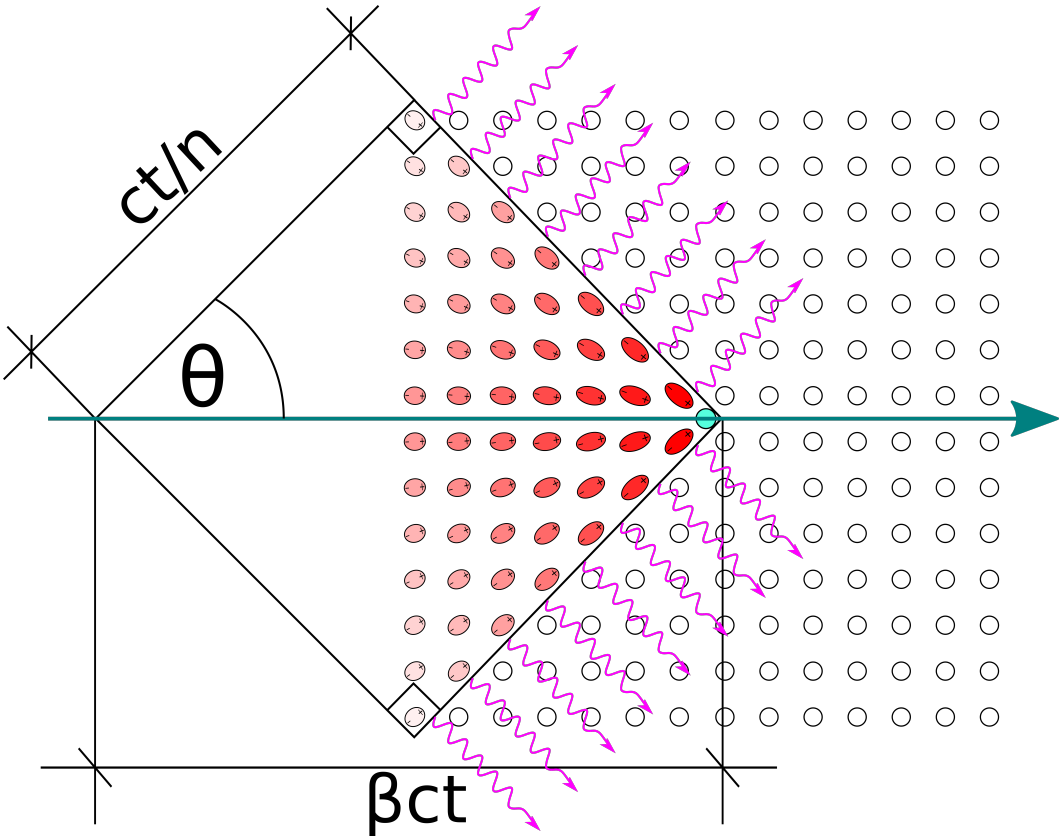

Figure 10: An illustration of the Cherenkov effect. If the particle moves with a speed $v_{\text{particle}} > c/n$ then the surrounding medium is polarized so that an electromagnetic wave is created and Cherenkov photons are emitted.

Cherenkov radiation occurs when a charged particle in a medium moves faster than the speed of light in that medium (Figure 10). Thus the minimum speed is given by

$$v = \frac{c}{n(\omega)} \tag{60}$$

where c is the speed of light in vacuum and $n(\omega)$ the refraction index of the medium as a function of the light frequency ω.

Particles with velocities $v_{\text{particle}} > \frac{c}{n(\omega)}$ polarize the surrounding medium so fast that the resulting electromagnetic waves interfere constructively which results in the emission of Cherenkov photons. This coherent electromagnetic wave front is formed at an angle θ_{C} relative to the particles trajectory which is given by

$$cos(\theta_c) = \frac{1}{\beta\, n(\omega)} \tag{61}$$

with $\beta = \frac{v_{\text{particle}}}{c}$.
Cherenkov radiation is not a very effective source of light and contributes only a few photons per primary particle to the overall photon count [26] which will also be seen in the results of this work.
The number of photons produced per path length can be calculated by

$$\frac{dN}{dx} = 2\,\pi\,z^2\,\alpha\,\sin^2(\theta_c)\int_{\lambda 1}^{\lambda 2}\frac{d\lambda}{\lambda^2} \tag{62}$$

where z is the number of elemental charges of the particle moving through the medium, α the fine structure constant, θ_c the opening angle of the Cherenkov light cone and λ the wavelength of emitted Cherenkov light.

4 GEANT4 Application and Analysis Software

The GEANT4 application developed in this work aims to accurately simulate the properties of a detector system comprising of a central cube shaped monolithic scintillation crystal with 2, 4 or all 6 of its sides in direct optical contact to DPCs. The goal is to be able to investigate several properties of the detector system and find answers to the questions:

- Can an increase in performance be expected from 6-sided readout compared to 2- and 4-sided readout?
- How do optical photons behave in the detector system based on the number of DPCs used?
- How do photon densities change with respect to different points of interaction?
- How do Cherenkov photons influence timing?
- How does the resolution of DPCs influence the performance of spatial reconstruction?

4.1 Materials

The materials used in this simulation are implemented either by using pre-defined materials from the GEANT4 material database or by defining the elements contained in a material and then creating that material as a mixture of them and with a given density. Properties such as a refractive index or scintillation are added during detector construction as well.
The DPCs are structured in a few layers of different segments, comprising only of a few different materials. The circuit board which is at the base of the DPC tile is made of a mixture of epoxy and SiO_2 called FR4 [27] which is the standard material most circuit boards are made out of. The sub-pixels which are made of pure silicon are placed on top of the circuit board and are arranged as pixels and dies according to the geometry described in the DPC manual [10]. They are then covered by a layer of acrylic based glue—the glue is implemented as pure acrylic, no detailed description of the ingredients for the glue were found—and a layer of glass. A cross section of a DPC tile and its interface with the scintillation crystal can be seen in Figure 12.
In the case of 2- or 4-sided readout faces of the scintillation crystal which are not in contact with a DPC are covered by a reflective layer to prevent optical photons from escaping the detector. For this layer, silver was used as material but its properties in the simulation do not correspond to the true properties of silver and instead are set to provide a reflectivity of $R = 1$ for all optical photons.
Information on some scintillation properties of LYSO:Ce:Ca was not found and data of LYSO:Ce was used instead. The energy spectrum of the emission intensity of LYSO:Ce was acquired at 47 points from 2.084 eV to 3.397 eV via plot-digitization from a paper by Laan et.al. [28] (see Figure 11). The absorption length was acquired the same way from the same paper at 15 points from 3.096 eV to 4.125 eV. Values for the refractive index n were acquired from a paper by Mao et.al. [29] and mapped to the energies of the emission intensity spectrum.

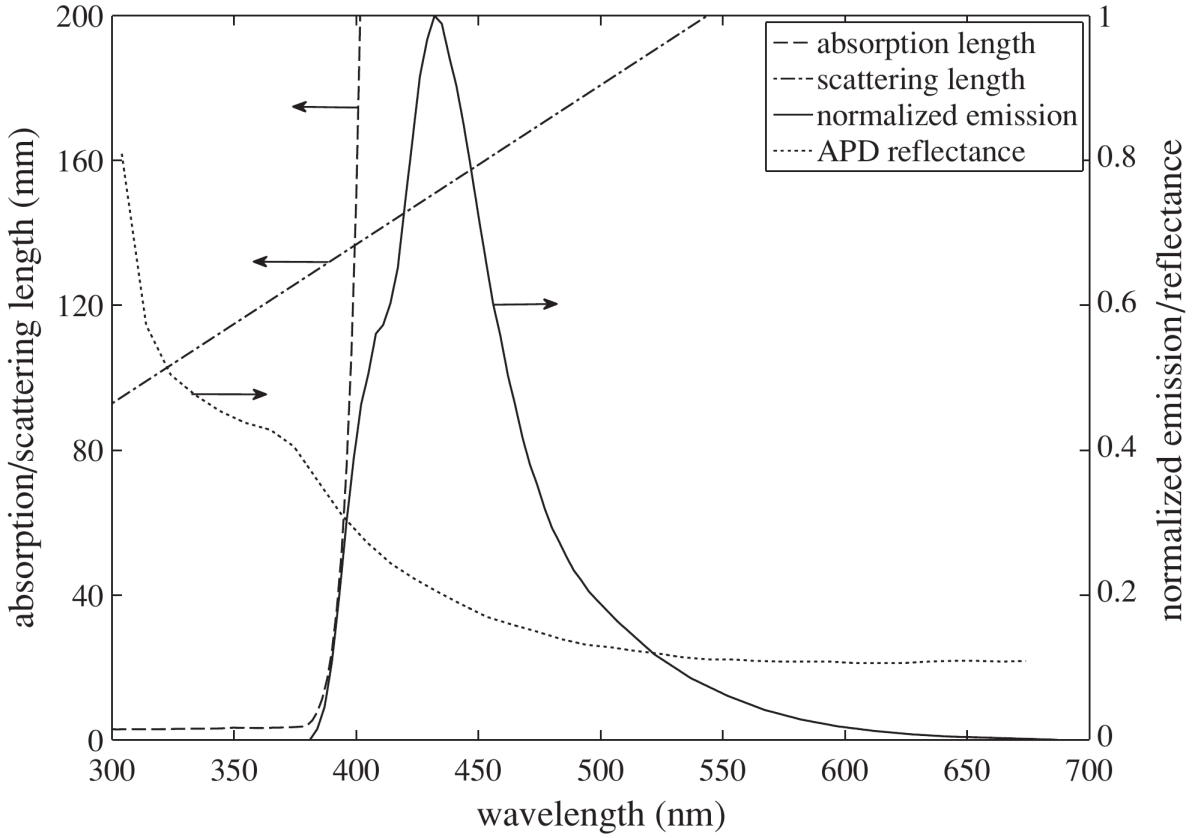

Figure 11: Emission spectrum and absorption length for LYSO:Ce [28] (Data on LYSO:Ce:Ca was not found). The graphs for reflectance and scattering length are not relevant to this work.

In order to get a broader emission spectrum of Cherenkov photons which covers the whole energy range where DPCs are sensitive, n had to be defined for a wider interval because GEANT4 only produces optical photons with energies where a refractive index of the surrounding medium is defined. The energy spectrum was extended to 1 eV at low and 5 eV at high energies and rough estimates for the corresponding values of n were acquired via linear extrapolation. The absorption length λ_{a} was extrapolated to 1 eV and 5 eV as well. As can be seen in Figure 11, λ_{a} has an almost constant value for wavelengths below ≈ 380 nm (energies of ≈ 3.25 eV) and increases extremely fast for wavelengths above ≈ 380 nm.
Light yield, fast decay time and slow decay time of LYSO:Ce:Ca were obtained from Weele et.al. [30]. According to that paper the number of detected photons for LYSO:Ce:Ca is 8260 photons/MeV when measured with a Hamamatsu R1791 PMT. This PMT has a photon detection efficiency (PDE) of ≈ 0.273 at $\lambda \approx 420$ according to Haas et.al [31]. The energy resolution achieved by Weele was 7.9 %. From these data the theoretical total light Yield Y_t and the resolution scale Δ_Y, a parameter in GEANT4 which governs the statistical fluctuation of the light yield, can be estimated.
Assuming a PDE of 0.273 the theoretical light yield is

$$Y_t = \frac{Y_m}{PDE} = \frac{8260}{0.273} = 30234. \tag{63}$$

The energy resolution is given as

$$\Delta E_{rel} = \frac{FWHM}{Y_t\, E} = 0.079 \tag{64}$$

and Δ_Y, σ and FWHM are related via

$$FWHM = 2\sqrt{2\,ln(2)}\,\sigma \tag{65}$$

$$\sigma = \Delta_Y \sqrt{Y_t\, E} \tag{66}$$

assuming a Gaussian distribution for Equation (65).
Using Equations (63), (64) and (65) the resolution scale Δ_Y can be calculated by

$$\Delta_Y = \frac{\sigma}{\sqrt{Y_t\, E}} = \frac{\frac{FWHM}{2\sqrt{2\,\ln(2)}}}{\sqrt{Y_t\, E}} = \frac{\frac{\Delta E_{rel}\, Y_t\, E}{2\sqrt{2\,\ln(2)}}}{\sqrt{Y_t\, E}} \tag{67}$$

$$= \frac{0.079\sqrt{30234 \times 0.511}}{2\sqrt{2\,\ln(2)}} \approx 4.17 \tag{68}$$

thus the standard deviation σ for the scintillation yield in the simulation is

$$\sigma = \Delta_{\mathrm{Y}} \sqrt{Y_t\, E} = 4.17\sqrt{15450} \approx 518\,[\text{photons}]. \tag{69}$$

A detailed summary of the materials and their properties can be found in the appendix in Tables 13, 14 and 15. The scintillation properties for LYSO:Ce:Ca are given in Table 16.

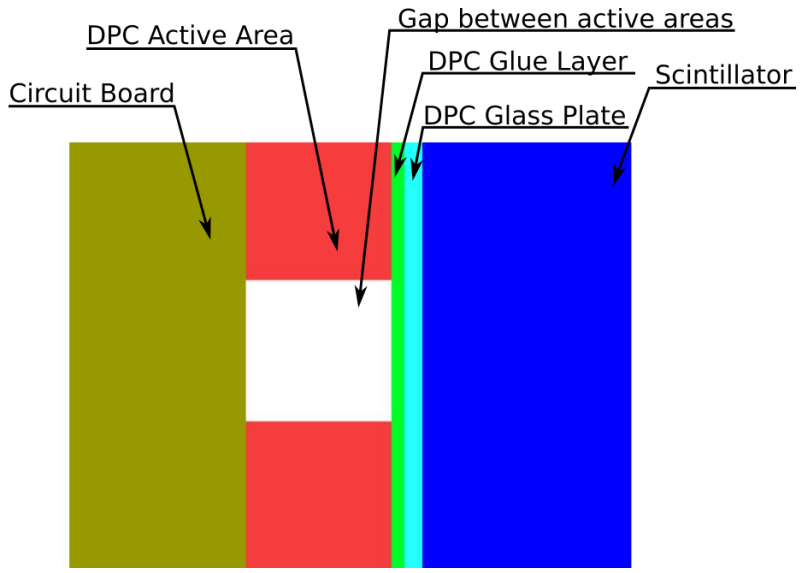

Figure 12: Cross section of the interface between the scintillation crystal and a DPC tile. The area marked as "gap between active areas" refers to any kind of gap between pixels or dies.

4.2 Detector Geometry

The geometry of the application is rather simple. The scintillation crystal is a cube shaped volume centred around the origin of the worlds coordinate system with its sides covered by DPCs as shown in Figure 13. Each DPC features an array of single photon avalanche diodes (SPAD) which are arranged in a pattern of sub-pixels, pixels and dies (see Figure 14), where each DPC contains 4×4 dies, each die contains 2×2 pixels and each pixel contains 2×2 sub-pixels. Each sub- pixel then contains 32×25 SPADs, but these are not included in the geometry explicitly. Rather, the application reconstructs the SPAD which would have been hit from the coordinates of a photon interaction on a sub-pixel. This approach greatly reduces the number of volumes in the entire detector geometry and consequently reduces computational effort. The dimensions of the DPCs were taken from the corresponding manual [10].

4.3 Primary Particle Source

The primary particle source responsible for the creation of primary particles at the beginning of an event. In this application two options for the primary generator are available and will be discussed in the following sections.
By default, the particle source, i.e. the primary generator, will produce 511 keV gamma photons, the application does however feature an option to set a custom energy for these photons.

4.3.1 Static Vertex

The first option is to use a generator with a static vertex position which is placed on the z-axis at $(0, 0, 5)$ cm of the worlds coordinate system a few cm away from the detector. Primary particles are created with a momentum $(0, 0, -1)$ and an energy of 511 keV by default. The geometry is shown in Figure 15 and described as "static vertex placement".

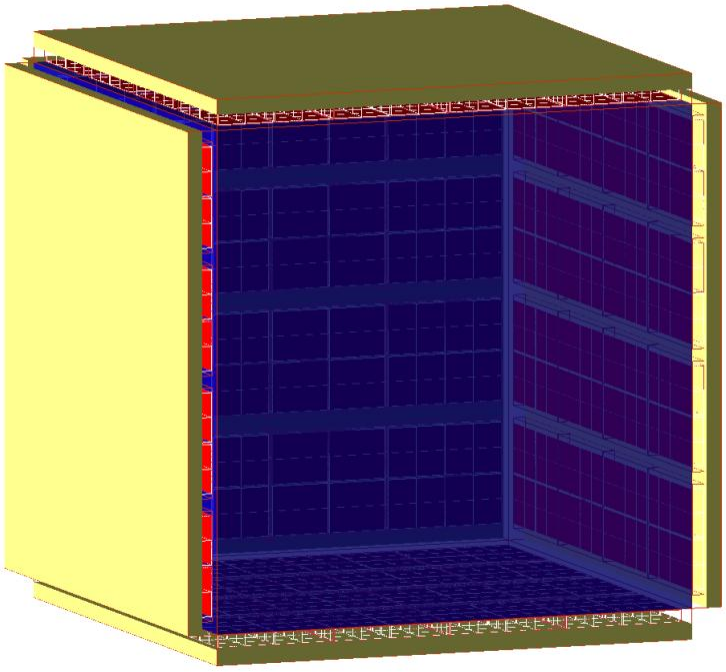

Figure 13: Structure of the detector system consisting of a central cube-shaped monolithic scintillation crystal and 6 *DPC tiles on its sides.*

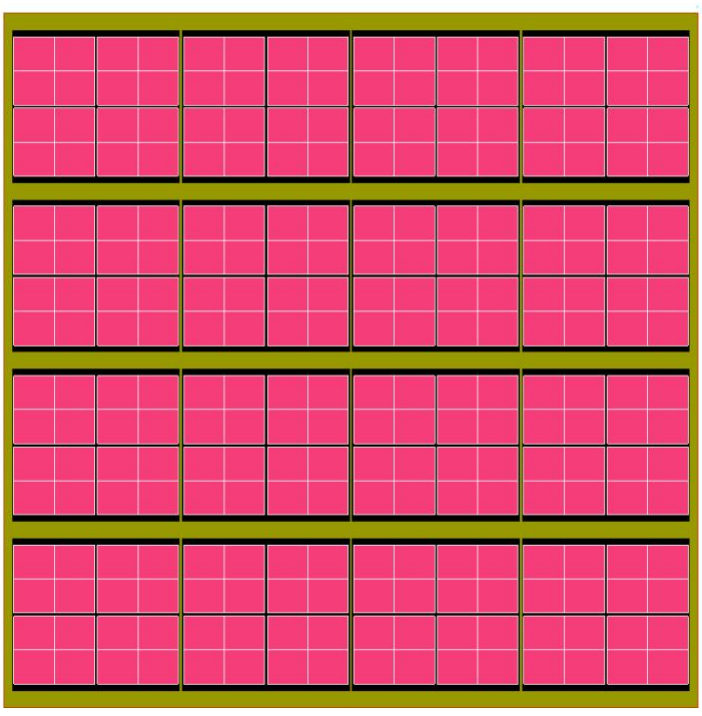

Figure 14: Shown is the structure of a single DPC tile in the GEANT4 application. The tile is segmented into 4×4 *dies which themselves contain* 2×2 *pixels. Each pixel contains* 2×2 *sub-pixels which feature* 32×25 *SPAD cells.*

This option was used to generate data for the analysis of the mean free path and energy deposit spectrum of primary particles in the scintillation crystal.

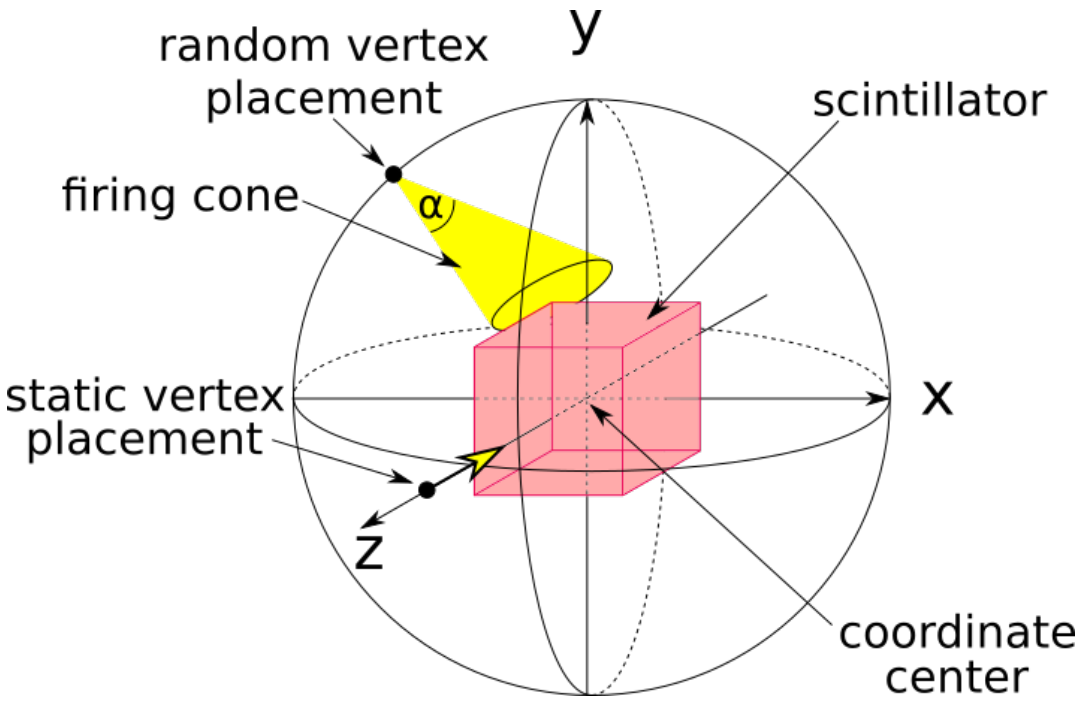

Figure 15: Shown is a sketch of the beam geometry. The application provides fixed and random vertex placement. Fixed vertices "fire" particles directly towards the coordinate center without any deviation. Randomly placed vertices "fire" towards the scintillator with a random deviation depicted as the "firing cone" which is large enough, so that the whole scintillation crystal is exposed.

4.3.2 Random Vertex

The second option for the primary generator is random vertex placement. In this case, the vertex position is changed for every event and is randomly distributed across the surface of a sphere surrounding the detector. The momenta of the primary particles point "inside" towards the center of the sphere, i.e. the center of the scintillation crystal, but a random direction is added so that particles are emitted within a "firing cone" which covers the whole detector. A sketch showing how the opening angle of this cone is calculated can be seen in Figure 16. The positioning of the random vertex and the firing cone can be seen in Figure 15 described as "random vertex placement". The opening angle is calculated by

$$r = \frac{\sqrt{3}}{2} a \tag{70}$$

$$\alpha = arcsin(\frac{r}{l}) \tag{71}$$

where r is half the length of the 3D diagonal of the cube-shaped scintillation crystal, a the length of the scintillation crystal's edges and l the distance between the primary generator vertex position and the center of the scintillator, i.e. the radius of the large sphere which defines the surface on which the primary particle vertex is placed.

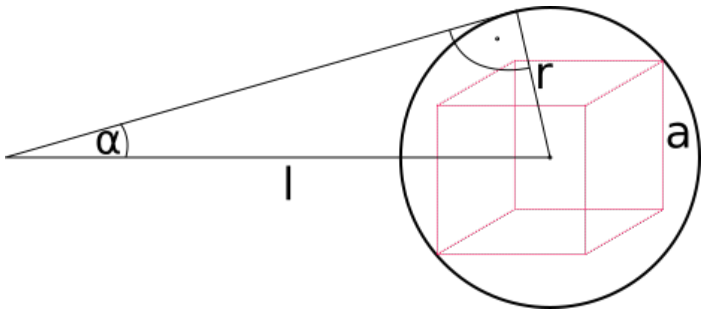

Figure 16: Geometry for the opening angle of the "firing cone". The radius r of the sphere is equal to $\frac{1}{2}\sqrt{3}\,a$ where a is the length of the scintillation crystal's edges.

4.4 Physics List

In the application developed in this work, comparatively low energetic gammas are used as primary particles and all significant processes are electromagnetic. For this case, low energy electromagnetic physics builders are most suitable. The most important such builders are

- Livermore Physics,
- Penelope Physics,
- LowEP Physics and
- EmStandardPhysics_option4.

The first three builders are discussed in section 3.4 with respect to relevant photon interactions in matter. The latter—EmStandardPhysics_option4— is used in the application of this work by default and implements the best performing models from Livermore as well as Penelope to achieve the best performance possible for low energy electromagnetic processes. Nevertheless, the application also provides the option to implement only the Livermore, Penelope or LowEP physics builder as well.
None of these builders include processes for scintillation, the Cherenkov effect or optical photons. These processes are added "by hand" in the physics list module of the application.
A very important parameter for any application is the production cut for individual particles. This parameter is defined in units of length—thus it is also called a range cut—and provides a lower limit for the range of secondary particles produced during an event, i.e. only secondary particles which will have ranges larger than the range cut will be produced. The default value set by GEANT4 is 1 mm but for this work it was set to 0.1 mm for gammas and electrons due to the comparatively low energies of the primary gammas. The value of the range cut does not influence the conservation of momentum and energy in the simulation.

4.5 Simulation Configuration Options

The data produced by the application can be modified using several parameters which are summarized in Table 2.

The number of events to be simulated can be set using the option "-nGoodEvents" and the primary energy can be specified with "-primaryE". In order to test various readout configurations, the number of DPCs can be set with "-nDPC". If more than one DPC is used, DPCs are placed on opposite sides of the scintillation crystal. Sides of the crystal which are not covered by a DPC are covered by a mirror to keep optical photons inside the detector. The geometry can be viewed using the option "-gui". However, this is not advised for data production. By default, the application will produce ROOT and ASCII output. The latter can be suppressed with the option "-noTXT".

In order to simplify the performance evaluation of the detector system, several event filters have been implemented. By default, the application will only record events, if the primary gamma deposits all its energy inside the scintillator during one interaction via photoelectric absorption (option "- singleInteractions"). If the option "-mDInteractions" is used, only events where the primary gamma deposits its full energy in several steps are recorded. If all events should be recorded irrespective of primary interactions, the option "-allInteractions" can be used. The application always processes all primary gamma interactions before any secondary tracks and then decides if an event is recorded or not. If not, the event is aborted and a new event is started to save computation time.

The particle generator mode can be chosen to either use a static vertex position ("-pencilBeam") or random vertex placement ("-randomBeam") as described in section 4.3.

Several physics builders are available and include the Livermore, Penelope, G4EmStandardPhysics_option4 and LowEP physics builders.

The options for the readout mode define how detailed the output will be. By default, the application stores all data available including which SPAD was hit by an optical photon (option "-spad"). The options "-sp" and "-tile" produce less detailed output where only the sub-pixel or tile hit by an optical photon is recorded, respectively. If only data about primary gammas and electrons are required, the option "-gammastats" can be used to suppress optical photon production and vastly increase the speed at which events are processed.

Parameter	Option	Range	Default Value
Number of simulated Events	-nGoodEvents=N	$N \in [1, 10^{10}]$	500
Primary Particle Energy [keV]	-primaryE=T	$T \in \mathbb{R}^+$	511
Number of DPCs	-nDPC=N	$N \in [1, 2, 4, 6]$	6
GUI	-gui		false
TXT Output	-noTXT		false
Event Filter	-singleInteractions -mDInteractions -allInteractions		-singleInteractions
Primary Particle Generator Mode	-pencilBeam -randomBeam		-pencilBeam
Physics Builder	-stdEM_opt4 -physList_penelope -physList_livermore -physList_lowEP		-stdEM_opt4
Readout Mode	-spad -tile -sp -gammastats		-spad

Table 2: Table of parameters which can be chosen for a simulation and their options.

The application will also create a string from all parameters relevant to the output of a simulation which is used to name configuration folders in the output folder hierarchy. For example, a simulation with

- 500 events
- 511 keV primary gammas
- 6 DPCs
- SPAD readout
- random primary particle generator
- single Interaction filter
- and the G4EmStandardPhysics_option4 physics list

will produce a folder named "stdEM4_rB_spad_sI_N500_6DPC_511keV" where "rB" stands for "randomBeam" and "sI" for "singleInteraction". The GUI and output format configuration is not added to the folder name since it has no influence on produced data. The folder hierarchy created by the application will be shown in following section.

4.6 Output

The application produces two kinds of output. On the one hand, a single ROOT file is produced for each run containing all its recorded data. On the other hand, if not suppressed, ASCII output is produced as well. The ASCII output contains separate files for each event of a run as well as one additional file containing data gathered across all events of the whole run.

The ROOT output is formatted in the typical pattern of trees and branches while the ASCII output is formatted as simple columns containing the various pieces of data.

The folder hierarchy created to store output in an organized fashion is shown in Figure 17. The output folder contains folders pertaining to various configurations of the application, which are then further divided in terms of output format and then, if ASCII output is concerned, by date.

ASCII files come in two varieties. For the whole run of a simulation where a number n of events were simulated, the application creates n files containing data about each individual event and 1 more file containing statistical data about all events, i.e. the whole run (see Figure 18). ROOT files are formatted differently in that for each run one ROOT file is created which contains data about each event as well as data for the whole run (see Figure 19).

As mentioned in section 4.2, SPAD cells are not featured explicitly in the detector system's geometry and thus, information about individual cells is not directly available—contrary to all other data gathered by the simulation. The SPAD cell which would have been hit is instead inferred from the hit position of the optical photon on the corresponding sub-pixel. A detailed explanation about this calculation can be found in the appendix in section 8.3.

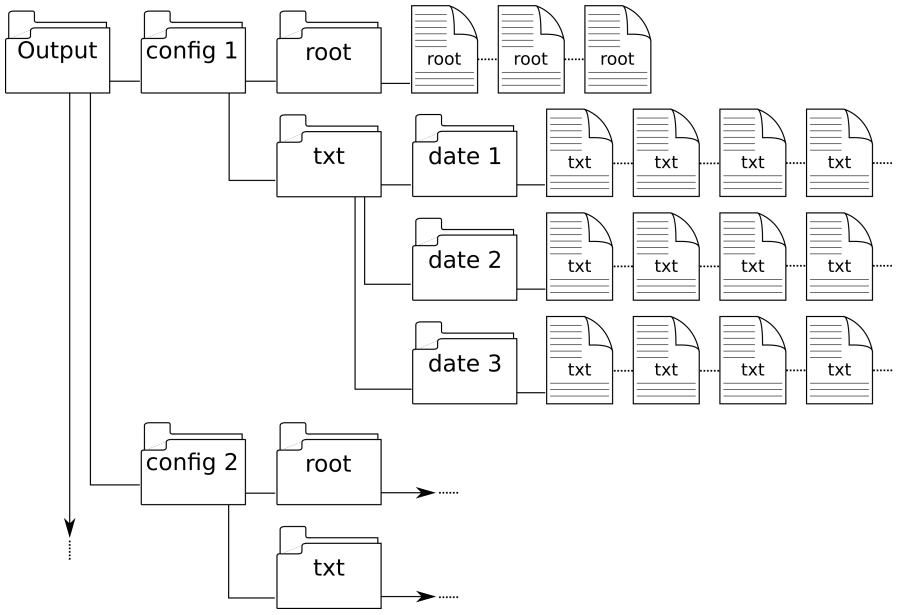

Figure 17: Shown is an outline of the file structure created by the application. Since the application can be configured in several ways (i.e. number of events, number of DPCs, type of beam, etc.) output is first sorted with respect to different configurations, then by output format. ROOT folders directly contain ROOT files for each run, TXT output is further sorted by date. Each date folder in the TXT output contains n event-data files (for each of the n events of a run) and 1 run-data file.

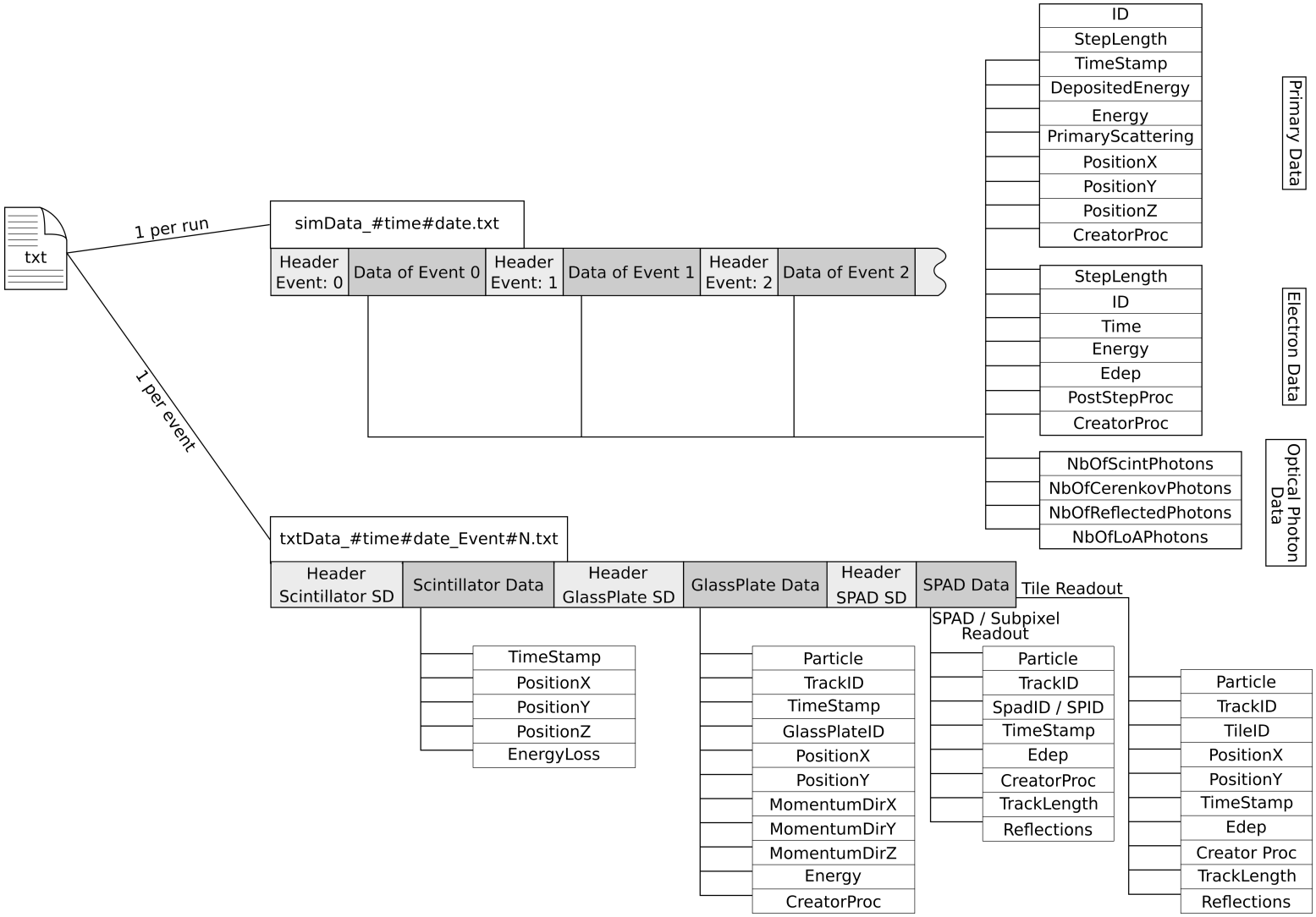

Figure 18: Shown is the Structure of TXT output files. Run-data files are structured as consecutive blocks of data for each event, respectively. Event- data files contain 3 headers which divide the TXT file into three segments. Each segment - scintillator, glass plate and SPAD - then contains several columns of data.

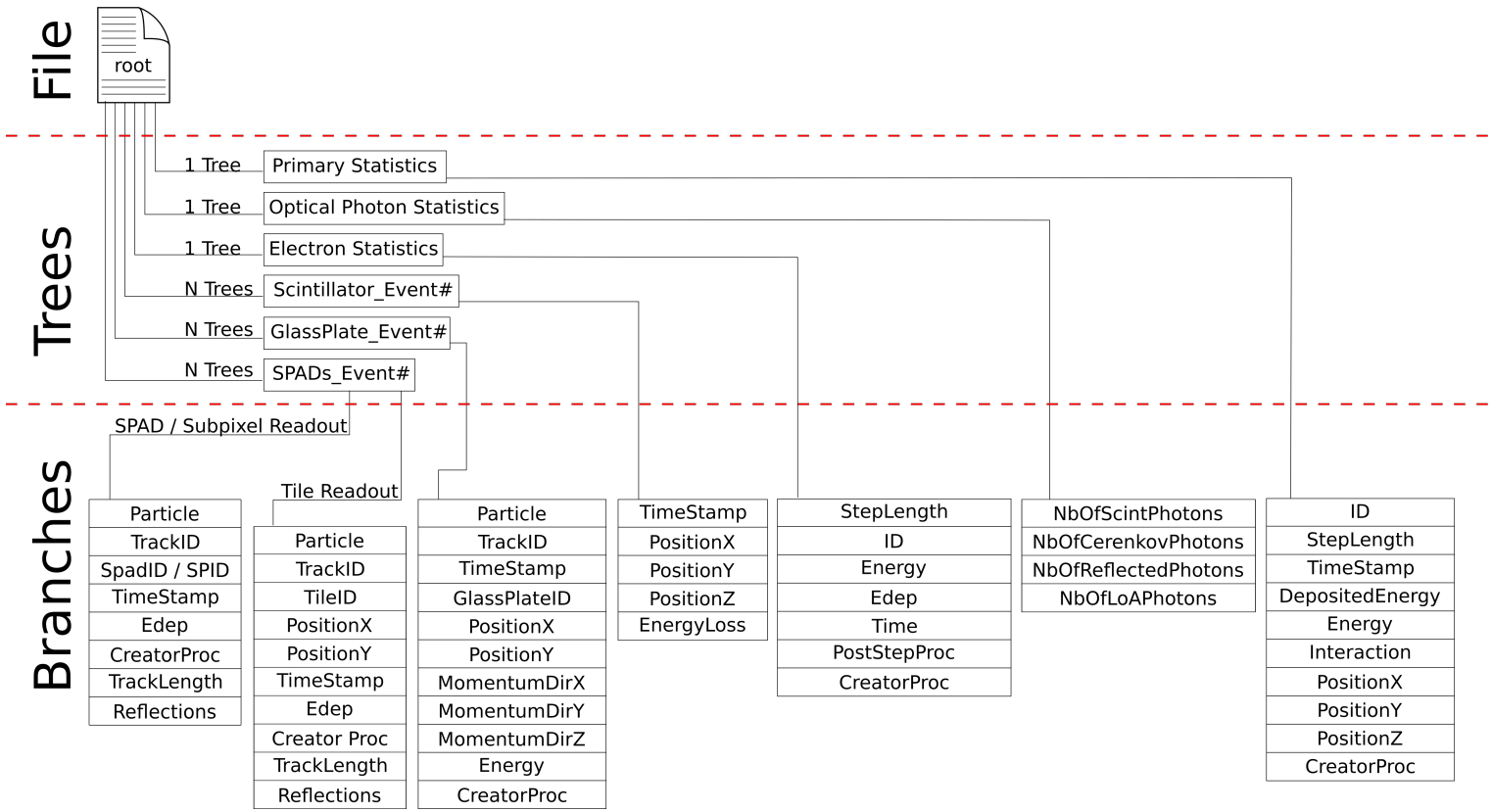

Figure 19: Shown is the structure of ROOT output files. Each ROOT file contains one tree "Primary Statistics", one tree "Electron Statistics" and one tree "Optical Photon Statistics" which contain the same data as the run-data file from the TXT output. Furthermore the ROOT file contains n scintillator-, n glass plate- and n SPAD-trees corresponding to the n events of a run. Each tree features several branches. Entries of the branches of the "Primary Statistics" or "Optical Photon Statistics" trees pertain to individual events. Entries of the branches of the scintillator-, glass plate- and SPAD- trees pertain to individual particles, i.e. primary gammas or optical photons.

4.7 A ROOT Script for Data Analysis

For this work a ROOT script was developed to read and plot various data from the ROOT files produced by the GEANT4 application. Since the same kind of analysis and plots had to be done for all the data produced by the GEANT4 application, 5 modules were written to handle various stages of data processing:

- MyDataManagement module
  - implements 6 data classes: MyScintillatorData, MyGlassPlateData, MySPADData, MyGammaData, MyElectronData and MyPhotonData
  - provides set and get methods to write to and read from objects of the data classes
- MyDataReadout module
  - find ROOT files in a given folder
  - scan a given file for trees
  - read data from trees and store them in objects of the corresponding data classes
- MyEventData module
  - collects data from various trees and branches to acquire and compute data relevant to a given event
- MyStatsData module
  - acquires data pertaining to a whole run with multiple events for statistical analyses
- MyPlotsAndGraphs module
  - provides methods to produce various plots used for data analysis

A scheme of how these modules are related to each other is shown in Figure 20.

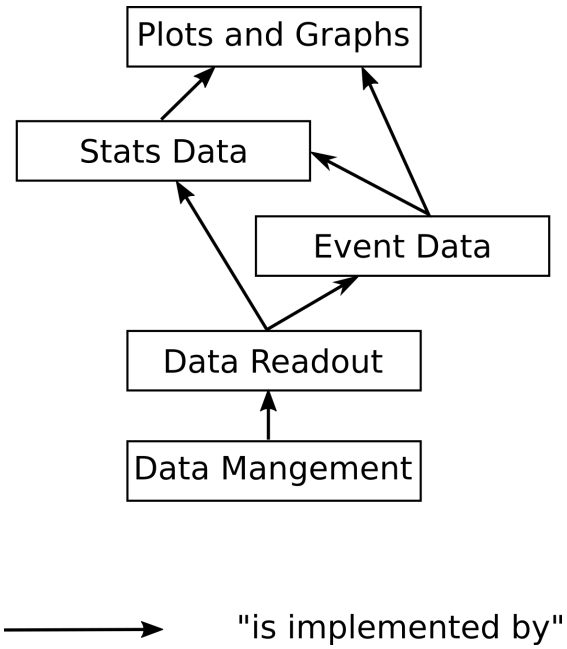

Figure 20: Relations between the various modules of the ROOT script. Arrows point form implemented modules to implementing modules.

5 Results and Discussion

So far verifying the results from the simulation by comparing them to experimental data has not been possible since no experiments with a comparable geometry have been conducted as of yet. Instead, before presenting results from this work, the plausibility of the output will be checked. This will be done by investigating the attenuation coefficient of LYSO:Ce:Ca, the energy deposit spectrum for primary gammas, the energy spectrum and range of electrons and the energy spectrum of optical photons produced in the scintillator to check, whether the physics of the application were implemented correctly.
After the plausibility of the data has been verified, the influence of Cherenkov photons on timing, the change in output when 2-sided and 4-sided readout is compared to 6-sided readout and the results for a simple COG-based spatial reconstruction algorithm will be presented.

5.1 Mean Free Path of 511keV Annihilation Gammas in LYSO:Ce:Ca

The mean free path of 511keV gammas in LYSO was plotted by using a static vertex position to irradiate the detector and adding up the path length of each primary gamma inside the scintillation crystal up to its first interaction. The resulting histogram was then fitted with a simple exponential function

$$f(x) = \exp(p_0 + p_1\, x) \tag{72}$$

with two parameters p_0 and p_1, which are a simple constant and the slope of the function, respectively. The attenuation coefficient is then given by p_1 in Figure 21.
The attenuation coefficient for LYSO (the co-doped components did not yield any different results) given by the NIST XCOM database [22] is $0.0851\,\mathrm{mm}^{-1}$. As shown by Figure 21 this value corresponds well ($\approx 3\%$ deviation) to the value yielded by the fit of the simulation data of $0.08757\,\mathrm{mm}^{-1}$.
From the fit function a particle detection efficiency PDE_{detector} can be estimated by calculating the total attenuation of the gamma beam along the full length of the crystal. This detection efficiency evaluates to

$$PDE_{\mathrm{detector}} = \frac{e^{p_0} - e^{p_0 + p_1\, x_{\mathrm{max}}}}{e^{p_0}} = 0.94 \tag{73}$$

which means that 94% of gammas will interact inside the crystal if they have to pass through the full length of the crystal. It should be noted here that in the case of random incidents, gammas may have paths through the crystal of various lengths which will influence the probability for detection.

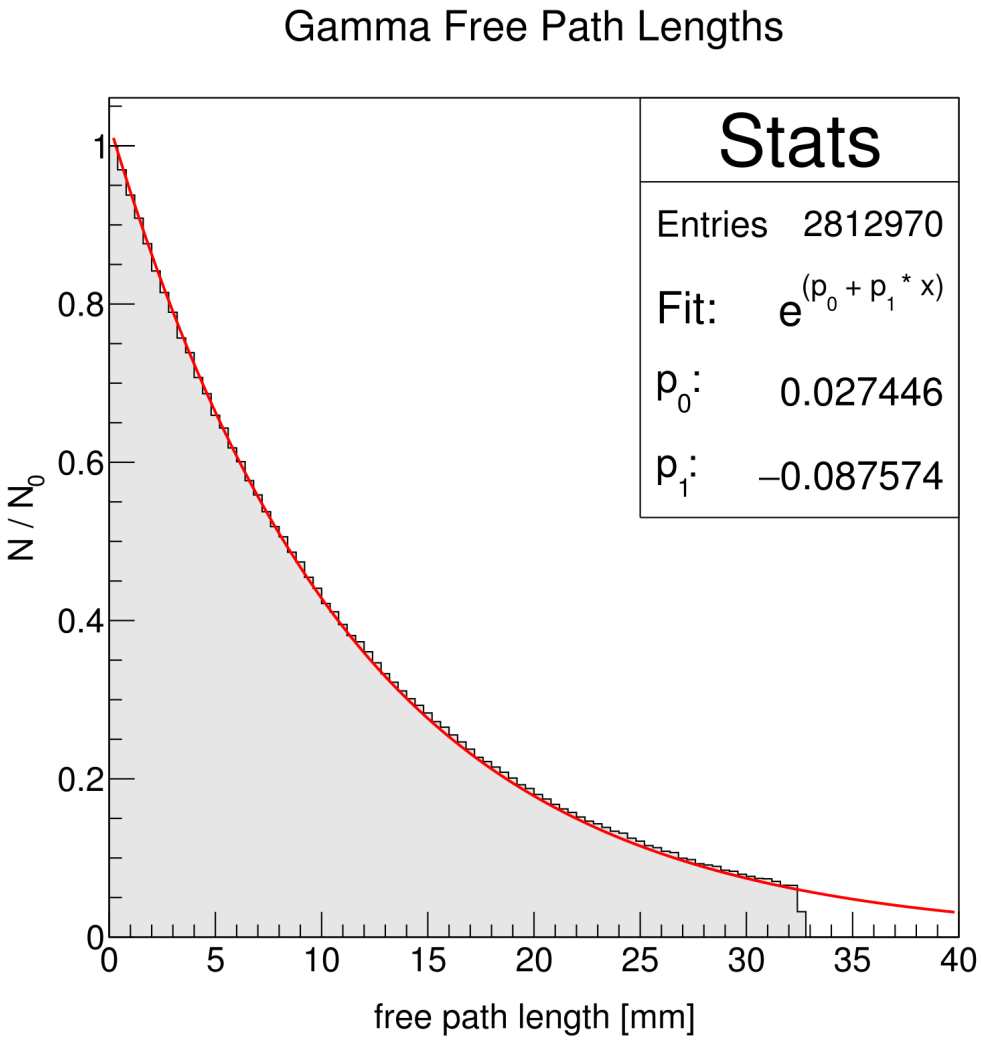

Figure 21: Histogram of the mean free path for 511 *keV gammas in LYSO:Ce:Ca. The fit curve is a simple exponential function (see Equation (72) and text for details). The "Slope" value corresponds to the attenuation coefficient.*

5.2 Energy Deposit Spectrum for 511 keV Annihilation Gammas

In order to check if various processes and models of the simulation work properly, investigating the energy deposition spectrum of the primary gammas is vital.

The "Single Compton" spectrum shows events with a single energy deposit via Compton scattering and subsequent escape of the scattered primary gamma. The Compton edge of the spectrum can be found at $\approx 340\,\text{keV}$ which agrees with the result of Equation (33) with $\theta = \pi$. The edge is not sharp due to Doppler Broadening which is included in the Livermore, Penelope and LowEP physics builders (and consequently in the EmStandardPhysics builder which is put together from Livermore and Penelope models) and is caused by the pre-collision momentum of atomic electrons.

The "Multiple Compton" spectrum shows events with two or more Compton scatterings in the scintillator followed by the primary gamma escaping the detector. The spectrum decreases fast for large energy deposits, i.e. low energies of the primary gamma, because the attenuation coefficient increases rapidly for lower ener-

gies as can be seen in Figure 24 and the primary is most likely absorbed completely.
The "Full Deposit" spectrum, i.e. the photo-peak, is located at 511 keV and contains any event where the primary gamma deposits its full energy irrespective of how it does so. Based on the height of the photo peak, 88% of gammas which interact in the scintillator are completely absorbed, i.e. the photo peak contains 88% of entries of the complete spectrum.
The "External Deposit" spectrum includes events where the primary gamma was Compton scattered before entering the scintillation crystal (forward scattering) or exited the crystal and was scattered back inside via Compton scattering (back scattering). Since only very few gammas traverse the scintillation crystal without being absorbed, most external deposits correspond to forward scattering of the primary gamma. Since the energy transfer for forward scattering is much lower than for back scattering, the spectrum is located between Compton edge and photo-peak. Also, a back-scatter peak can be identified, but it is too low to see in Figure 22. The spectrum for external deposits alone is shown in Figure 23 were a small peak at ≈ 200 keV can be seen which corresponds to back scattering. The continuum which starts at roughly 260 keV and extends to 511 keV corresponds to scattering angles $< 90\,^{\circ}$,i.e. forward scattering.
The "Gamma Escape" spectrum includes events, where one or more secondary gammas were emitted via de-excitation of ionized atoms and escaped the detector system. The two peaks which can be seen in Figure 22 correspond to the $K\alpha 1$ and $K\alpha 2$ lines of Yttrium and Lutetium, respectively.
The photo-peak in Figure 22 consists of events where 511 keV were deposited in various combinations of interactions. The ratios between these interactions can be seen in Table 3.

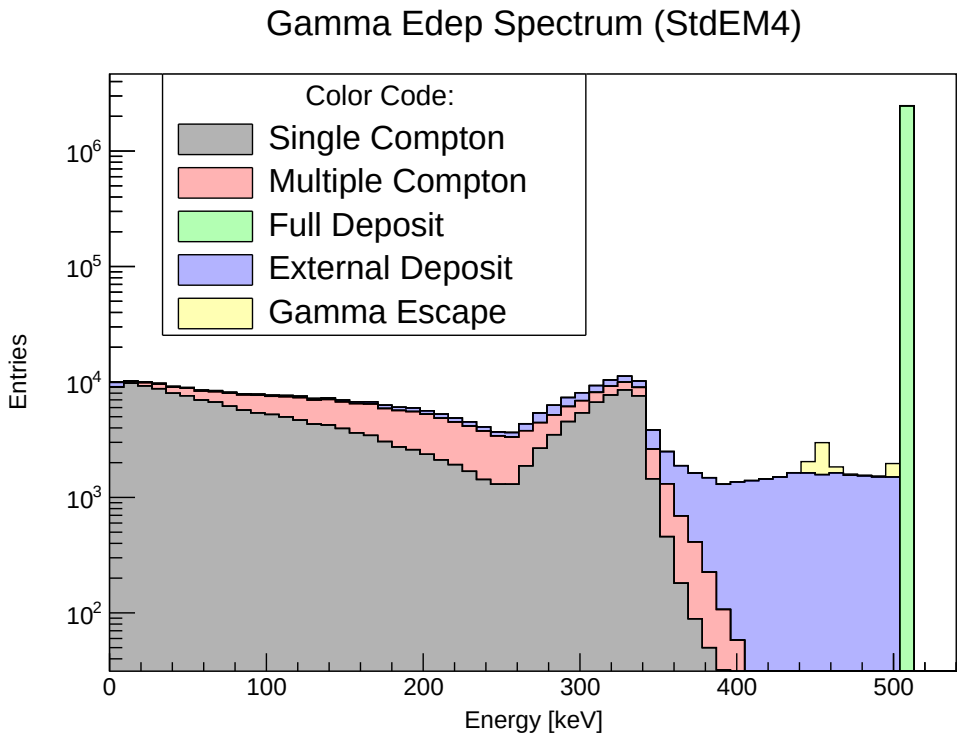

Figure 22: Gamma energy deposit spectrum segmented based on various interaction channels. All events were first sorted into separate histograms, i.e. single Compton scattering, full deposit, etc., based on the path and interactions of the primary gamma. Then these separate histograms were stacked in different colors to obtain the complete spectrum.

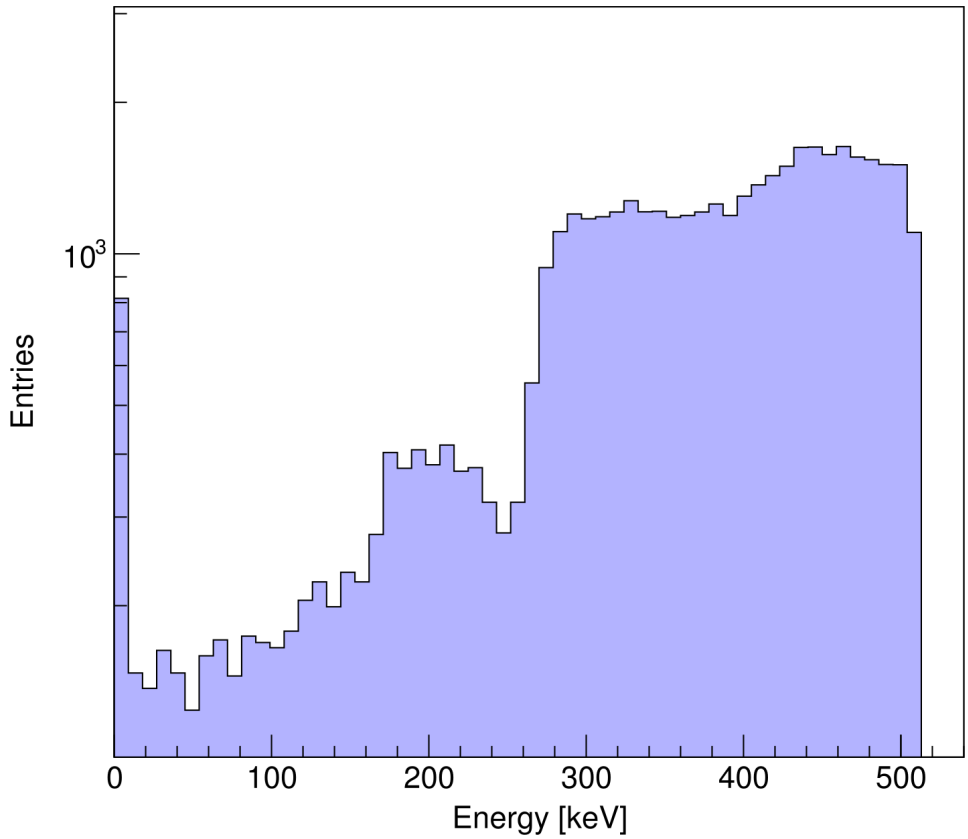

Figure 23: Spectrum of energy deposits of externally scattered primary gammas. The peak at 0 keV corresponds to gammas which have not interacted inside the scintillator after scattering externally. The peak centred around 200 keV corresponds to back scattered gammas and the continuum starting with 260 keV corresponds to forward scattered gammas (Compton energies $E_C \geq 260\,keV$ roughly correspond to scattering angles $\theta \leq 90°$) which interacted prior to entering the scintillation crystal.

Interaction	**Ratio (%)**
Immediate photo-absorption	35.7
1× Compton scattering	38.6
2× Compton scattering	18.5
3× Compton scattering	5.6
4× Compton scattering	1.0
> 4× Compton scattering	0.6

Table 3: Relative probabilities for various channels of a full energy deposition. For channels with one or more Compton scatterings, the eventual complete absorption of the primary gamma via the photoelectric effect is implied.

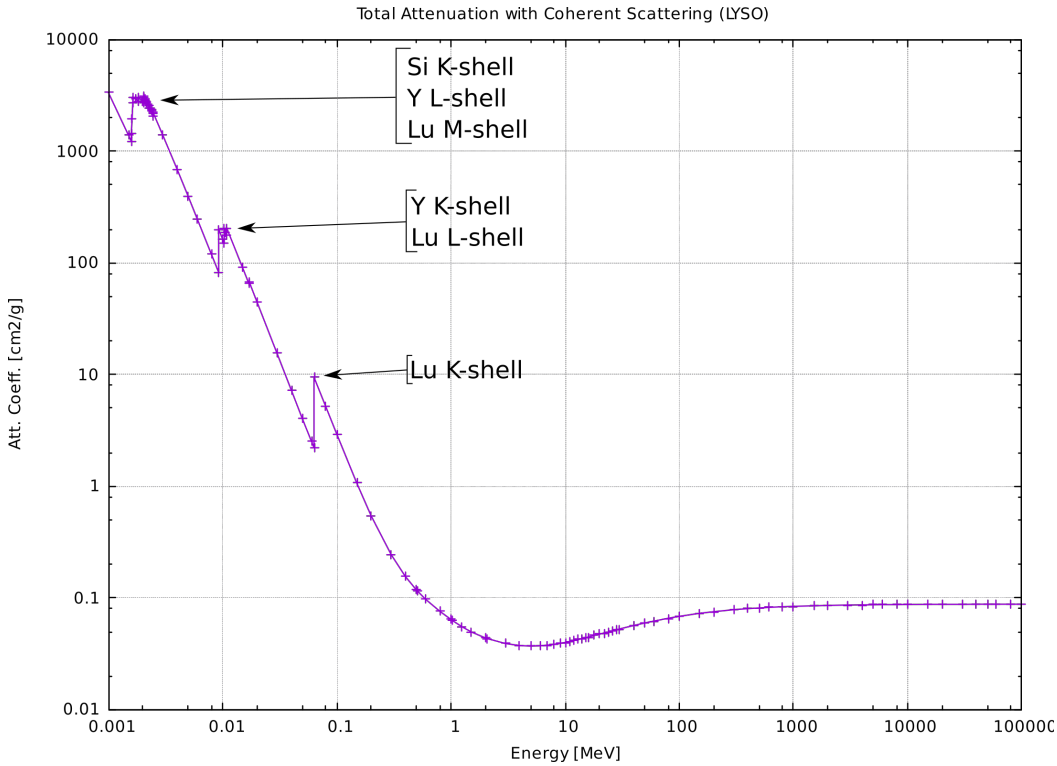

Figure 24: Shown is the development of the attenuation coefficient for LYSO. The data was acquired from NIST XCOM [22] and plotted with gnuplot [23].

5.3 Electron Range and Energy

The range of electrons in LYSO is another means to check the plausibility of the data and proper functioning of the corresponding models. In Figure 25, two plots show the electron ranges for various energy ranges. The values for mean ranges were cross checked with NIST ESTAR databases [32] where data was available. There is good correlation as shown in Table 4.

With the electron ranges a rough estimate of the expected Cherenkov yield for each event can be calculated. In many cases, secondary electrons will be ionized from Lutetium which is the main constituent of LYSO (see corresponding peak at 450 keV in Figure 25) and has a K-shell binding energy of ≈ 63 keV. Thus, if the primary gamma deposits all its energy via photoelectric absorption, a kinetic energy of ≈ 450 keV for the electron can be assumed. Such electrons will move at a speed of

$$\beta_{\text{electron}}(T) = \sqrt{1 - \left(\frac{1}{1 + \frac{T}{m_e\, c^2}} \right)^2} \tag{74}$$

$$\beta_{\text{electron}}(511) = 0.847\,[\text{c}] \tag{75}$$

where β_{electron} is the electron velocity in units of the speed of light c and m_e the electron rest mass. Also, electrons with this energy have a range of ≈ 0.331 mm (see Table 4) in the simulation. These electrons will emit Cherenkov photons until they drop below the critical velocity of $\beta_C = c/n$—which is at roughly 104 keV—with a remaining range of ≈ 0.034 mm [32]. Thus, the range for Cherenkov-emitting electrons is $r_e \approx 0.3$ mm.

The DPC is at least slightly sensitive for wavelengths from roughly $\lambda_1 = 250$ nm to $\lambda_2 = 1240$ nm and the refractive index of LYSO:Ce:Ca can be roughly estimated with $n = 1.82$. Thus, using Equations (61) and (62), a value for the Cherenkov angle θ_C and consequently an estimate of the Cherenkov yield per path length $\mathrm{d}N/\mathrm{d}x$ can be calculated:

$$\theta_C = 0.865\,[\text{rad}]$$
$$\frac{\mathrm{d}N}{\mathrm{d}x} = 84.8 \left[\frac{\text{photons}}{\text{mm}} \right].$$

The estimated Cherenkov yield during an event in the simulation is then

$$Y_C = r_e \frac{\mathrm{d}N}{\mathrm{d}x} = 25.4 \tag{76}$$

which is in very good agreement with the mean Cherenkov yield calculated from simulation data in section 5.6.

Mean Energy [keV]	EStar Range [mm]	Simulated Range [mm]
88.11	0.0276	0.0287
148.52	0.0643	0.0657
208.62	0.1092	0.1115
269.78	0.1611	0.1620
324.37	0.2110	0.2113
388.25	0.2727	0.2722
446.92	0.3316	0.3311
501.63	0.3879	0.3874

Table 4: Shown is a comparison of electron ranges in the simulation and experimental values from the NIST XCOM database [22]. The data points from NIST XCOM [22] were fitted with splines and extrapolated for the mean energies of the intervals shown in the bottom picture in Figure 25. For higher energies simulation and experimental data agree increasingly better.

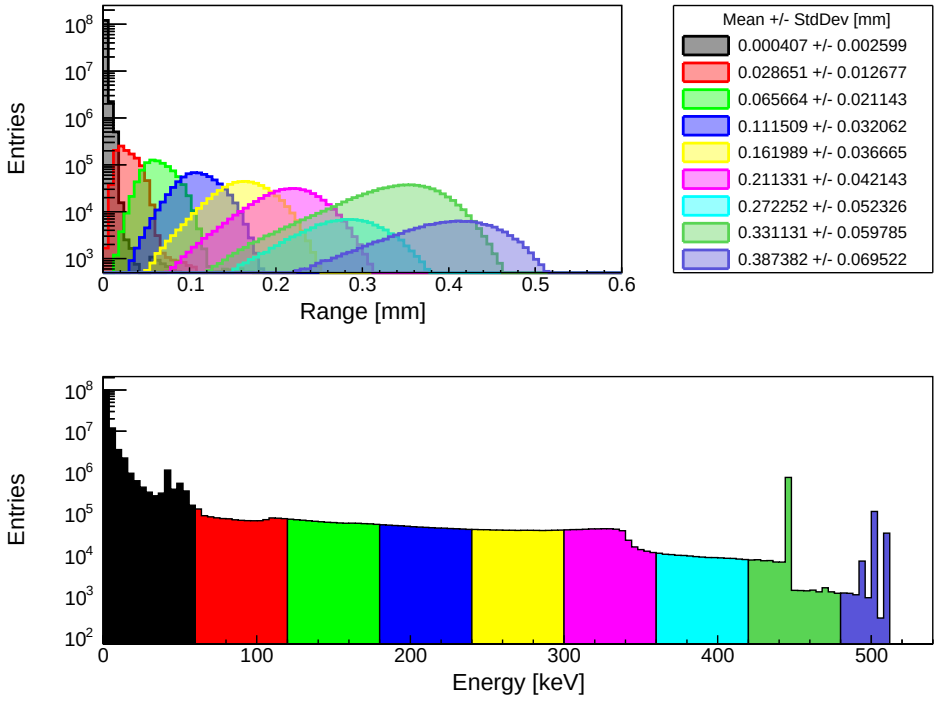

Figure 25: Shown are the ranges and energies of electrons produced in the scintillation crystal by primary gamma interactions. The Compton edge can be seen at $\approx 340\,keV$ as well as various peaks at high energies corresponding to the binding energies of constituents of LYSO:Ce:Ca. The colouring of the energy spectrum corresponds to the colouring of the range spectra.

5.4 Scintillation and Cherenkov Energy Spectrum

The refractive index for LYSO was given for an energy range of 1-5 eV because GEANT only produces optical photons for energies where a refractive index is defined.
In Figure 26 both spectra for photons detected by the DPCs of the simulation can be seen.
At $\approx$ 3 eV the absorption length for optical photons in LYSO:Ce:Ca drops to $\approx$ 2 mm which causes the sudden decrease in detected Cherenkov photons. The scintillation spectrum and the absorption length narrowly overlap and and some scintillation photons are self-absorbed as well by the scintillator.
Since the Cherenkov yield is proportional to the wavelength by λ^{-2} one would expect the Cherenkov count to increase from 1 eV to 3 eV. This is not the case because the refractive index of LYSO only changes by $\approx 6\%$ across the defined energy range (even including extrapolated values for 1 eV and 5 eV) which results in such a small increase of Cherenkov photons that it is compensated by the continuously shortening absorption length. A plot of the emission spectrum and absorption length for LYSO:Ce:Ca can be seen in Figure 11.
For this sections and analyses concerning optical photos in general, a quantum efficiency of 100 % was used unless stated otherwise. The convention for the relation between quantum efficiency QE, fill factor FF and particle detection efficiency PDE in this work is

$$PDE = QE \times FF. \tag{77}$$

The fill factor has a fixed value of ≈ 0.73 for all analyses and is determined by the DPC geometry.

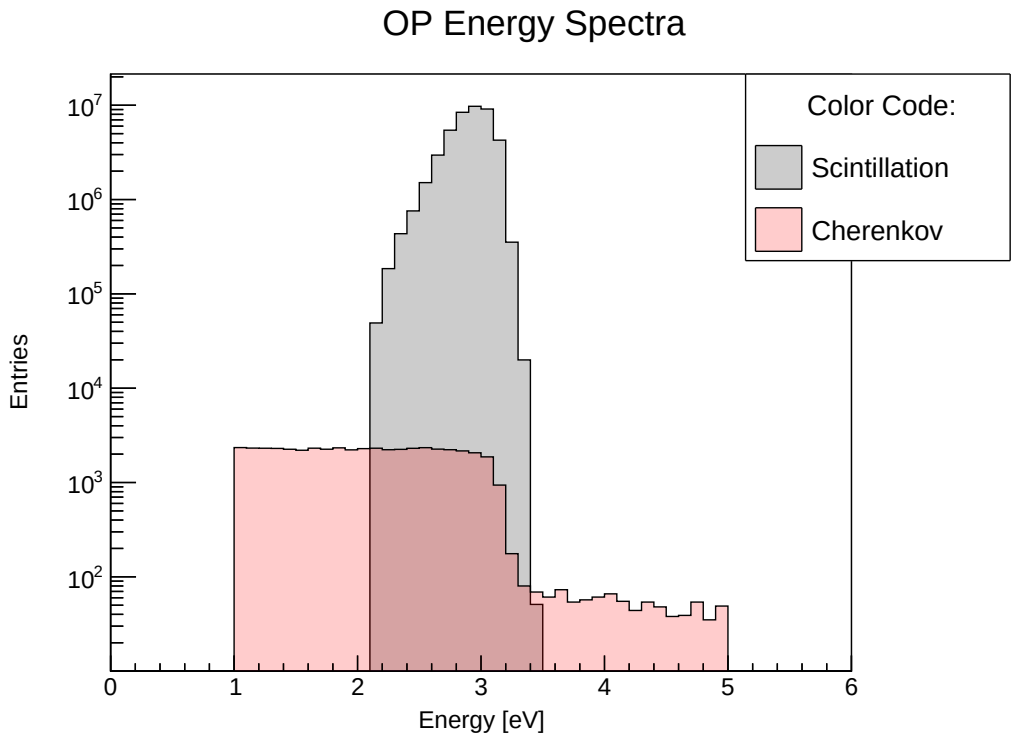

Figure 26: Shown are the energy spectra of scintillation and Cherenkov photons. The plateau of Cherenkov photon counts from 1 eV to 3 eV is caused by a rather stable refractive index of LYSO over the concerned energy range.

5.5 POI Distribution

Although it is irrelevant to plausibility, the distribution of POIs over the whole detector system when simulating events with random incident must be investigated to guarantee that reconstruction algorithms can be tested against events which are distributed over the whole scintillation crystal.
The particle generator of the application features a randomly placed primary vertex for this purpose (see section 4.3). In Figure 27 the spatial distribution of 6000 POIs is shown. One can see, that the data is roughly centred around the coordinate origin and has a standard deviation of $\approx 9 - 10$mm.
The mean value for the z-coordinate is further off the center than the x- and y- coordinate and the standard deviation is larger as well but this should not have a detrimental effect on the analysis of reconstruction algorithms. The most important feature is that the POI distribution covers the whole volume of the scintillation crystal so that a great variety in POIs can be expected when simulating events with random incidents.

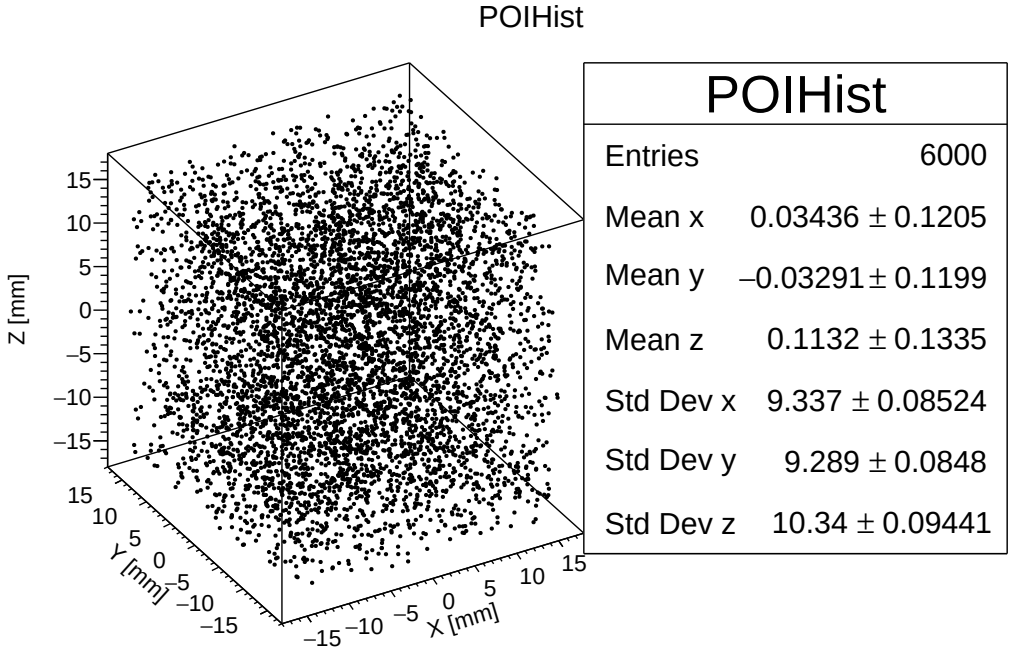

Figure 27: Shown is a plot of the spatial distribution of POIs in the scintillator when using a random primary particle incident vector.

5.6 Optical Photon Statistics

Now that the plausibility of the data has been established, first results of the simulation can be shown.
For statistical and timing purposes it is important to know the number of scintillation photons and Cherenkov photons per valid event, i.e., full energy deposition of the 511 keV primary gamma. Also, the number of photons which have been reflected before being detected is of interest when analytical POI reconstruction is concerned because the geometrical information for analytical reconstruction is lost, once the photon has been reflected. In Figure 32 the distributions of various photon counts are shown. All data in this chapter was produced with a quantum efficiency of 100% and a detector geometry featuring all 6 DPCs.

The distribution of the scintillation yield in Figure 28(a) is centred around 15500 photons which is roughly half of the yield per MeV specified in the application and to be expected for 511keV gammas. The width of the distribution was specified in the application based on experimental results (see calculation at end of section 3.5).
An interesting piece of information is the mean number of Cherenkov photons (Figure 28(b)), which might influence the temporal reconstruction of scintillation events because Cherenkov photons are produced faster than scintillation photons. During real acquisition the DPC only records time stamps of the first photon detected on each die which means, that Cherenkov photons might have a disproportionately large influence on time stamps despite their low numbers.
When analytical POI reconstruction is concerned, the number of reflected photons (see Figure 28(c)) is important because these photons no longer carry any geometrical information that an analytical code such as COG could use. Thus, for a more precise analytical reconstruction, reflections should be kept low. On the other hand, k-NN methods rely on photon count distributions as a whole and perform better if all photons are kept inside the scintillator, even reflected ones [12].
The number of photons which were lost or absorbed (Figure 28(d)) gives an idea of how many photons are available for evaluation even if the quantum efficiency is 100%. It is important to note here, that "absorbed" refers only to optical photons which were reabsorbed by the scintillation crystal. Photons are counted as lost if they leave the scintillator before they are detected either by hitting a gap between pixels of dies or by leaving the detector at the edges of the scintillation crystal (which happens only rarely).
Finally, the number of photons measured by the DPC (Figures 28(e) and 28(f)) is centred around 8600 photons which is due to the geometric fill factor of the DPC of $\approx 73\%$ and photons which were lost or absorbed. The same is true for the number of measured Cherenkov photons, where some photons are lost as well due to the filling factor of the DPCs and absorption.
When comparing these results to results for a 2-sided and 4-sided readout geometry, several observations can be made (see Table 5). While the numbers for detected scintillation and Cherenkov photons drop, the numbers for reflected and lost or absorbed photons increase. This is to be expected since those sides of the scintillation crystal which are not covered by a DPC are covered by a reflective layer instead. Consequently, photons are reflected more often and thus travel through the scintillation crystal longer which increases the probability for absorption and fewer photons are detected. Based on these results, a better performance for k-NN algorithms (because of the higher number of detected photons) and analytic algorithms alike (because of the lower number of reflected photons) can be expected for a 6-sided readout configuration. Additionally, the lower number of reflected photons might also improve timing since photons have a better chance of being detected immediately in a 6-sided readout geometry.

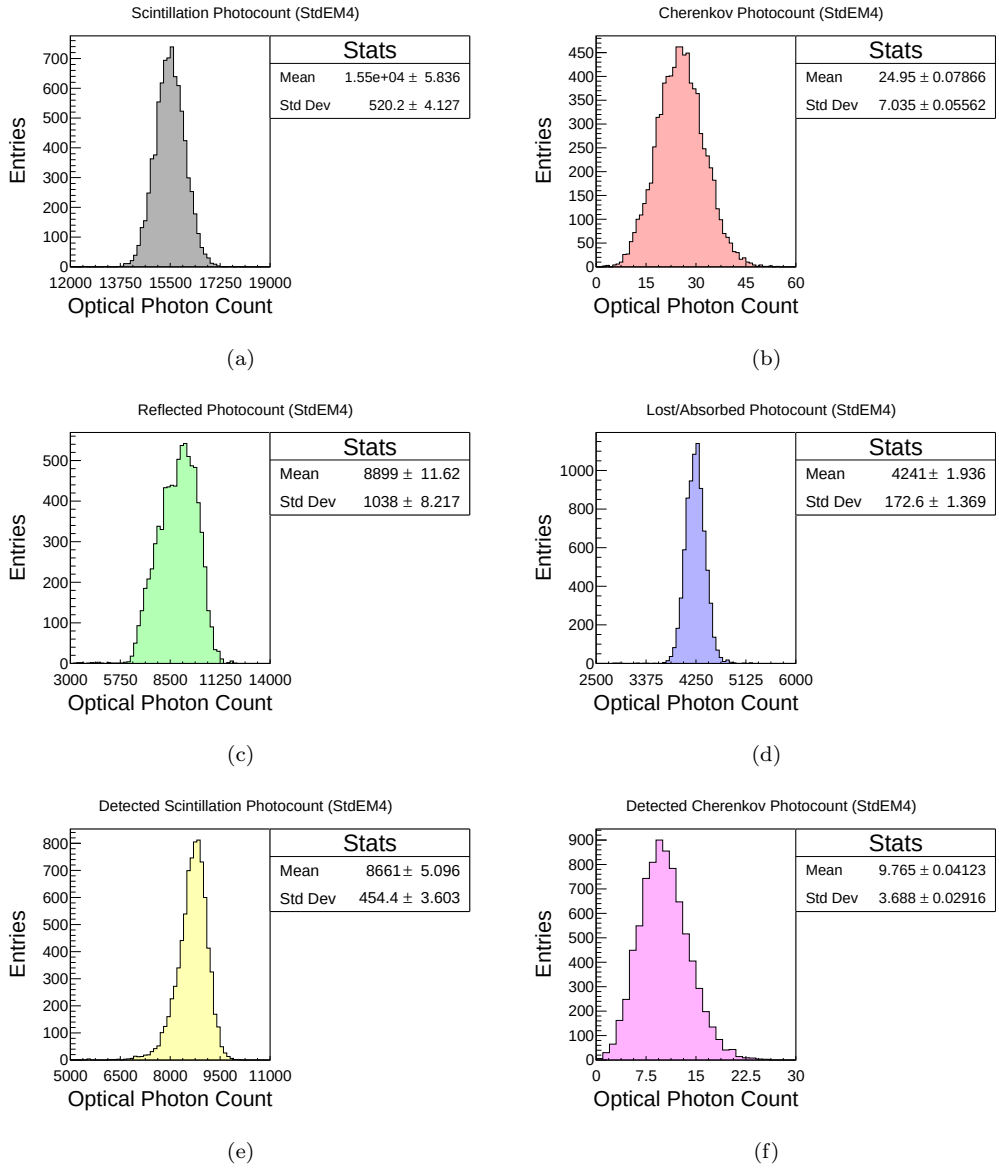

Figure 28: Shown are the optical photon count distributions for a 6-sided readout geometry and 100% quantum efficiency. Figures 28(a) and 28(b) show the number of produced scintillation and Cherenkov photons, respectively. Figure 28(c) shows the number of reflected and Figure 28(d) the number of lost or absorbed photons. Figures 28(e) and 28(f) show the number of detected scintillation and Cherenkov photons, respectively.

Readout Geometry	**Det. Scintillation**	**Det. Cherenkov**	**Reflected**	**Lost / Abs.**
2-sided	-24%	-9.1%	$+35\%$	$+65\%$
4-sided	-9.2%	-3.7%	$+17.5\%$	$+22\%$

Table 5: Shown are the changes for detected scintillation and Cherenkov photons as well as reflected and lost/absorbed photons for 2-sided and 4-sided readout compared to 6-sided readout.

5.7 Arrival Times for Scintillation and Cherenkov Photons

While the POI reconstruction inside the detector itself relies on photon count distributions, the image reconstruction in, e.g., TOF-PET systems relies on the reconstructed interaction times of annihilation gamma pairs. Thus, determining not only the POI but also the time of interaction (TOI) is important.
As mentioned in section 5.6, it is important to investigate the influence of Cherenkov photons on the detection time distribution in order to get an estimate of the inherent time resolution of the detector system.
Since time stamps are generated from the first photon interaction on a die, Cherenkov photons have a disproportionately large influence on mean arrival times of first photons despite their small number. In Figure 29(a), one can see the arrival time histogram for the first photon detected in the whole detector system during an event and that a very large amount of these photons were produced by the Cherenkov effect.
The fraction of Cherenkov photons decreases quickly for photons detected later (see Figures 29(b) and 29(c)). Since the QE of the real detector system is less than 100% and the trigger threshold of the DPC can be adjusted as well, photons which arrive later at the detector are still relevant for time stamp generation.
The development of the standard deviation of time stamps for the n-th scintillation and Cherenkov photon can be seen in Figure 30. While there is a steady increase for scintillation photons, the standard deviation for Cherenkov photons does not increase beyond the 10th photon. However, its large fluctuations indicate that statistics rapidly deteriorate for later photons. The total standard deviation refers to the standard deviation of the distribution if no distinction between scintillation and Cherenkov photons is made. It mostly follows the development of the scintillation standard deviation since most photons are scintillation photons.
In Figure 31 the development of the mean arrival time for all photons of an event are shown and indicates that, including errors, roughly 200 ns pass until all optical photons are detected which would give a theoretical detection rate capability of the detector system with 6-sided readout of 5 MHz.
Concerning the influence of Cherenkov photons on timing, it has to be noted, that a total of 96 dies from all 6 DPCs will produce time stamps while the mean number of measured Cherenkov photons per event is ≈ 10 which means that the mean ratio of time stamps created from Cherenkov photons will only be roughly 10% (see mean number of detected Cherenkov photons in Figure 28(f)).

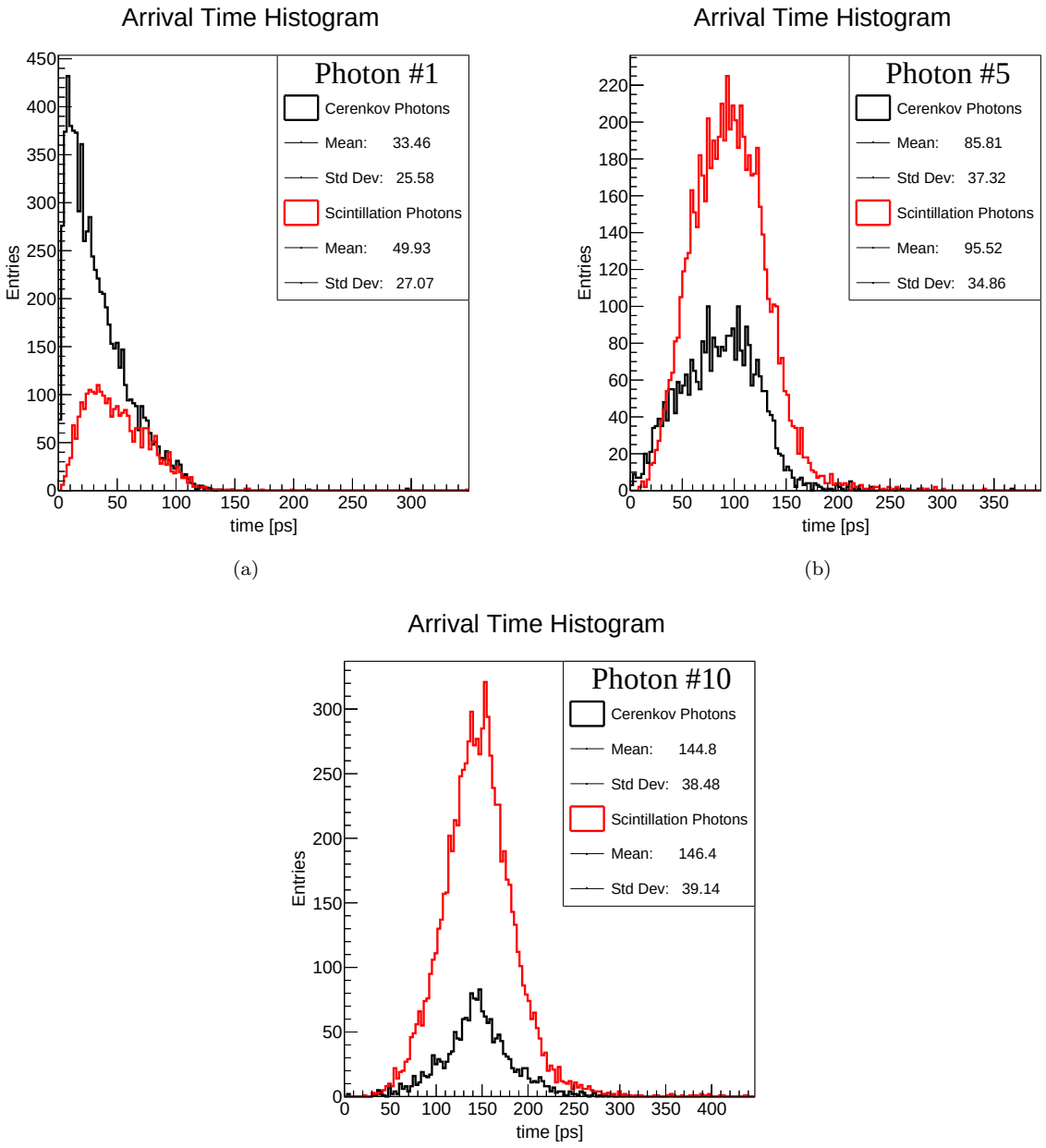

Figure 29: Shown are the arrival time histograms for the first, 5th and 10th photon detected by a detector system with 6-sided readout configuration.

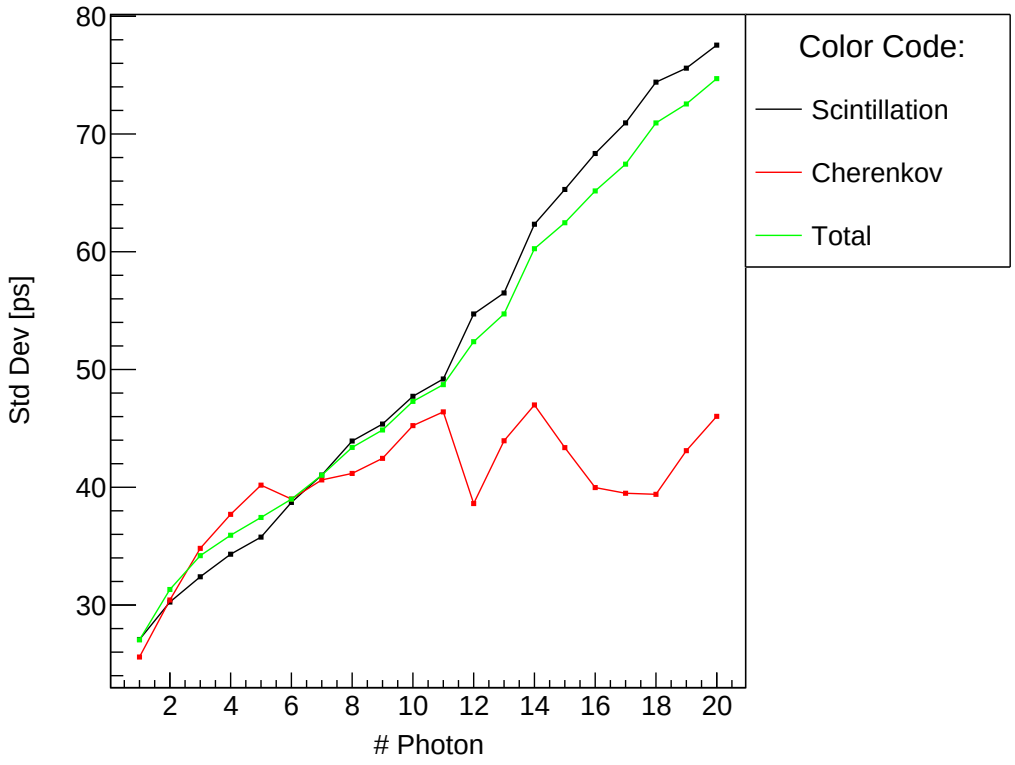

Figure 30: Development of the standard deviation which corresponds directly to the inherent time resolution of the detector system. The graph for the total deviation corresponds to the standard deviation of the total time distribution of the added scintillation and Cherenkov arrival-time histograms.

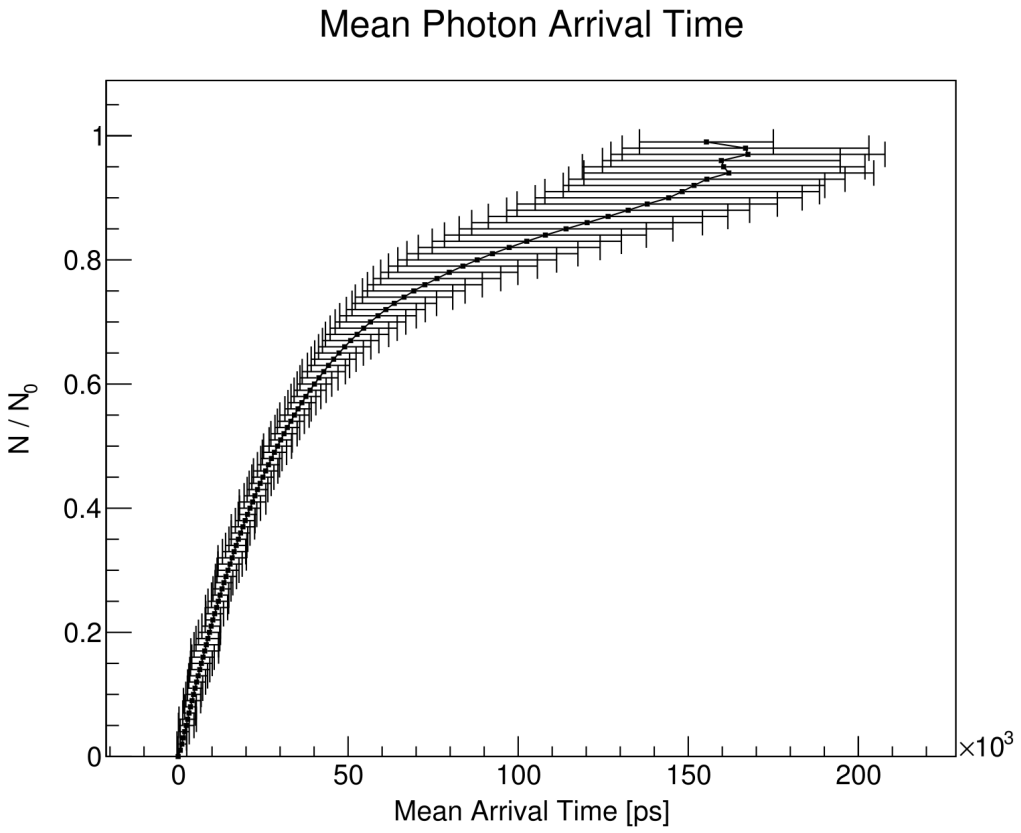

Figure 31: Shown is a plot of the mean arrival time and corresponding standard deviation for all photons detected in the detector system (6-sided readout, 100 % QE).

5.8 Pixel Count Arrays

Reconstructing the POI of an event is necessary to correct time stamps of dies for the photon path length, i.e. the time it took the photon to get from the POI to the die. Consequently, the precision of reconstructed TOIs depends on the precision of reconstructed POIs. While k-NN methods have proved to reach accuracies or $\approx 1.5\,\text{mm}$ FWHM [13], they require extensive calibration and computing power which is why analytic methods would be a welcome alternative. Even an analytic algorithm with mediocre accuracy can still vastly improve the speed of k-NN methods by reducing the search space for look up tables.

One problem for analytic methods is the large amount of reflected photons which carry no geometrical information any more but still contribute to all calculations. It is because of this "background" of reflected photons that center of gravity methods often yield insufficient results.

As can be seen in Figure 32 for small DOIs the photon count array (PCA) is extremely peaked and COG will yield a very precise result. Yet, for larger DOIs the peak diminishes and the background of reflected photons, which is quite evenly distributed over the whole array, increases relatively to the peak. For events close to the center of the scintillation crystal, the background is not a problem. This changes for off-center events where the background is not equally strong at all sides around the peak which results in the background biasing the COG towards the center and, since the background increases with larger DOIs, this bias increases with the DOI as well.

The colouring in Figure 32 indicates time information. Darker bins have been hit earlier by their first photon. While for small DOIs the time stamp distribution seems to correlate with peaks, i.e. most bins with dark shading are part of the peak, this is not the case anymore for Figure 32(d). This might be caused by the background of reflected photons which is much higher relative to the peak compared to PCAs with smaller DOIs.

The peak value P is used to measure the *peakedness* of PCAs and is implemented as a weighting factor in an approach for analytical reconstruction of the DOI.

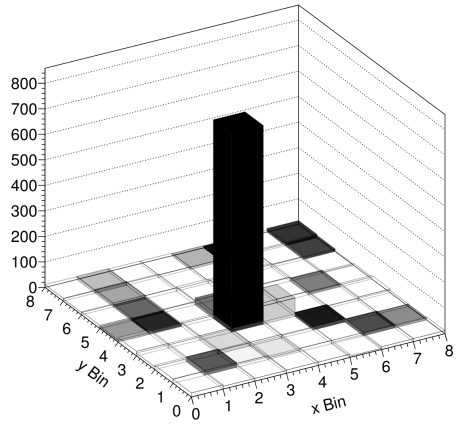

(a) Pixel count distribution at a DOI of $\approx 1\,\text{mm}$.

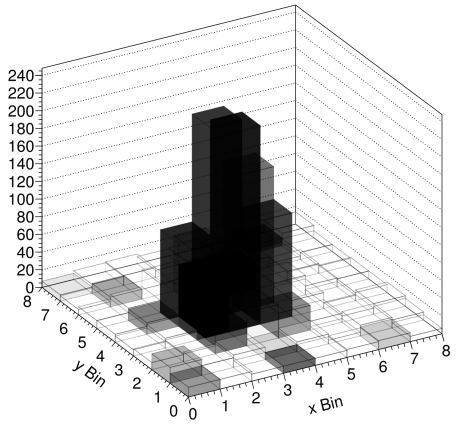

(b) Pixel count distribution at a DOI of $\approx 4\,\text{mm}$.

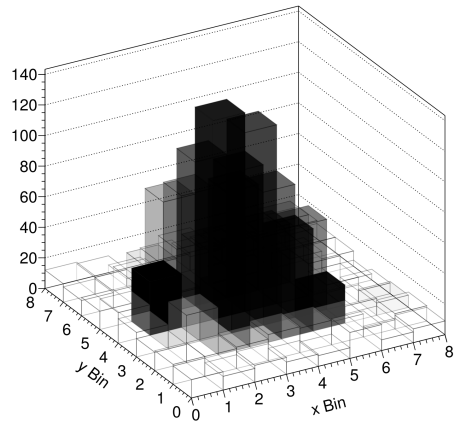

(c) Pixel count distribution at a DOI of $\approx 8\,\text{mm}$.

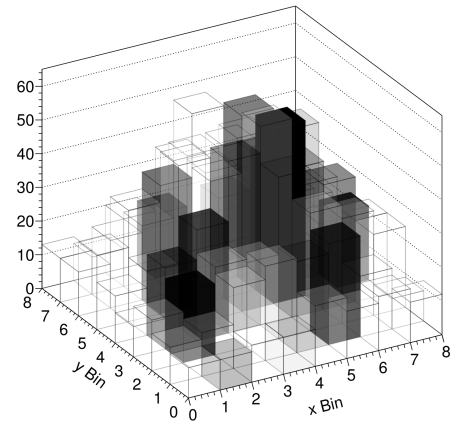

(d) Pixel count distribution at a DOI of $\approx 12\,\text{mm}$.

Figure 32: Shown are pixel photon count distributions for various normal distances between scintillation event and DPC (DOI). The vertical axis indicates the photon count of the bins.

5.9 Correlation between Peak Value and DOI

For the data displayed in this section, only events where the primary gamma interacted only once via the photoelectric effect in the scintillator, i.e. single interaction events, were used to make the analysis easier. In Figure 33 the correlation between relative peak value and DOI are shown for various powers with which the peak was calculated. For details see section 3.3 and Equation (25).

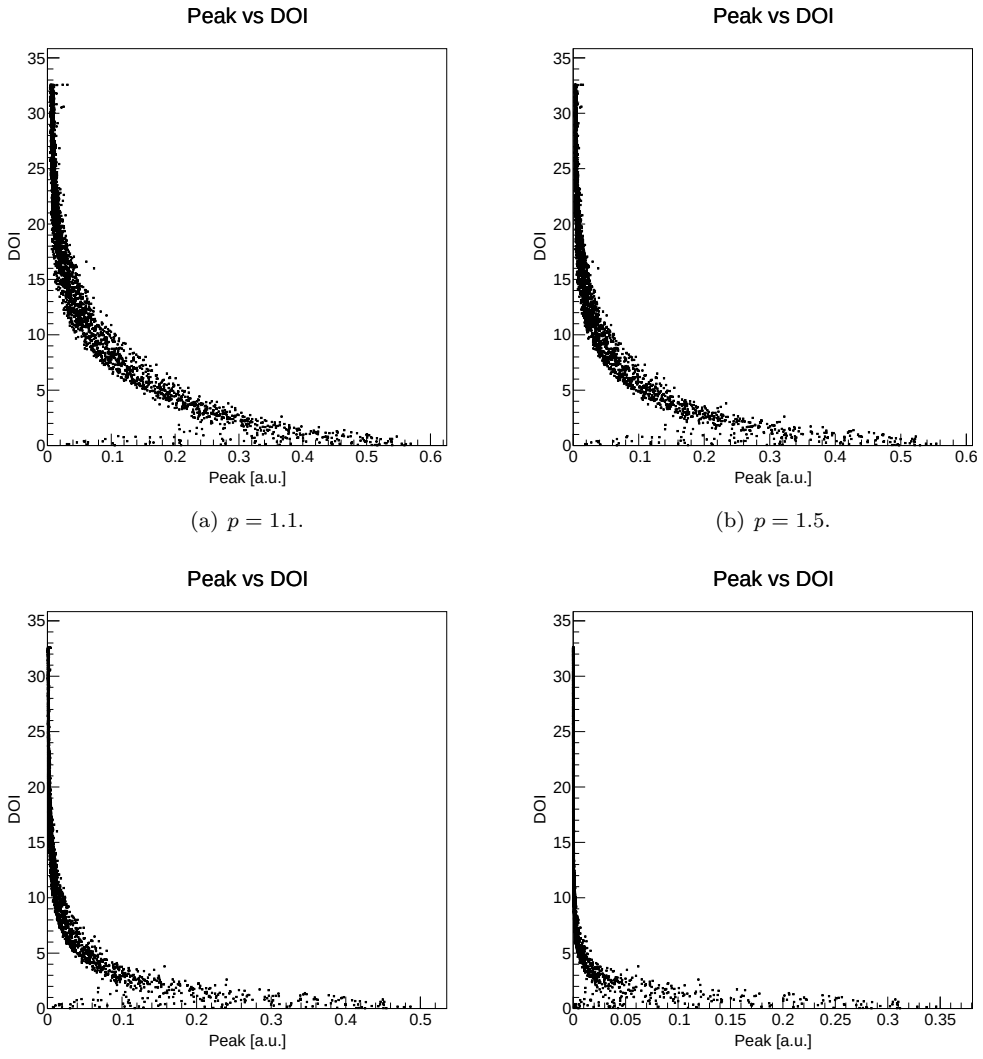

(a) $p = 1.1$.

(b) $p = 1.5$.

(c) $p = 2.0$.

(d) $p = 3.0$.

Figure 33: The plots show the correlation between relative peak and DOI for various values of p in Equation (25).

As one can see, there is very good correlation between the relative peak value and the DOI, especially for powers close to but slightly larger than 1 (for $p = 1$ the peak value is equal to the total count and P_{rel} always evaluates to 1). This justifies using the peak value as a figure of merit when reconstructing the DOI. However, likely due to the way the relative peak value is used in the reconstruction algorithm in section 5.10—the DOI is calculated as a COG between the positions of opposite DPC tiles with P_{rel} as weighting factor instead of inferring a DOI directly—the best results have so far been achieved with $p = 2$.

The COG approach for DOI reconstruction was chosen because the result will always be inside the crystal even for extreme outliers. Furthermore, the data shown in this section is not easily available via experimental methods because the exact DOI is not known in experiments whereas the COG method can be applied directly to the data produced by DPCs in real acquisition.
Some data points show very low peak values at very small DOIs. These outliers correspond to events with very low scintillation yields or events were the POI is very close to the DPC at the border between two pixels and many photons get lost in the gap between them.

5.10 POI Reconstruction

The analytical reconstruction devised in this work relies only on the COG, the peak value P and the relative peak value P_{rel}. All three can be calculated from PCAs (photon count array) alone.
For convention, x and y will be the coordinates in the respective DPC tiles plane and z the coordinate normal to it (i.e. the DOI). First, for each DPC tile the two coordinates in the tiles plane are calculated by

$$x_{\mathrm{COG}} = \mathrm{COG}(p_{\mathrm{xy}}, \vec{c}, \vec{x}) \tag{78}$$
$$y_{\mathrm{COG}} = \mathrm{COG}(p_{\mathrm{xy}}, \vec{c}, \vec{y}) \tag{79}$$

with the COG function defined as in Equation (10). The vectors $\vec{x}$, $\vec{y}$ and $\vec{c}$ have dimension 64 and contain the coordinates and photon counts of a given photon count array (as seen in Figure 32), $p_{\mathrm{xy}} > 1$ is a power to which the weights of the COG are raised.
In a 6-sided readout configuration there are three pairs of DPCs facing each other (for 4-sided readout there are two and for 2-sided readout one). The DOI was estimated using the positions of opposite DPC tiles and weighting these positions with their corresponding relative peak values which can be done using the COG function again

$$z_{\mathrm{COG}} = \mathrm{COG}(p_z, \vec{P}_{\mathrm{rel}}(p_{\mathrm{DOI}}), \vec{z}) \tag{80}$$

where p_z is the weighting power similar to p_{xy}, $\vec{z}$ a vector of dimension 2 with the positions of two opposite DPC tiles (always $\pm 16.3\,\mathrm{mm}$ along all 3 axes) and $\vec{P}_{\mathrm{rel}}(p_{\mathrm{DOI}})$ a vector of dimension 2 containing the relative peak values as defined in Equation (25) for both DPCs, respectively. The DOIs of two opposite DPCs will always add up to 32.6 mm.
In this way, a set of 6 POI estimates can be acquired for each event using 6-sided readout, although the DOIs acquired from opposite DPCs are redundant. After rotating all 6 estimates into the same coordinate system, a weighted mean is applied once more using the COG function a third time where the weights are the corresponding relative peak values $P_{\mathrm{rel}}(p_{\mathrm{est}})$ which are themselves raised to a power p_{POI}:

$$x_{\mathrm{est}} = \mathrm{COG}(p_{\mathrm{est}}, \vec{x}_{\mathrm{POI}}, \vec{P}_{\mathrm{rel}}(p_{\mathrm{POI}})) \tag{81}$$
$$y_{\mathrm{est}} = \mathrm{COG}(p_{\mathrm{est}}, \vec{y}_{\mathrm{POI}}, \vec{P}_{\mathrm{rel}}(p_{\mathrm{POI}})) \tag{82}$$
$$z_{\mathrm{est}} = \mathrm{COG}(p_{\mathrm{est}}, \vec{z}_{\mathrm{POI}}, \vec{P}_{\mathrm{rel}}(p_{\mathrm{POI}})). \tag{83}$$

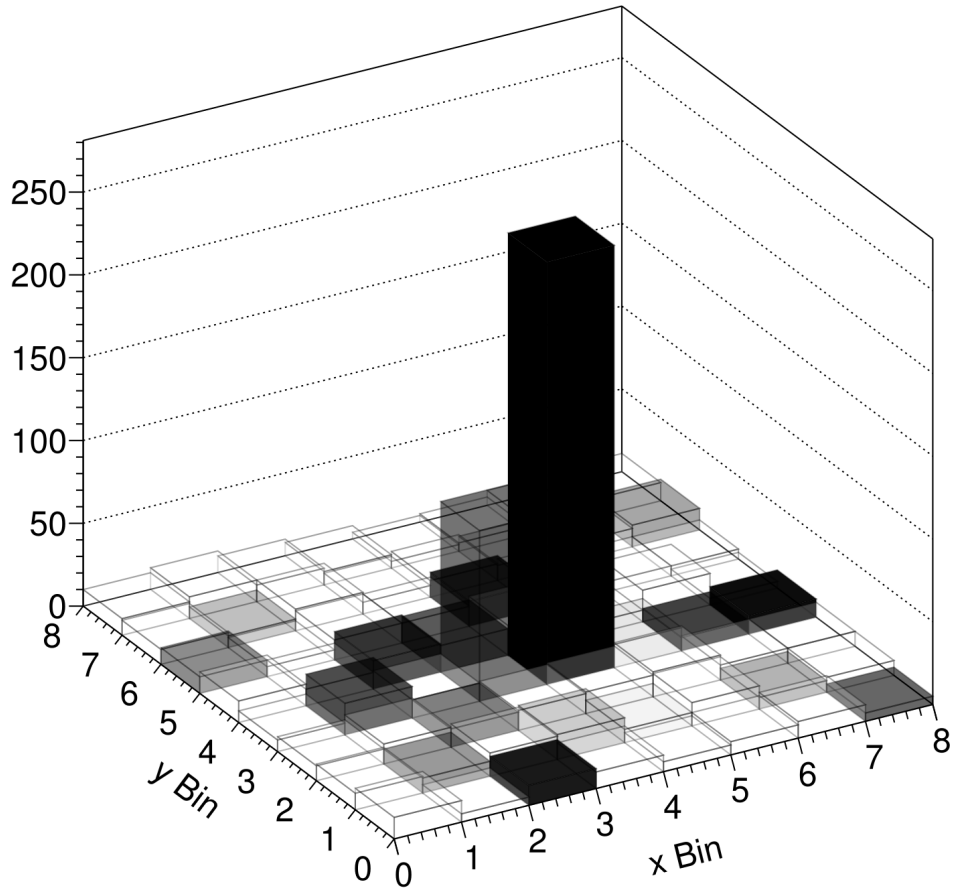

Figure 34: Although the PCA is very sharply peaked, the counts are much lower compared to normal events with similar peaks (see Figure 32(a)). Such outliers occur if a POI is located close to a gap between pixels where many optical photons are lost.

In total, 5 parameters have to be chosen: p_{xy}, p_z, p_{DOI}, p_{est} and p_{POI}.
A sixth parameter, the peak threshold $t_{\mathrm{P}} \in [0, 1]$ is introduced to filter events with PCAs which yield high peak values despite very low photon counts, an example can be seen in Figure 34. These events occur if the POI is very close to the DPC tile and between two pixels or dies. In this case, a lot of photons will vanish in the gap between them and consequently the photon count and the peak (i.e. highest photon count in the array) will be low.

In order to filter these events, the total count C_{tot} (Equation (16)) for each tile is calculated. Then, a mean total count is calculated by

$$\overline{C} = \frac{\sum_{i=1}^{N-1} C_{\mathrm{tot},i}}{N-1}, \quad C_{\mathrm{tot},i} \geq C_{\mathrm{tot,min}} \tag{84}$$

where N is the number of DPCs used in the detector system. The mean is then compared to the lowest total count $C_{\mathrm{tot,min}}$ using t_P. If

$$C_{\mathrm{tot,min}} > t_P \, \overline{C} \tag{85}$$

is true, then the event is accepted, otherwise it is discarded. This approach is based on the assumption, that the DPC tile where many photons are lost in a gap between pixels has a lower total photon count than other DPCs in the detector system.

5.11 POI Reconstruction Calibration with variable QEs and Results

The reconstruction algorithm was applied to data sets of single and multiple interaction events with pixel and sub-pixel resolution and a 2-, 4- and 6-sided readout configuration.
The POI reconstruction method described in the previous chapter relies on 6 parameters which have to be calibrated. In order to find the best set of parameters, a rough scan has been performed with the limits and step sizes shown in Table 6. Each set of parameters was applied to 100 random single interaction events out of the corresponding full data set. Then the mean error of these 100 samples was calculated and the sets achieving the best results for each quantum efficiency (QE) were then tested against the full data set. The size of the various data sets can be seen in Table 7. The parameter sets with the best performance can be seen in Tables 8, 9 and 10.

Parameter	**Min**	**Max**	**Step**
QE	0.5	0.9	0.1
p_{xy}	1	4	1
p_z	1	4	1
p_{est}	1	4	1
p_{DOI}	2	4	1
p_{POI}	2	4	1
t_P	0.2	0.2	0.0

Table 6: These ranges and step sizes were used for the reconstruction parameter scan.

Readout Configuration	**Event Type**	**Number of Events**
6-sided	single Interaction	10000
	multiple Interactions	10000
4-sided	single Interaction	8000
2-sided	single Interaction	8000

Table 7: Given above are the numbers of simulated events for various configurations of the detector system.

Best Parameter Sets found for 2-sided readout						
QE	p_{xy}	p_z	p_{est}	p_{DOI}	p_{POI}	t_P
0.5	4	1	3	3	4	0.2
0.6	4	1	4	3	3	0.2
0.7	4	1	2	3	4	0.2
0.8	4	1	2	3	3	0.2
0.9	4	1	4	3	2	0.2

Table 8: Given above are the best parameter sets found for 2-sided readout.

Best Parameter Sets found for 4-sided readout						
QE	p_{xy}	p_z	p_{est}	p_{DOI}	p_{POI}	t_P
0.5	2	2	1	2	2	0.2
0.6	2	2	1	2	3	0.2
0.7	4	2	1	2	2	0.2
0.8	4	2	1	2	3	0.2
0.9	3	2	2	2	2	0.2

Table 9: Given above are the best parameter sets found for 4-sided readout.

Best Parameter Sets found for 6-sided readout						
QE	p_{xy}	p_z	p_{est}	p_{DOI}	p_{POI}	t_P
0.5	2	1	1	3	2	0.2
0.6	2	1	2	2	4	0.2
0.7	2	1	1	3	2	0.2
0.8	2	1	3	2	2	0.2
0.9	4	1	3	2	2	0.2

Table 10: Given above are the best parameter sets found for 6-sided readout.

From each reconstructed event, an error vector was calculated as

$$\vec{r}_{\text{error}} = \vec{r}_{\text{reco}} - \vec{r}_{\text{true}} \tag{86}$$

where $\vec{r}_{\text{reco}}$ is the reconstructed POI and $\vec{r}_{\text{actual}}$ is the true POI. The coordinates of the error vector were then entered into histograms for each coordinate axis.

The parameter sets for 2- and 4-sided readout were tested only for single interaction events (sketches for these configurations are shown in Figure 35). For both configurations, the error histograms differ strongly for individual axes based on what information was available for reconstruction.
In Figure 36 the error histograms for 2-sided readout, a QE of 0.7 and single interaction events are shown. While x- and y-coordinates had to be reconstructed from the COG in the DPCs planes alone, the z-coordinate had to be reconstructed from the COG between DPCs using the relative peak value as weight. X- and y-coordinates achieve a better FWHM but the z-coordinate has a better FWTM. This shows, that the COG method in the DPC plane may reach very good precision in certain cases but its performance varies greatly—presumably for larger DOIs where the background increases—which causes wider slopes in the corresponding error distributions. On the other hand, the z-axis shows a plateau for small errors—which indicates a lower limit for precision—but the DOI reconstruction using the peak value performs equally well for most events—and thus most positions in the scintillator—which causes the distribution to have very steep slopes. Consequently, in Table 11 all FWHM values correspond to the z-coordinate while all FWTM values correspond to either the x- or y-coordinate. Interestingly, the FWHM does not improve with larger QE values which shows, that the relative peak value is mostly dependent on the distribution of photon counts and not their absolute values in a PCA.

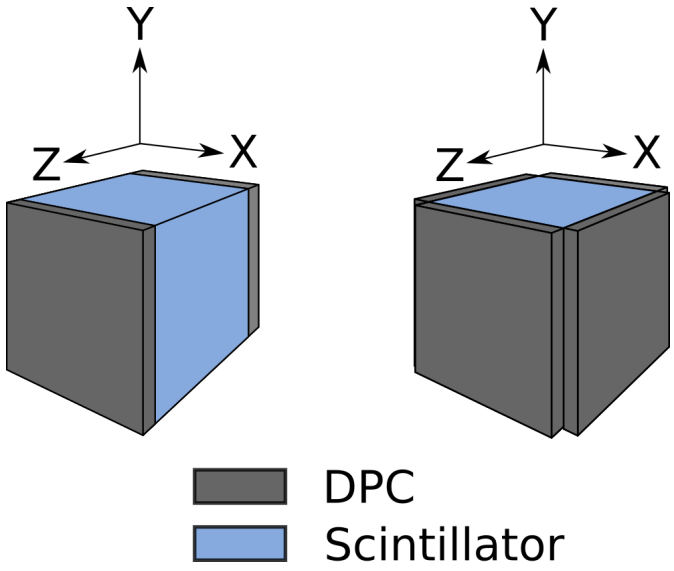

Figure 35: Shown are sketches for the 2-sided (left) and 4-sided (right) readout configuration of the detector system.

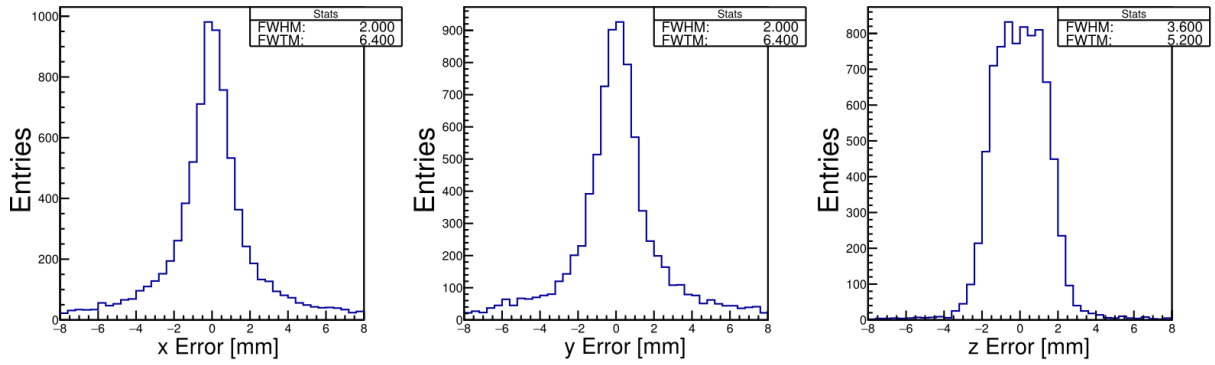

Figure 36: Shown are the reconstruction error histograms for a 2-sided readout configuration and single interaction events at a QE of 0.7*. For a discussion of these Figures please refer to the text.*

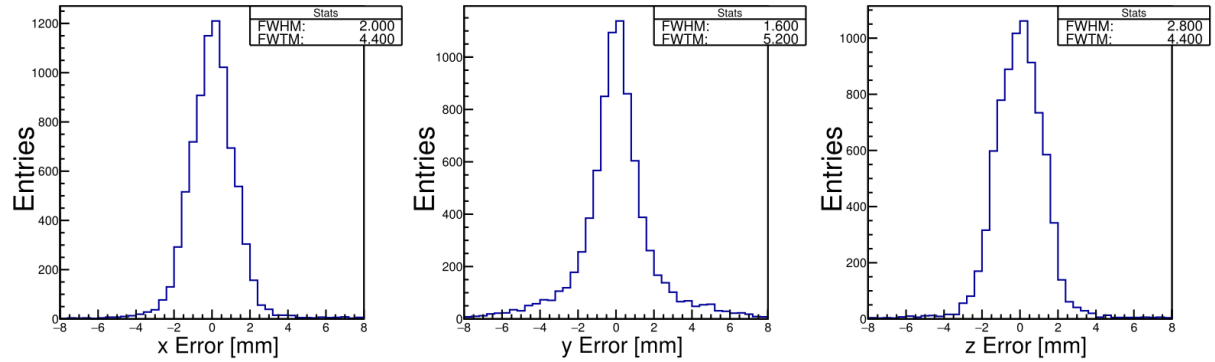

Figure 37: Shown are the reconstruction error histograms for a 4-sided readout configuration and single interaction events at a QE of 0.7*. For a discussion of these Figures please refer to the text.*

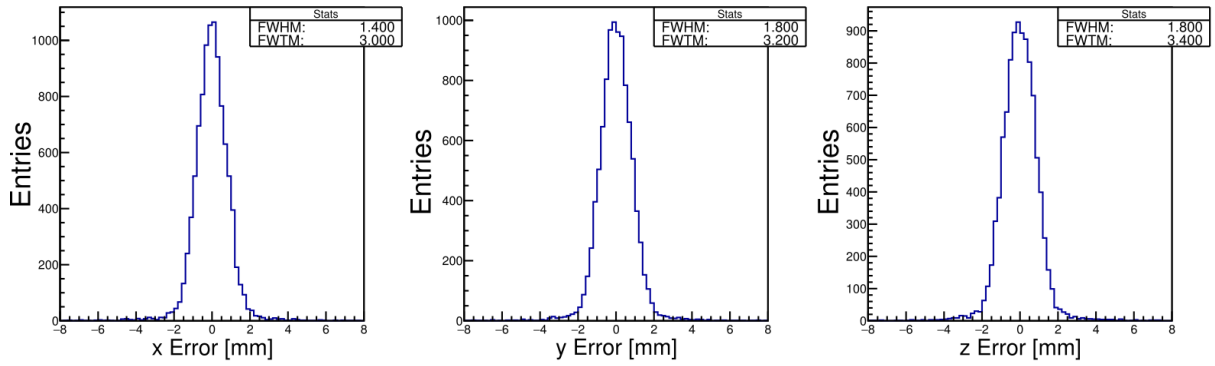

Figure 38: Shown are the reconstruction error histograms for a 6-sided readout configuration and single interaction events at a QE of 0.7*. For a discussion of these Figures please refer to the text.*

In Figure 37 the error histograms for a 4-sided readout configuration, a QE of 0.7 and single interaction events is shown. For x- and z-coordinates the COG in the DPC plane as well as the COG between DPCs can be calculated. For the y-coordinate only the COG in the DPC plane is available. Similar to a 2-sided readout, while the FWHM is better along the y-axis, the FWTM is better for the x- and z-axis. However, the fluctuating results shown in Table 11 indicate, that the parameter sets are not well optimized.
In Figure 38 the error histograms are shown for a 6-sided readout configuration and single interaction events with a QE of 0.7. The FWHM reaches 1.4 to 1.8 mm. The fluctuations are likely due to the large bin size which had to be chosen based on the size of the data sets. However, there is an overall tendency that errors for the x-axis are smallest and errors for the z-axis largest for a 6-sided readout configuration. The only asymmetry in this configuration is caused by the positioning of dies on a DPC tile (see Figure 14) where they have large gaps between them along one direction but only very small gaps along the other which is likely the cause for slightly different errors along individual axes. The plateaus which seem to occur for very small errors along the y- and z-axis may be due to the possibility, that the true best parameter set for this particular detector configuration has not yet been found and the algorithm is not performing optimally. Although, as shown for 2-sided and 4-sided readout configurations, another possibility is that the COG between DPCs has a lower limit for its error due to the behaviour of the peak value or sub-optimal parameter sets. The parameter set for 6-sided readout was also tested for multiple interaction events and with pixel as well as sub-pixel resolution. A summary of the results can be seen in Table 12
Overall, the resolution definitely improves for sub-pixel readout. Interestingly, sub-pixel readout seems to greatly improve FWTM values for multiple interaction events.

	Single Interactions for 2-sided Readout	**Single Interactions for 4-sided Readout**
QE	FWHM [mm] ‖ FWTM [mm]	FWHM [mm] ‖ FWTM [mm]
0.5	3.6 ‖ 9.2	2.0 ‖ 8.0
0.6	3.6 ‖ 8.0	2.0 ‖ 6.4
0.7	3.6 ‖ 6.4	2.8 ‖ 5.2
0.8	3.6 ‖ 5.6	3.6 ‖ 4.8
0.9	3.6 ‖ 5.2	1.6 ‖ 5.2

Table 11: Shown are results for the FWHM and FWTM for 2-sided and 4-sided readout of single interaction events calculated with the parameter sets given in Tables 8 and 9, respectively. For each QE only the largest value for the FWHM and FWTM across all 3 axes is given. For details please refer to the text.

	Single Interactions at Pixel Resolution	**Multiple Interactions at Pixel Resolution**
QE	FWHM [mm] ‖ FWTM [mm]	FWHM [mm] ‖ FWTM [mm]
0.5	1.8 ‖ 3.4	2.0 ‖ 7.2
0.6	1.4 ‖ 3.0	2.0 ‖ 7.6
0.7	1.8 ‖ 3.4	2.0 ‖ 6.4
0.8	1.0 ‖ 2.6	2.0 ‖ 7.6
0.9	1.2 ‖ 3.0	2.0 ‖ 7.6
	Single Interactions at Sub-Pixel Resolution	**Multiple Interactions at Sub-Pixel Resolution**
QE	FWHM [mm] ‖ FWTM [mm]	FWHM [mm] ‖ FWTM [mm]
0.5	1.0 ‖ 2.2	1.0 ‖ 3.0
0.6	1.0 ‖ 3.0	1.4 ‖ 4.0
0.7	0.6 ‖ 1.8	1.0 ‖ 2.2
0.8	1.0 ‖ 2.4	1.0 ‖ 3.4
0.9	1.0 ‖ 2.4	1.4 ‖ 3.4

Table 12: Shown are results for the FWHM and FWTM for 6-sided readout of single and multiple interaction events with pixel and sub-pixel resolution calculated with the parameter sets given in Table 10. For each QE only the largest value for the FWHM and FWTM across all 3 axes is given. For details please refer to the text.

In summary, the results in Tables 11 and 12 show:

- more DPCs improve the performance of the reconstruction algorithm significantly.
- Using sub-pixel resolution improves the performance of the reconstruction algorithm, especially for multiple interaction events.
- There is an overall decrease in performance for multiple interactions.
- COGs calculated in the DPC plane are capable of higher precision but have a broader distribution of errors.
- COGs calculated between DCPs using the peak factor seemingly have a lower limit for precision but have a narrower error distribution overall.

The fluctuations of the mean errors indicate, that the true best parameter sets have not yet been found. This is likely due to the fact, that the initial scan tested parameter sets only against 100 events which means that non-negligible fluctuations of the resulting mean are still likely. Also, only integer values were scanned for most parameters. A scan with smaller step sizes might yield better results.

6 Conclusion and Outlook

Although the performance of the application cannot be determined without comparing it to experimental data, the output was investigated for consistency and seems plausible based on the mean free path of gammas in the scintillator, their energy deposit spectrum and the electron ranges for various energies in the scintillator.

The statistical analysis of the behaviour of optical photons in the scintillator shows, that even for a 6-sided readout configuration more than half of the photons are reflected at least once which is likely limiting the performance of analytic reconstruction algorithms. For 2- and 4-sided readout configurations, this issue is exacerbated. Furthermore, roughly a quarter of optical photons is either re-absorbed by the scintillator or lost in gaps between pixels. Overall, a bit more than half of scintillation photons and a bit less than half of Cherenkov photons produced during an event with full energy deposit are detected by the DPCs with a QE of 1.0.

The influence of Cherenkov photons on timing was shown to be minimal due to the fact that in a 6-sided readout, the number of dies—and thus the number of time stamps—is much larger than the mean number of detected Cherenkov photons. Furthermore, the influence of Cherenkov photons decreases rapidly beyond the first few detected photons.

The results achieved with the reconstruction algorithm allow several conclusions:

While the COG in the DPC plane can provide precise results for some events it quickly loses performance for larger DOIs which worsens performance overall. On the other hand, the COG between opposite DPC tiles with the peak value used as weight, performs very stably for most DOIs although in some cases there seems to be a minimum error which cannot be undercut. Consequently, FWHM values are improved by the COG in the DPC plane while FWTM values are improved by the COG between DPCs. Further improvements on how both COGs can be combined to achieve optimum results must be investigated.

When comparing 2-, 4- and 6-sided readout performance, a definite improvement for configurations with more DPCs can be observed. Specifically, 2- and 4-sided readout are not equally precise along all spatial axes which diminishes their performance whereas a 6-sided readout only shows slight fluctuations in precision caused by the asymmetric positioning of dies on the DPCs.

When comparing pixel and sub-pixel resolution, a definite improvement in POI reconstruction can be observed. Consequently, a DPC model capable of producing photon counts at sub-pixel resolution might perform better although such a model will most likely have a lower fill factor and thus a lower PDE.

The next steps for the application developed in this work will be to improve the stability and speed of the code and provide more options to limit the output so that larger data sets can be generated, i.e., to improve statistics for the analysis of reconstruction algorithms. Furthermore, common phenomena in DPCs and SiPMs in general must be implemented, such as a dark count rate and cross talk. The various available physics lists must be tested and optimized once experimental data is available and other scintillation materials must be implemented and compared.

Finally, it can be concluded that the simulated detector design with 6-sided readout promises to achieve—or at least come close to—the goals set for the PALADIN project. The simulation of the mean free path of gammas in the scintillator indicates, that a detection efficiency of 90% is possible, an energy resolution of less than 10% will have to be confirmed experimentally, however it has already been achieved by other research groups using LYSO:Ce:Ca. The results for spatial reconstruction seem promising although– again–experiments will be necessary. The same may be expected for timing resolution which greatly depends on spatial reconstruction.

7 References

[1] D. Renker, "Geiger-mode avalanche photodiodes, history, properties and problems," *Nuclear Instruments & Methods in Physics Research, Section A: Accelerators, Spectrometers, Detectors, and Associated Equipment*, 2006.

[2] P. Buzhan, B. Dolgoshein, A. Ilyin, V. Kantserov, V. Kaplin, A. Karakash, A. Pleshko, E. Popova, S. Smirnov, Y. Volkov, *et al.*, "An advanced study of silicon photomultiplier," *ICFA Inst. Bull*, vol. 21, p. 28, 2001.

[3] T. Frach, G. Prescher, C. Degenhardt, R. de Gruyter, A. Schmitz, and R. Ballizany, "The digital silicon photomultiplier - principle of operation and intrinsic detector performance," *IEEE*, 2009.

[4] "Paladin project." http://fasttiming.weebly.com/.

[5] "Paladin - "positron annihilation detection beyond the limits"." MSCA-IF-2014-EF - Marie Skodowska-Curie Individual Fellowships (IF-EF). http://cordis.europa.eu/project/rcn/195770_en.html.

[6] S. Seifert, G. van der Lei, H. T. van Dam, and D. R. Schaart, "First characterization of a digital sipm based time-of-flight pet detector with 1mm spatial resolution," *Physics in Medicine and Biology*, vol. 58, no. 9, p. 3061, 2013.

[7] S. Brunner, L. Gruber, J. Marton, H. Orth, and K. Suzuki, "Time resolution below 100ps for the scitil detector of panda employing sipm," 2014. arXiv: 1312.4153.

[8] I. Antcheva, M. Ballintijn, B. Bellenot, M. Biskup, R. Brun, N. Buncic, P. Canal, D. Casadei, O. Couet, V. Fine, L. Franco, G. Ganis, A. Gheata, D. G. Maline, M. Goto, J. Iwaszkiewicz, A. Kreshuk, D. M. Segura, R. Maunder, L. Moneta, A. Naumann, E. Offermann, V. Onuchin, S. Panacek, F. Rademakers, P. Russo, and M. Tadel, "ROOT A C++ framework for petabyte data storage, statistical analysis and visualization," *Computer Physics Communications*, vol. 180, no. 12, pp. 2499 – 2512, 2009.

[9] S. Cova, M. Ghioni, A. Lotito, I. Rech, and F. Zappa, "Evolution and prospects for single-photon avalanche diodes and quenching circuits," *Journal of Modern Optics*, vol. 51, pp. 1267–1288, June 2004.

[10] Philips, "Philips digital photon counting, tile-tek user manual," 2016. www.digitalphotoncounting.com.

[11] Z. Liu, M. Pizzichemi, E. Auffray, P. Lecoq, and M. Paganoni, "Performance study of philips digital silicon photomultiplier coupled to scintillating crystals," *IOPscience*, 2016.

[12] G. Borghi, V. Tabacchini, and D. R. Schaart, "Towards monolithic scintillator based tof-pet ssystem: practical methods for detector calibration and operation," *IOPscience*, vol. Phys. Med. Biol. 61, 2016.

[13] H. T. van Dam, S. Seifert, R. Vinke, P. Dendooven, H. Löhner, F. J. Beckman, and D. R. Schaart, "Improved nearest neighbor methods for gamma photon interaction position determination in monolithic scintillatior pet detectors," *IEEE Transactions of Nuclear Science*, vol. 58, October 2011.

[14] S. Agostinelli, J. Allison, K. Amako, J. Apostolakis, H. Araujo, P. Arce, M. Asai, D. Axen, S. Banerjee, G. Barrand, F. Behner, L. Bellagamba, J. Boudreau, L. Broglia, A. Brunengo, H. Burkhardt, S. Chauvie, J. Chuma, R. Chytracek, G. Cooperman, G. Cosmo, P. Degtyarenko, A. Dell'Acqua, G. Depaola, D. Dietrich, R. Enami, A. Feliciello, C. Ferguson, H. Fesefeldt, G. Folger, F. Foppiano, A. Forti,

S. Garelli, S. Giani, R. Giannitrapani, D. Gibin, J. G. Cadenas, I. Gonzlez, G. G. Abril, G. Greeniaus, W. Greiner, V. Grichine, A. Grossheim, S. Guatelli, P. Gumplinger, R. Hamatsu, K. Hashimoto, H. Hasui, A. Heikkinen, A. Howard, V. Ivanchenko, A. Johnson, F. Jones, J. Kallenbach, N. Kanaya, M. Kawabata, Y. Kawabata, M. Kawaguti, S. Kelner, P. Kent, A. Kimura, T. Kodama, R. Kokoulin, M. Kossov, H. Kurashige, E. Lamanna, T. Lampn, V. Lara, V. Lefebure, F. Lei, M. Liendl, W. Lockman, F. Longo, S. Magni, M. Maire, E. Medernach, K. Minamimoto, P. M. de Freitas, Y. Morita, K. Murakami, M. Nagamatu, R. Nartallo, P. Nieminen, T. Nishimura, K. Ohtsubo, M. Okamura, S. O'Neale, Y. Oohata, K. Paech, J. Perl, A. Pfeiffer, M. Pia, F. Ranjard, A. Rybin, S. Sadilov, E. D. Salvo, G. Santin, T. Sasaki, N. Savvas, Y. Sawada, S. Scherer, S. Sei, V. Sirotenko, D. Smith, N. Starkov, H. Stoecker, J. Sulkimo, M. Takahata, S. Tanaka, E. Tcherniaev, E. S. Tehrani, M. Tropeano, P. Truscott, H. Uno, L. Urban, P. Urban, M. Verderi, A. Walkden, W. Wander, H. Weber, J. Wellisch, T. Wenaus, D. Williams, D. Wright, T. Yamada, H. Yoshida, and D. Zschiesche, "Geant4a simulation toolkit," *Nuclear Instruments and Methods in Physics Research Section A: Accelerators, Spectrometers, Detectors and Associated Equipment*, vol. 506, no. 3, pp. 250 – 303, 2003.

[15] J. Allison, K. Amako, J. Apostolakis, H. Araujo, P. A. Dubois, M. Asai, G. Barrand, R. Capra, S. Chauvie, R. Chytracek, G. A. P. Cirrone, G. Cooperman, G. Cosmo, G. Cuttone, G. G. Daquino, M. Donszelmann, M. Dressel, G. Folger, F. Foppiano, J. Generowicz, V. Grichine, S. Guatelli, P. Gumplinger, A. Heikkinen, I. Hrivnacova, A. Howard, S. Incerti, V. Ivanchenko, T. Johnson, F. Jones, T. Koi, R. Kokoulin, M. Kossov, H. Kurashige, V. Lara, S. Larsson, F. Lei, O. Link, F. Longo, M. Maire, A. Mantero, B. Mascialino, I. McLaren, P. M. Lorenzo, K. Minamimoto, K. Murakami, P. Nieminen, L. Pandola, S. Parlati, L. Peralta, J. Perl, A. Pfeiffer, M. G. Pia, A. Ribon, P. Rodrigues, G. Russo, S. Sadilov, G. Santin, T. Sasaki, D. Smith, N. Starkov, S. Tanaka, E. Tcherniaev, B. Tome, A. Trindade, P. Truscott, L. Urban, M. Verderi, A. Walkden, J. P. Wellisch, D. C. Williams, D. Wright, and H. Yoshida, "Geant4 developments and applications," *IEEE Transactions on Nuclear Science*, vol. 53, pp. 270–278, Feb 2006.

[16] G. Cowan, *Statistical Data Analysis*. Oxford University Press, 1998. ISBN 0 19 850156 0.

[17] D. M. Geant4, *Physics Reference Manual*. Geant4, 2015. URL: http://geant4.web.cern.ch/geant4/G4UsersDocuments/UsersGuides/ PhysicsReferenceManual/html/-PhysicsReferenceManual.html.

[18] W. R. Leo, *Techniques for Nuclear and Particle Physics Experiments*. Springer-Verlag Berlin Heidelberg GMBH, 2nd edition ed., 1993.

[19] J. Apostolakis, S. Giani, M. Maire, P. Nieminen, M. Pia, and L. Urban, "Geant4 low energy electromagnetic models for electrons and photons," *CERN-OPEN*, vol. 99-034, 1999.

[20] F. Salvat, J. Fernandez-Varea, E. Acosta, and J. Sempau, "Penelope, a code system for monte carlo simulation of electron and photon transport," *OECD/NEA*, vol. 5-7, 2001. ISBN: 92-64-18475-9.

[21] R. Ribberfors, "Relationship of the relativistic compton cross section to the momentum distribution of bound electron states. ii. effects of anisotropy and polarization," *Phys. Rev. B*, vol. 12, pp. 3136–3141, 1975.

[22] M. J. Berger, J. H. Hubbell, S. M. Seltzer, J. Chang, J. S. Coursey, R. Sukumar, D. S. Zucker, and K. Olsen, "Xcom: Photon cross section datadata," no. Verison 1.5, 2010. http://physics.nist.gov/xcom.

[23] T. Williams, C. Kelley, and many others, "Gnuplot 4.4: an interactive plotting program," March 2010. http://gnuplot.sourceforge.net/.

[24] D. Cullen, "A simple model of photon transport," *Nuclear Instruments & Methods in Physics Research, Section B: Accelerators, Spectrometers, Detectors, and Associated Equipment*, vol. 101, pp. 499–510, 1995.

[25] U. D. Wikimedia Commons, "Klein-nishina polar plot." released into public domain. https://commons.wikimedia.org/wiki/File:Klein-Nishina_distribution.png.

[26] G. F. Knoll, *Radiation Detection and Measurement*. Wiley, 4th ed., 2010.

[27] NEMA - National Electrical Manufacturers Association, "Industrial laminating thermosetting products," *NEMA Standards Publication*, no. LI 1-1998.

[28] D. J. van der Laan, D. R. Schaart, M. C. Maas, F. J. Beekman, P. Bruyndonckx, and C. W. E. van Eijk, "Optical simulation of monolithic scintillator detectors using gate/geant4," *IOPscience, Phys. Med. Biol.*, vol. 55, pp. 1659–1675, 2010.

[29] R. Mao, L. Zhang, and R.-Y. Zhu, "Optical and scintillation properties of inorganic scintillators in high energy physics," *IEEE*, 2007.

[30] D. N. ter Weele, D. R. Schaart, and P. Dorenbos, "Comparative study of co-doped and non co-doped lso:ce and lyso:ce scintillators for tof-pet," *IEEE Transactions of Nuclear Science*, vol. 62, no. 3, 2015.

[31] J. T. M. de Haas and P. Dorenbos, "Advances in yield calibration of scintillators," *IEEE Transactions of Nuclear Science*, vol. 55, no. 3, 2008.

[32] "Nist estar." URL: http://physics.nist.gov/PhysRefData/Star/Text/ESTAR.html.

[33] "Nist elements database." http://physics.nist.gov/PhysRefData/Elements/index.html.

[34] *DELO-PHOTOBOND 4436 - Technische Information*. https://www.delo.de/fileadmin/datasheet/DELO-PHOTOBOND_4436_(TIDB-D).pdf.

[35] "Refractive index database," http://refractiveindex.info/.

8 Appendix

8.1 Material Properties

Element	Atomic Weight	Atomic Number
Hydrogen, H	1.01	1
Carbon, C	12.01	6
Oxygen, O	16.00	8
Silicium, Si	28.09	14
Calcium, Ca	40.078	20
Yttrium, Yt	88.91	39
Cer, Ce	140.12	58
Lutetium, Lu	174.97	71

Table 13: Given above is a list of the elements defined in the application. They are used to build various materials. The data was acquired from the NIST database for elements [33]. Only Elements which were specifically needed to build certain materials were defined explicitly. Others were introduced as materials from the GEANT4 NIST Material Database.

Material	Molecular Formula or Components in %	Density $[g/cm^3]$	Source
Vacuum	unknown	10^{-25}	GEANT4 NIST Material Database
Air	C: 0.0124 N: 75.5267 O: 23.1781 Ar: 1.2827	$1.2\,10^{-3}$	GEANT4 NIST Material Database
Silicon Dioxide (Glass)	SiO_2	2.32	GEANT4 NIST Material Database
Silver	Ag	10.5	GEANT4 NIST Material Database
Silicon	Si	2.33	GEANT4 NIST Material Database
Acrylic (base ingredient for glue from DPC)	$C_5O_2H_8$	1.0	DELO Photobond 4436 data sheet [34]
Epoxy (base ingredient for circuit board)	$C_1O_1H_1$	1.0	[28]
FR4 (circuit board)	SiO_2: 52.8 Epoxy: 47.2	1.86	[27]
LYSO (base material for scintillator)	Lu: 71 | Si: 7 O: 18 | Y: 4	7.4	[29]
LYSO:Ce:Ca	LYSO: 99.6 Ce: 0.2 Ca: 0.2	7.4	[30]

Table 14: Given above are details on the materials used in the application. Detailed data of the refractive index, absorption and emission spectrum and reflectivity of materials can be found in Table 15

Material	Energy Bins [eV]	Refractive Index Bins (dielectrica only)	Reflectivity Bins [a.u] (metals only)	Efficiency Bins [a.u.] (metals only)	Source
Glass	1.000, 1.968, 2.084, 2.214, 2.362, 2.530, 2.725, 2.952, 3.220, 3.542, 3.936, 4.428, 5.000	1.467, 1.457, 1.458, 1.459, 1.461, 1.463, 1.465, 1.468, 1.472, 1.477, 1.484, 1.494 1.504			[35]
Silicon	1.000, 2.000, 2.032, 2.066, 2.101, 2.138, 2.175, 2.214, 2.254, 2.296, 2.339, 2.384, 2.431, 2.480, 2.530, 2.583, 2.638, 2.695, 2.755, 2.818, 2.883, 2.952, 3.024, 3.100, 3.179, 3.263, 3.351, 3.444, 5.000		0.291, 0.350, 0.352, 0.354, 0.356, 0.359, 0.361, 0.364, 0.367, 0.370, 0.374, 0.378, 0.382, 0.387, 0.392, 0.398, 0.404, 0.411, 0.420, 0.429, 0.439, 0.452, 0.467, 0.486, 0.511, 0.547, 0.584, 0.583, 0.673	1.0	[35]
LYSO:Ce	1.000, 2.084, 2.101, 2.119, 2.138, 2.156, 2.175, 2.194, 2.214, 2.234, 2.254, 2.275, 2.296, 2.317, 2.339, 2.362, 2.384, 2.407, 2.431, 2.455, 2.480, 2.505, 2.530, 2.556, 2.583, 2.610, 2.638, 2.666, 2.695, 2.725, 2.755, 2.786, 2.818, 2.850, 2.883, 2.917, 2.952, 2.987, 3.024, 3.061, 3.100, 3.139, 3.179, 3.220, 3.263, 3.306, 3.351, 3.397, 5.000	1.781, 1.806, 1.806, 1.806, 1.806, 1.806, 1.806, 1.806, 1.806, 1.806, 1.806, 1.810, 1.810, 1.810, 1.810, 1.810, 1.810, 1.813, 1.813, 1.813, 1.813, 1.813, 1.813, 1.818, 1.818, 1.818, 1.818, 1.818, 1.822, 1.822, 1.822, 1.822, 1.822, 1.827, 1.827, 1.827, 1.833, 1.833, 1.833, 1.833, 1.833, 1.833, 1.833, 1.833, 1.833, 1.833, 1.833, 1.886			[29]
Vacuum	any energy	1.0			none
Air	any energy	1.0			[35]
Silver	any energy		1.0	0.0	none
Glue	any energy	1.5			[34]
Epoxy	any energy	1.52			[28]
FR4	not defined	not defined	not defined	not defined	none

Table 15: Given above are the refractive indices for all materials used in the application. The energy range has been extended from $1\,eV$ *to* $5\,eV$ *by linearly extrapolating from the data given by sources. This only affects the first and last entry of all tables. This has been done to widen the spectrum of energies for which GEANT4 calculates the production of optical photons, especially Cherenkov photons. The data for LYSO:Ce will be used in the application although the material in the application is actually LYSO:Ce:Ca because no sources for LYSO:Ce:Ca could be found. If a refractive index is constant for any energy, only its one value is given. Silver has properties which have been chosen to obtain a perfect reflector and not to represent its actual properties. In the application, silver is simply used as a reflective coating for sides of the scintillation cube which are not covered by a DPC when 2-sided or 4-sided readout is simulated to reflect optical photons back into the crystal.*

	Value	Note	Source
Light Yield [1/MeV]	30234	calculated, see Equation (63)	[30], [31]
Fast Time Constant [ns]	7.1 (7%)	Fast Scintillation Component	[30]
Slow Time Constant [ns]	33.3 (93%)	Slow Scintillation Component	[30]
Yield Ratio	0.07	Relative Intensity of Fast Component	[30]
Resolution Scale	4.17	stat. fluctuation of Yield , calculated, see Equation (67)	[30]

	Energy [eV]	Intensity [a.u.]	Source
Photo Emission Spectrum	1.000, 2.084, 2.101, 2.119, 2.138, 2.156, 2.175, 2.194, 2.214, 2.234, 2.254, 2.275, 2.296, 2.317, 2.339, 2.362, 2.384, 2.407, 2.431, 2.455, 2.480, 2.505, 2.530, 2.556, 2.583, 2.610, 2.638, 2.666, 2.695, 2.725, 2.755, 2.786, 2.818, 2.850, 2.883, 2.917, 2.952, 2.987, 3.024, 3.061, 3.100, 3.139, 3.179, 3.220, 3.263, 3.306, 3.351, 3.397, 5.000	0.00000, 0.00000, 0.00000, 0.00165, 0.00167, 0.00152, 0.00333, 0.00610, 0.00521, 0.00764, 0.01006, 0.01117, 0.01334, 0.01770, 0.02013, 0.02365, 0.02671, 0.02977, 0.03344, 0.03832, 0.04502, 0.05436, 0.06485, 0.07878, 0.09467, 0.11725, 0.13932, 0.16499, 0.20140, 0.24168, 0.28924, 0.34628, 0.40069, 0.46068, 0.50702, 0.53453, 0.55480, 0.55851, 0.56448, 0.56878, 0.57236, 0.54510, 0.45280, 0.32717, 0.12754, 0.06665, 0.02053, 0.00344, 0.00000	[28]

	Energy [eV]	Absorption Length[mm]	Source
Absorption Length	1.000, 3.096, 3.099, 3.120, 3.153, 3.180, 3.205, 3.263, 3.351, 3.444, 3.543, 3.647, 3.758, 3.875, 4.001, 4.125, 5.000	5648.80, 198.298, 168.993, 102.055, 44.6810, 22.3200, 11.6800, 4.12900, 3.21400, 3.07000, 2.92600, 2.93700, 2.79300, 2.80300, 2.81300, 2.66900, 2.37300	[28]

Table 16: Given above are additional optical properties of LYSO:Ce and scintillation properties. Again, the data applies to LYSO:Ce but will be used for LYSO:Ce:Ca in the simulation for lack of a source. Again, the energy intervals have been extrapolated to $1\,eV$ *on the low and* $5\,eV$ *on the high side. This is again done by simple linear extrapolation of the actual source data and only applies to the first and last data points of each table.*

8.2 Decision Trees for the Stepping Action and the Event Action

8.2.1 Stepping Action

The decision tree of the stepping action for optical photons can be seen in Figure 39. If a new step belongs to an optical photon, the simulation first checks which readout mode and event filter are set (see Table 2). If the readout mode is "gammastats" all optical photons are discarded and only gamma- and electron-tracks are calculated. Otherwise, depending on the readout mode, various data are gathered. The default readout mode is "spad" where for each photon a full data set is recorded down to the SPAD which was hit. If "sp" is set, the simulation will only record which sub-pixel was hit by a specific photon. If "tile" is set, only the global coordinates of each photon hit will be recorded. Data such as the photon energy or the time stamp are always recorded.
If the readout mode is not "gammastats" the stepping action will proceed to test for various conditions of the step. For example, a SPAD will only be triggered (bottom left column of the tree) if:

- The post-step point of the step is at a border and
- logically inside the sub-pixel volume. Whenever a step is limited by a volume interface, the post-step point is placed exactly on the interface but logically it is treated as if it was inside the volume into which the particle is moving.
- The pre-step point if the step is in the sub-pixel surface layer.
- The track status is "fStopAndKill" which ensures the particle was absorbed at sub-pixel surface.
- The deposited energy is $> 0\,\mathrm{keV}$.

This guarantees, that only photons which deposit energy at the sub-pixel surface and are absorbed trigger a SPAD SD. It has to be noted here, that a SPAD SD cannot be triggered automatically because sensitive detectors only record particles which moved for at least one step inside their volume. Yet, optical photons cannot enter volumes filled with metal and thus cannot trigger a metal-filled sensitive detector such as the SPAD. Consequently the SD has to be triggered "manually".
The decision tree of the stepping action for gammas is shown in Figure 40. If a step belongs to a gamma, the stepping action first checks which event filter is set or if "gammastats" is activated. If "gammastats" or "all Interactions" is set, the event is automatically flagged as "good". If the event filter was set to either "single Interactions" or "multiple Interactions" certain requirements must be fulfilled so that the event is flagged good, otherwise it is aborted. For example, if an event is flagged as "good" while the filter is set to "single Interactions", the following conditions must be met:

- The gamma must be absorbed via the photoelectric effect.
- The track status must be "fStopAndKill".
- The deposited energy must be $511\,\mathrm{keV}$.
- No gamma (primary or secondary) must leave the world volume or be absorbed outside the scintillator.
- All the energy must be deposited with one interaction (immediate photoelectric absorption).

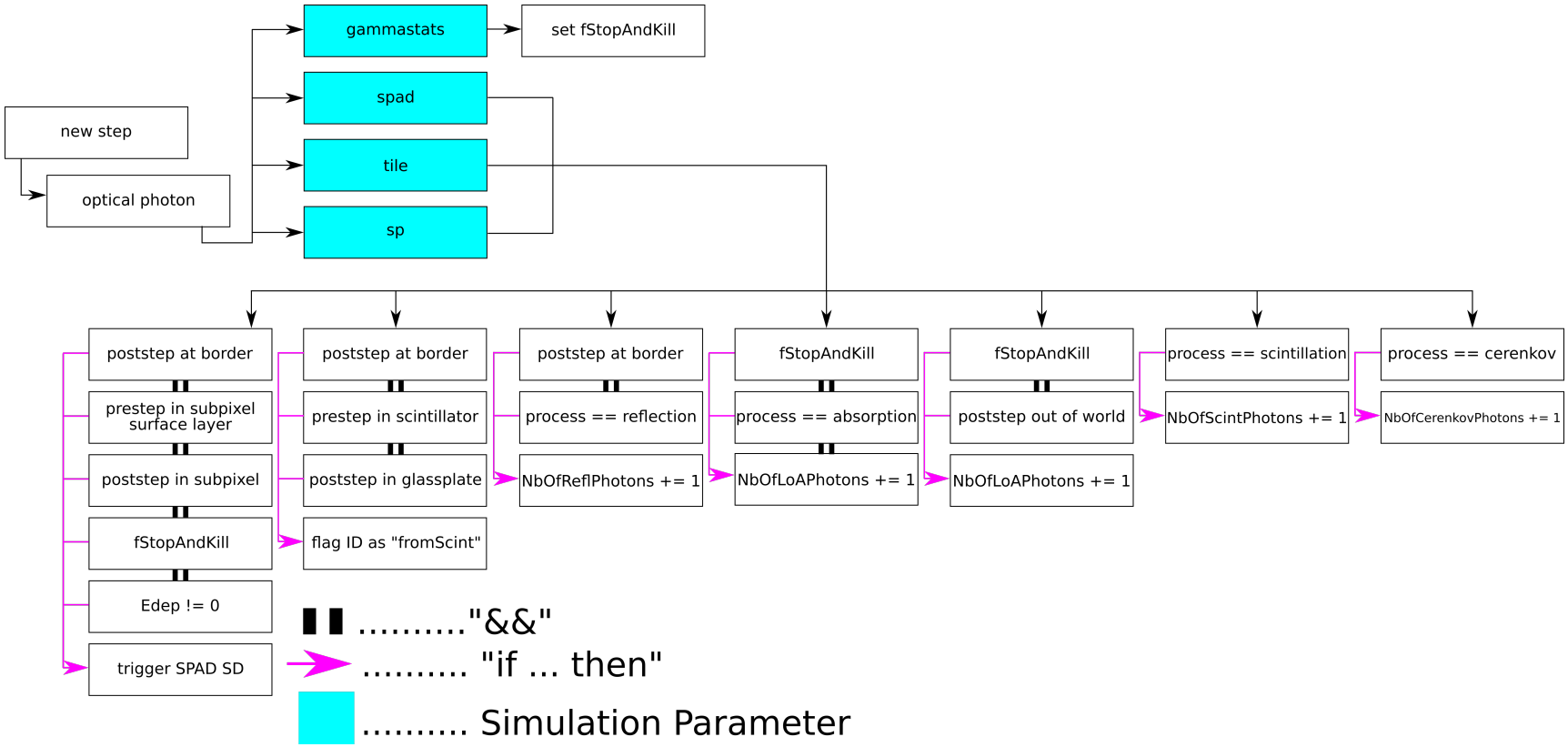

Figure 39: Shown is the decision tree for the stepping action of the application for optical photons. Any counting involving optical photons is done here. Depending on the simulation parameters, optical photons might be killed directly after creation if the parameter "gammastats" for fast gamma calculations has been set.

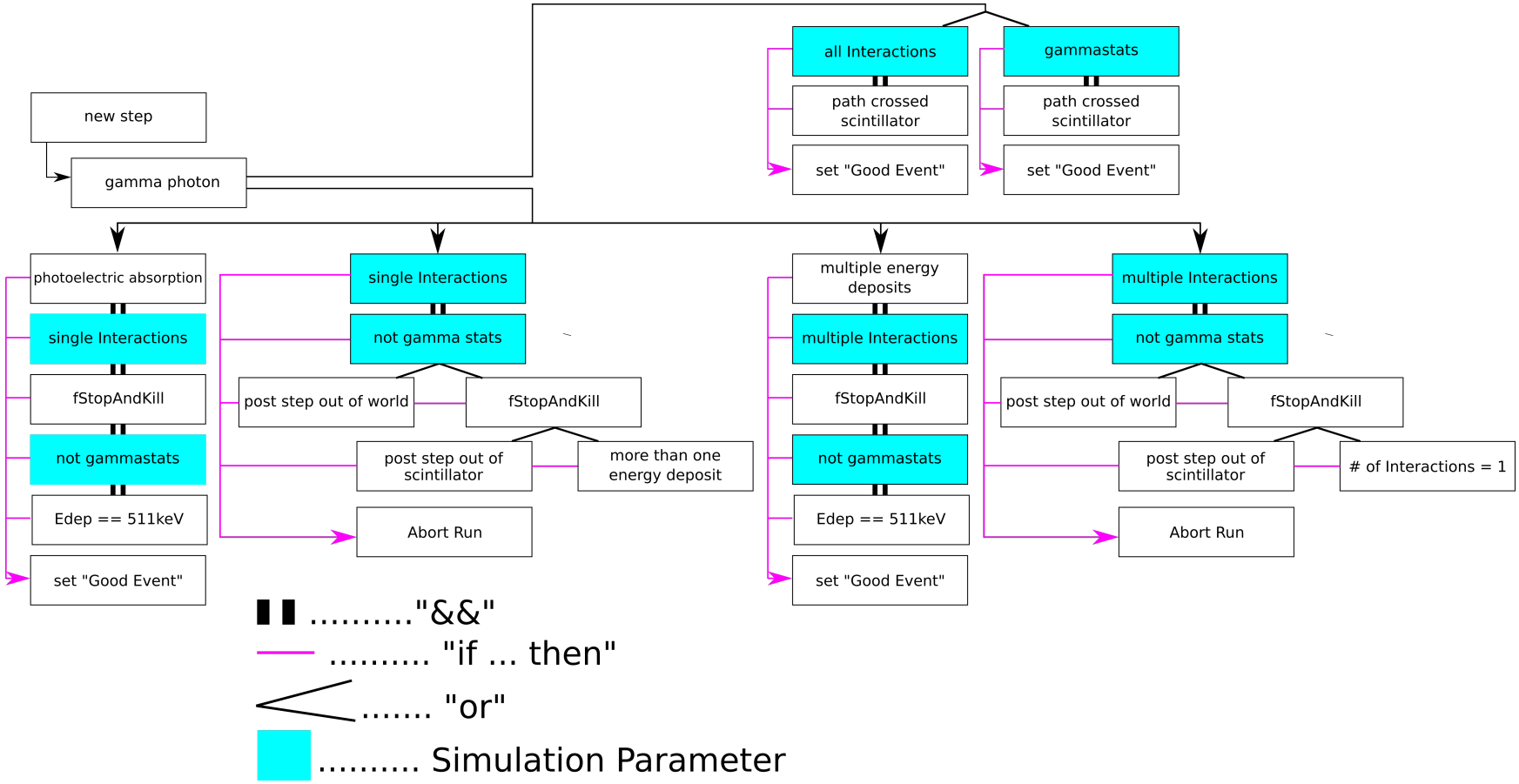

Figure 40: Shown is the decision tree for the stepping action of the application for gamma photons. Here the simulation decides if an event meets any criteria given by the user, i.e. if an event is "good". In the same way, the Stepping Action may abort an event, if the corresponding criteria are met.

8.2.2 Event Action

The workflow of a simulation run is shown in Figure 41. First, at the begin of the run, the output ROOT file is created and the first 2 n-tuples which will contain data across the whole run are booked. Then the simulation moves on to the first event. If new n-tuples are needed to store event data (for the first event, this is always true) then they are initialized (booked) and the corresponding bool variable "need new NTuples" is set to "false". Then the stepping action processes gamma and electron tracks and either accepts of rejects the event. If the event is accepted, "good Event" is set to true otherwise the event is aborted and a new event is started. After the stepping action and the various SDs have processed all their tracks and steps, the simulation enters the end-of-event stage and checks whether the event was flagged as "good". If yes, the data from the event are recorded and "need new NTuples" is set to true again so that new n-tuples are created during the next event. Then, if no more events are needed, the end-of-event stage is entered where the simulation writes data about the whole run into the corresponding n-tuples which were created at the beginning and the run is terminated.

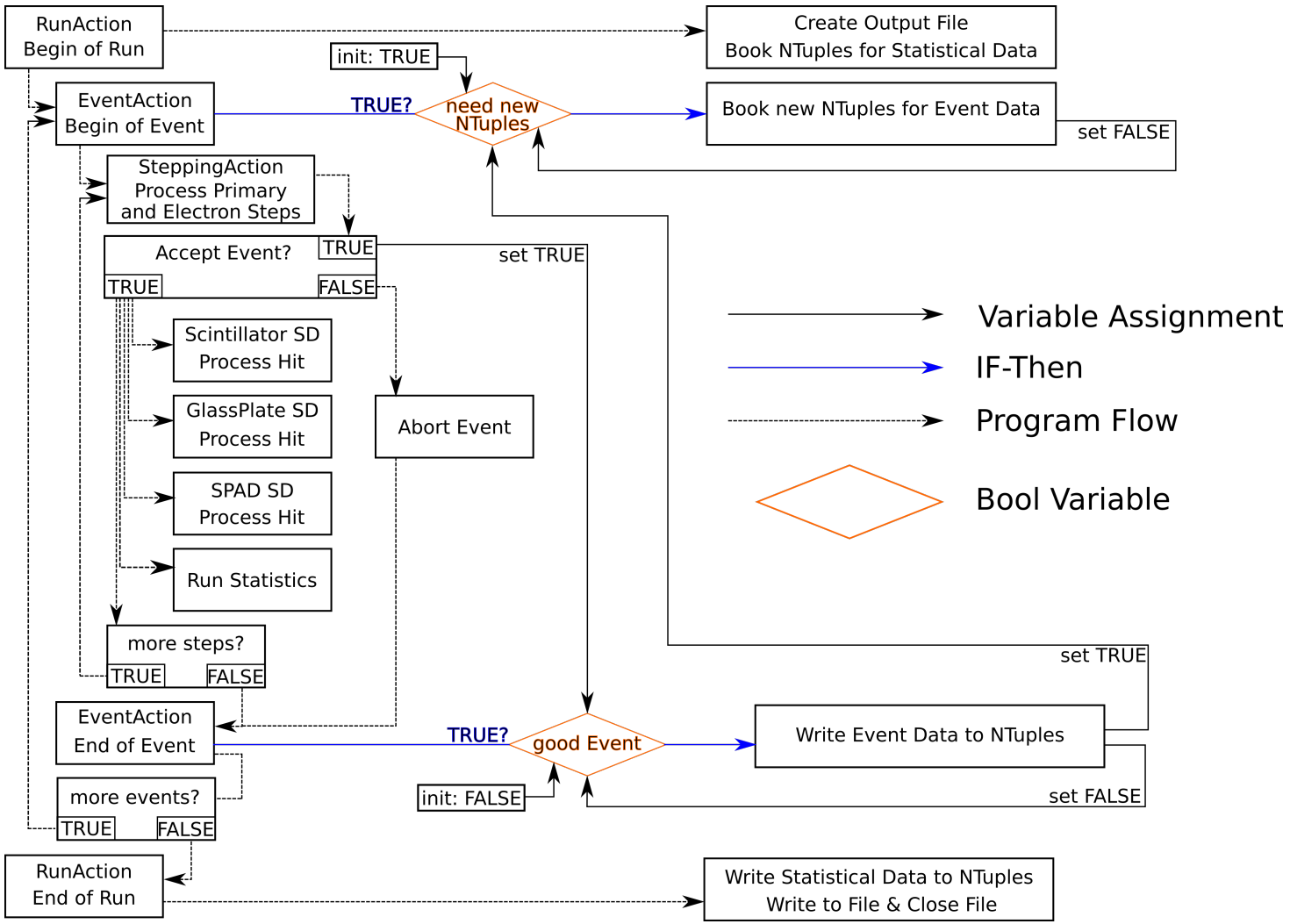

Figure 41: Shown is the decision tree to handle events depending on if they are flagged fit for recording or not. Arrows represent the process order, the diamond shaped box represents a boolean variable which can be toggled between "TRUE" and "FALSE". "Good Event" is initialized "FALSE" and "need new NTuples" is initialized as "TRUE". Blue arrows are if-then-statements.

8.3 SPAD Cell Hit Reconstruction

The ID of a SPAD which was hit by an optical photon—which is synonymous with its position—is calculated from the position on the corresponding sub-pixel where the photon was absorbed.

The "SPAD vector" v_{SPAD} is calculated as the difference between the global hit position v_{hit} and the global sub-pixel position v_{sp}. This vector then "points" at the right SPAD within the SPAD array of the sub-pixel. The calculation of this SPAD vector is complicated by the fact that GEANT4 only provides the local coordinates of a volume within the coordinate system spanned by its mother volume. Consequently, one must acquire the sub-pixels position within its containing pixel, the pixels position within its containing die and so forth until one reaches the world volumes coordinate system. Then, adding up all of these positions will yield the global coordinates. Again, this calculation is complicated even further if one or more volumes along the volume hierarchy are rotated with respect to their mother volumes.

Once the SPAD vector has been obtained, it can be projected into the plane parallel to the sub-pixel's front side. The resulting 2D vector yields which SPAD would have been hit (see Figures 42 and 43).

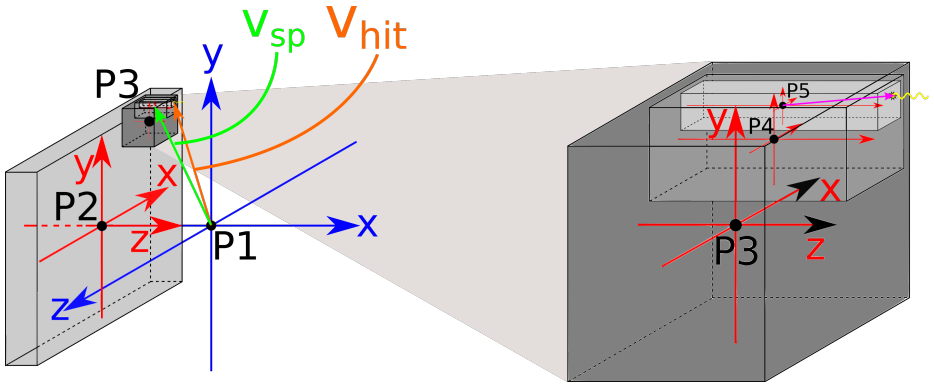

Figure 42: The global hit position can be acquired directly. The global sub-pixel position must be calculated from a series of vectors. P1 is the center of the global coordinate system. P2 is the tile position with respect to global coordinates (because the mother volume of the tile is the world volume). P3 is the die position with respect to tile coordinates (since the tile is the dies mother volume). This pattern continues until P5 which is the sub-pixel position with respect to its containing pixel. The sum $\vec{v}_{P1P2} + \boldsymbol{R}(\vec{v}_{P2P3} + \vec{v}_{P3P4} + \vec{v}_{P4P5})$ will yield the sub-pixel position with respect to global coordinates, where $\boldsymbol{R}$ is a rotation matrix which rotates vectors of the local coordinate systems (red) into the global coordinate system (blue).

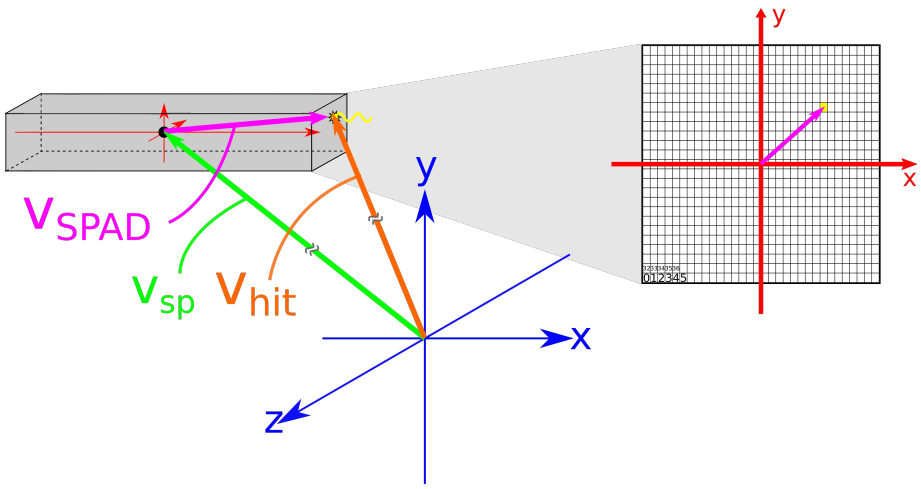

Figure 43: Once the global sub-pixel position and the global hit position have been acquired, the SPAD vector $\vec{v}_{SPAD} = \vec{v}_{hit} - \vec{v}_{sp}$ can be calculated and projected onto the xy-plane of the sub-pixel coordinate system. The coordinates of $\vec{v}_{SPAD}$ allow the calculation of the SPAD ID.